HELSINKI UNIVERSITY OF TECHNOLOGY
Faculty of Electronics, Communications and Automation

Sami P. Kiminki

COMPUTATION OF ANTENNA PARAMETERS USING ELECTROMAGNETIC SURFACE INTEGRAL EQUATIONS

Thesis submitted for examination for the degree of Master of Science in Technology

Espoo 30.10.2009

Thesis supervisor:

Prof. Keijo Nikoskinen

Thesis instructor:

Doc. Pasi Ylä-Oijala

TEKNILLINEN KORKEAKOULU

DIPLOMITYÖN TIIVISTELMÄ

Tekijä: Sami P. Kiminki

Työn nimi: Antenniparametrien laskenta sähkömagnetiikan pintaintegraaliyhtälöillä

Päivämäärä: 30.10.2009 Kieli: Englanti Sivumäärä: 8+81

Tiedekunta: Elektroniikan, tietoliikenteen ja automaation tiedekunta

Professuuri: Sähkömagnetiikka Koodi: S-96

Valvoja: Prof. Keijo Nikoskinen

Ohjaaja: Dos. Pasi Ylä-Oijala

Pintaintegraaliyhtälömenetelmää käytetään laskennallisessa sähkömagnetiikassa yksinkertaistamaan monimutkaisia ongelmia. Menetelmä muuntaa Maxwellin osittaisdifferentiaaliyhtälöt pintaintegraaliyhtälösysteemiksi, jossa tuntematon kenttä esitetään kentän pintaintegraalina yli materiaalirajapintojen. Menetelmää voidaan käyttää ratkaisemaan ongelmia, jotka voidaan jakaa äärelliseen määrään osa-alueita, joissa materiaali on vakio. Menetelmän vahvuus on siinä, että vain osa-alueiden reunapinnat tarvitsee esittää numeerisesti. Lisäksi menetelmän vahvuutena on se, että kentän säteily ympäröivään vapaaseen avaruuteen toteutuu automaattisesti oikein, mikä johtaa hyvään tarkkuuteen vapaan tilan sironta- ja antennitehtävissa.

Tässä työssä käsitellään numeerista sähkömagneetiikan simulointia pintaintegraaliyhtälömenetelmällä. Alussa menetelmän teoreettinen tausta käydään läpi ja siihen tehdään oma tulkinta. Seuraavaksi käydään läpi työkalut ja vaiheet, joita tarvitaan ongelmien numeeriseen ratkaisemiseen menetelmällä. Työssä myös toteutettiin C-kielellä ohjelmoitu EFIE-PMCHWT-formulaation mukaisten yhtälöiden numeerinen ratkaisija, jossa käytetään RWG-funktioita ja momenttimenetelmää ratkaisemaan mielivaltainen paloittain homogeeninen ongelma, jossa voi olla metallisten ja dielektristen alueiden välisiä materiaaliliitoksia. Ratkaisijaa lopulta käytetään dipoliantennin ja mikroliuska-antennin antenniparametrien laskentaan.

Avainsanat: antennit, laskennallinen sähkömagnetiikka, integraaliyhtälömenetelmät, MoM, liitokset

Author: Sami P. Kiminki

Title: Computation of antenna parameters using electromagnetic surface integral equations

Date: 30.10.2009 Language: English Number of pages: 8+81

Faculty: Faculty of Electronics, Communications and Automation

Professorship: Electromagnetics Code: S-96

Supervisor: Prof. Keijo Nikoskinen

Instructor: Doc. Pasi Ylä-Oijala

Surface integral equation method is used in computational electromagnetics to simplify complex problems. The method transforms the Maxwell's partial differential equations into surface integral equation system, where the unknown field is represented as surface integral of the field over the material interface surfaces. The method can be used to solve any problems that can be composed into finite number of subregions of homogeneous media. The strength of the method is that it only needs numerics for the boundary surfaces of the subregions. An additional strength of the method is that the radiation of the field into free space surrounding the problem domain is automatically realized correctly, which results as very good accuracy of scattering and antenna problems inside free space.

This thesis studies numerical electromagnetic simulations with the surface integral equation method. First the theory behind the method is reviewed and interpreted. Then the procedures and tools needed to numerically solve problems with the method are studied. A numerical solver of EFIE-PMCHWT formulation written in C that uses RWG functions and method of moments to solve arbitrary piecewise homogeneous problems with junctions of metallic or dielectric structures is implemented. The solver is then used to compute antenna parameters of a dipole antenna and a microstrip patch antenna.

Keywords: antennas, computational electromagnetics, integral equation methods, MoM, junctions

Preface

I would like to thank my instructor, doc. Pasi Ylä-Oijala for the support, guidance and patience during this work. A lot of questions were answered during this work but at least as many remained open for further research. I would also like to thank D.Sc. Matti Taskinen for his great support and discussions during the programming work, and Ph.D. Seppo Järvenpää for his guidance for threading in C. I also express my deepest gratitude towards my supervisor, prof. Keijo Nikoskinen for his patience, discussions and great leadership at the faculty.

I would also like to thank my mother and all my friends for the great support and friendship you have given me through all these years. Without you my life wouldn't be as happy.

Otaniemi, 30.10.2009

Sami P. Kiminki

Contents

List of symbols and abbreviations

Symbols

f	frequency
ω	angular frequency
t	time
$\boldsymbol{E}$	electric field
$\boldsymbol{H}$	magnetic field
$\boldsymbol{D}$	electric flux density
$\boldsymbol{B}$	magnetic flux density
$\boldsymbol{J}_V$	electric current density
ρ	electric charge density
$\boldsymbol{r}$	position vector, field point
$\boldsymbol{r'}$	source point
ϵ	permittivity of medium
μ	permeability of medium
σ	conductivity of medium
$\boldsymbol{J}_c$	conductivity current density
ϵ_c	complex permittivity of a conductive medium
$\hat{\boldsymbol{n}}$	unit normal vector of a surface
k	wavenumber
G	Green's function
$\boldsymbol{J}_{pol,i}$	relative electric polarization current density
$\boldsymbol{M}_{pol,i}$	relative magnetic polarization current density
$\boldsymbol{J}_i$	domain specific equivalent electric surface current density
$\boldsymbol{M}_i$	domain specific equivalent magnetic surface current density
Z_s	surface impedance
R_s	surface resistance

Operators

D^c	complement of a domain D
∂D	boundary of a domain D
Ω_D	relative solid angle on a boundary surface of domain D
$\mathcal{L}$	surface integral operator
$\mathcal{K}$	surface integral operator
$\mathcal{S}$	surface integral operator
$\mathcal{L}_i$	operator $\mathcal{L}$ with material parameters of domain i
$\mathcal{K}_i$	operator $\mathcal{K}$ with material parameters of domain i
$\mathcal{S}_i$	operator $\mathcal{S}$ with material parameters of domain i
$\nabla_s \cdot$	surface divergence

Abbreviations

FDTD	finite difference time domain
FEM	finite element method
BEM	boundary element method
MoM	method of moments
EFIE	electric field integral equation
MFIE	magnetic field integral equation
CFIE	combined field integral equation
RWG	Rao-Wilton-Glisson
PMCHWT	Poggio-Miller-Chang-Harrington-Wu-Tsai
RF	radio frequency

1 Introduction

Numerical methods have been gaining a lot of interest in electromagnetics lately. The speed and the memory space of typical computers has increased steadily, which has made it possible to calculate quite complex problems nowadays with accurate results. This has resulted as the computational electromagentics society being very active in science.

The methods of computational electromagnetics can roughly be devided into time domain and frequency domain methods. The strength of time domain methods is that they can be used with almost arbitrary excitation signal waveform. However, most of the engineering parameters and specifications are in the frequency domain, which drives to the use of the frequency domain methods. Time domain methods can be used to get frequency domain results with the discrete Fourier transform, but typically the accuracy of the frequency domain results with Fourier techniques is inferior to the accuracy of real frequency domain methods.

The methods of computational electromagnetics can also be devided into other classes, such as into methods that are based on differential equations, such as FDTD or FEM, or into methods that are based on integral equations, such as surface integral equation method (often called as BEM). However, the classification of a numerical method is secondary to the applicability and accuracy that are achievable by the method.

Surface integral equation method is a method of computational electromagnetics that can be used to solve many challenging electromagnetic problems efficiently and accurately. In numerics the method is mostly used only in the frequency domain. The method is based on the fact that the field inside any homogeneous region can be represented in terms of the field values (or the equivalent surface current densities) on the boundary surface of the region. By piecewise representation of the field inside homogeneous subregions, a problem with a finite number of homogeneous subregions is transformed into a system of surface integral equations over the boundary surfaces of the regions. The integral equation system must then be solved to find the unknown field values on the boundary surfaces, which can then be used to represent the field everywhere. The surface integral equation system can be solved numerically with method of moments (MoM).

This thesis includes description of the surface integral equation method and the procedures needed to solve the resulting surface integral equation systems with MoM. A solver routine that can be used to solve general piecewise homogeneous problems including metal and dielectrics is programmed. The implemented solver routine is then used to solve antenna parameters of two small antennas.

Chapters of this thesis are as follows. Chapters 2-3 describe the theory behind the surface integral equations. Chapter 4 describes the numerics and the use of MoM to solve the resulting integral equation system. Chapters 5-6 describe the most important antenna parameters and the way how they are calculated from the numerical results. The programming work and the datastuctures that were

used to e.g. describe the geometry are described in Chapter 7. Chapter 8 includes the results for the antenna paramaters of a dipole antenna and a microstrip patch antenna obtained with the implemented solver routine. Chapter 8.4 includes general analysis of the achieved results and finally, Chapter 9 includes the conclusions.

2 Background

In this chapter the basic theory of electromagnetics is quickly reviewed. The theoretical background of the surface integral equation method is also introduced here. The method itself will be treated in Chapter 3.

2.1 Maxwell's equations

The task of solving electromagnetic problems is to find the solutions to the Maxwell's equations. The equations can be solved either in the time domain or in the frequency domain. If the frequency domain is used, it is equal to assuming harmonic time dependence $e^{-i\omega t}$ for the fields and currents, where the angular frequency ω is related to the physical frequency f by $\omega = 2\pi f$. In the time harmonic case, the time derivative is simply $\partial/\partial t = -i\omega$ and the Maxwell's equations [1] for the electric field $\boldsymbol{E}$, the electric flux density $\boldsymbol{D}$, the magnetic field $\boldsymbol{H}$ and the magnetic flux density $\boldsymbol{B}$ are of the form

$$\begin{aligned} \nabla \times \boldsymbol{E}(\boldsymbol{r}) &= i\omega \boldsymbol{B}(\boldsymbol{r}) && (2.1)\\ \nabla \cdot \boldsymbol{D}(\boldsymbol{r}) &= \rho(\boldsymbol{r}) && (2.2)\\ \nabla \times \boldsymbol{H}(\boldsymbol{r}) &= \boldsymbol{J}_V(\boldsymbol{r}) - i\omega \boldsymbol{D}(\boldsymbol{r}) && (2.3)\\ \nabla \cdot \boldsymbol{B}(\boldsymbol{r}) &= 0, && (2.4) \end{aligned}$$

where $\boldsymbol{J}_V$ is the electric current density and ρ is the electric charge density. By taking divergence of the Ampere's law (2.3) and using the Gauss's law (2.2), we get the continuity relation

$$\nabla \cdot \boldsymbol{J}_V(\boldsymbol{r}) = i\omega \rho(\boldsymbol{r}), \tag{2.5}$$

which expresses the conservation of the electric charge.

In a linear and isotropic medium, when the properties of the medium are independent of field strength and field direction, the dependence of the flux densities and the fields can simply be presented by

$$\begin{aligned} \boldsymbol{D}(\boldsymbol{r}) &= \epsilon(\boldsymbol{r})\boldsymbol{E}(\boldsymbol{r}) && (2.6)\\ \boldsymbol{B}(\boldsymbol{r}) &= \mu(\boldsymbol{r})\boldsymbol{H}(\boldsymbol{r}), && (2.7) \end{aligned}$$

where ϵ is the electric permittivity and μ is the magnetic permeability of the medium. If the medium is conductive, the electric field forces the free charges to move causing a conductivity current distribution

$$\boldsymbol{J}_c(\boldsymbol{r}) = \sigma(\boldsymbol{r})\boldsymbol{E}(\boldsymbol{r}) \tag{2.8}$$

If this is substituted into Ampere's law (2.3) as current density $\boldsymbol{J}_V = \boldsymbol{J}_c$, we see that the conductivity σ in the time harmonic case can be replaced by complex permittivity

$$\epsilon_c(\boldsymbol{r}) = \epsilon(\boldsymbol{r}) + i\frac{\sigma(\boldsymbol{r})}{\omega}. \tag{2.9}$$

Generally the constitutive parameters ϵ and μ can be almost any functions of frequency, but they can depend on the frequency only in a way which matches causality in time domain. This leads to the Kramers-Kronig relations [1] between the real part and the imaginary part of the constitutive parameter.

The solutions of the Maxwell's equations also have further continuity properties [1] for the field and the flux quantities on a border of two media as

$$\begin{aligned} \hat{\boldsymbol{n}} \cdot \boldsymbol{D}_1 &= \hat{\boldsymbol{n}} \cdot \boldsymbol{D}_2 \\ \hat{\boldsymbol{n}} \cdot \boldsymbol{B}_1 &= \hat{\boldsymbol{n}} \cdot \boldsymbol{B}_2 \\ \hat{\boldsymbol{n}} \times \boldsymbol{E}_1 &= \hat{\boldsymbol{n}} \times \boldsymbol{E}_2 \\ \hat{\boldsymbol{n}} \times \boldsymbol{H}_1 &= \hat{\boldsymbol{n}} \times \boldsymbol{H}_2, \end{aligned} \tag{2.10}$$

i.e. normal components $\boldsymbol{B}_n = \hat{\boldsymbol{n}}\hat{\boldsymbol{n}} \cdot \boldsymbol{B}$ and $\boldsymbol{D}_n = \hat{\boldsymbol{n}}\hat{\boldsymbol{n}} \cdot \boldsymbol{D}$ of the fluxs and tangential components $\boldsymbol{E}_{tan} = -\hat{\boldsymbol{n}} \times \hat{\boldsymbol{n}} \times \boldsymbol{E}$ and $\boldsymbol{H}_{tan} = -\hat{\boldsymbol{n}} \times \hat{\boldsymbol{n}} \times \boldsymbol{H}$ of the fields are continuous through the border. Here $\hat{\boldsymbol{n}}$ is a unit normal vector of the boundary surface between the domains pointing either into domain 1 or domain 2. The continuity requirements are clarified in figure 1.

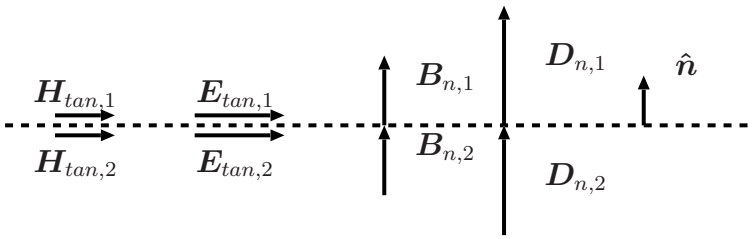

Figure 1: Continuity properties of the fields and fluxs.

On a general surface between two penetrable media, there are no other boundary conditions than the continuity requirements (2.10). On a PEC surface, when the conductivity σ inside the conductive region tends to infinity, the boundary conditions are much simpler. Since the physical quantities such as the conductivity current $\boldsymbol{J}_c$ in (2.8) should not have infinite energy, the electric field $\boldsymbol{E}$ inside the conductive medium must vanish. By the continuity requirements (2.10) this implies that the tangential electric field $\boldsymbol{E}_{tan}$ vanishes on a PEC surface. Actually the normal component of the curl of $\boldsymbol{E}$ also vanishes, because it only contains surface derivatives of the tangential electric field which is zero. If this result is substituted into Faraday's law (2.1) as

$$\hat{\boldsymbol{n}} \cdot \nabla \times \boldsymbol{E} = i\omega \hat{\boldsymbol{n}} \cdot \boldsymbol{B} = 0, \tag{2.11}$$

it implies that the normal component of the magnetic flux density $\boldsymbol{B}$ vanishes in time harmonic case, giving the boundary conditions of a PEC surface as

$$\begin{aligned} \boldsymbol{E}_{tan} &= \boldsymbol{0} \\ \hat{\boldsymbol{n}} \cdot \boldsymbol{B} &= 0. \end{aligned} \tag{2.12}$$

It has to be stressed here that the second condition is only valid for dynamic fields. In statics, only the first condition is valid. Similar could also be done for a surface with PMC boundary condition. In that case one only need to replace $\boldsymbol{E}$ by $\boldsymbol{H}$ and $\boldsymbol{B}$ by $\boldsymbol{D}$.

The boundary conditions and the Maxwell's equations together with the physical requirement of finite energy of the fields define the differential equation problem for the electromagnetic field. The problem can be solved analytically in certain special cases, but numerical methods are often more versatile and can solve almost arbitrary problems.

2.2 Surface equivalence principle

Let D present the domain of interest. Let's assume that the space is homogeneous with constant isotropic material parameters ϵ and μ. If the sources of the electromagnetic field, ie. charge distributions $\rho(\boldsymbol{r})$ and current distributions $\boldsymbol{J}_V(\boldsymbol{r})$, are outside of D, the electromagnetic field inside D satisfies the homogeneous Helmholtz equations [1]

$$\begin{aligned} \left(\nabla^2 + k^2\right) \boldsymbol{E} &= 0 \\ \left(\nabla^2 + k^2\right) \boldsymbol{H} &= 0, \end{aligned} \tag{2.13}$$

where $\nabla^2 = \Delta = \nabla \cdot \nabla$ is the Laplace operator and wavenumber $k = \omega\sqrt{\mu\epsilon}$.

Let S present a closed surface that is the boundary of D. The electromagnetic surface equivalence principle [2, 3] states that the electric field $\boldsymbol{E}$ and the magnetic field $\boldsymbol{H}$ in D can be represented by the expressions [4]

$$\Omega_D(\boldsymbol{r})\,\boldsymbol{E}(\boldsymbol{r}) = \eta\mathcal{L}(\hat{\boldsymbol{n}} \times \boldsymbol{H})(\boldsymbol{r}) + \mathcal{K}(\hat{\boldsymbol{n}} \times \boldsymbol{E})(\boldsymbol{r}) \tag{2.14}$$

$$\Omega_D(\boldsymbol{r})\,\boldsymbol{H}(\boldsymbol{r}) = -\frac{1}{\eta}\mathcal{L}(\hat{\boldsymbol{n}} \times \boldsymbol{E})(\boldsymbol{r}) + \mathcal{K}(\hat{\boldsymbol{n}} \times \boldsymbol{H})(\boldsymbol{r}), \tag{2.15}$$

where $\eta = \sqrt{\mu/\epsilon}$ is the wave impedance of the medium and relative solid angle of the smooth surface S is

$$\Omega_D(\boldsymbol{r}) = \begin{cases} 1, & \boldsymbol{r} \in D, \\ \frac{1}{2}, & \boldsymbol{r} \in S \\ 0, & \boldsymbol{r} \in D^c. \end{cases} \tag{2.16}$$

Here D^c is the complement of D and $\hat{\boldsymbol{n}}$ is the unit normal vector of the surface S pointing into D.

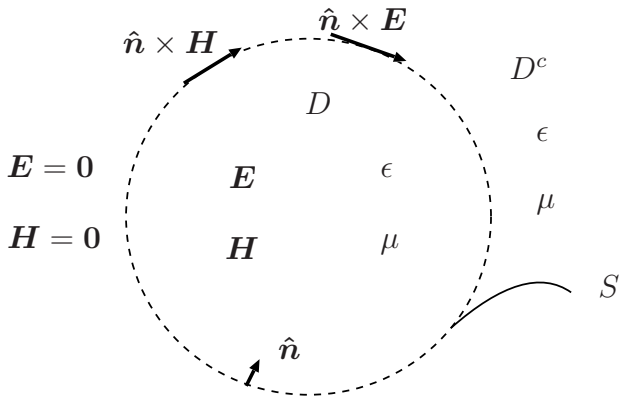

Figure 2: Surface equivalence principle.

Surface integral operators of equations (2.14) and (2.15) operating to a smooth enough vector function $\boldsymbol{F}$ are

$$\mathcal{L}(\boldsymbol{F})(\boldsymbol{r}) = -\frac{1}{ik}\nabla\mathcal{S}(\nabla'_s \cdot \boldsymbol{F})(\boldsymbol{r}) + ik\mathcal{S}(\boldsymbol{F})(\boldsymbol{r}) \tag{2.17}$$

$$\mathcal{K}(\boldsymbol{F})(\boldsymbol{r}) = \nabla \times \mathcal{S}(\boldsymbol{F})(\boldsymbol{r}) \tag{2.18}$$

$$\mathcal{S}(\boldsymbol{F})(\boldsymbol{r}) = \int_S G(\boldsymbol{r}, \boldsymbol{r'})\, \boldsymbol{F}(\boldsymbol{r'})\, \mathrm{d}S(\boldsymbol{r'}), \tag{2.19}$$

where $G(\boldsymbol{r}, \boldsymbol{r'})$ is the Green's function of the Helmholtz operator in D that satisfies the equation

$$\left(\nabla^2 + k^2\right) G(\boldsymbol{r}, \boldsymbol{r}') = -\delta(\boldsymbol{r}, \boldsymbol{r}'), \tag{2.20}$$

for any combination of source point $\boldsymbol{r}'$ and field point $\boldsymbol{r}$ within D with $\delta(\boldsymbol{r}, \boldsymbol{r}')$ being the three dimensional delta function that fulfils the equation

$$f(\boldsymbol{r}) = \int_{\mathcal{R}^3} f(\boldsymbol{r}')\, \delta(\boldsymbol{r}, \boldsymbol{r}')\, \mathrm{d}V' \tag{2.21}$$

for an arbitrary smooth function $f(\boldsymbol{r})$. Surface divergence in (2.17) is

$$\nabla'_s \cdot \boldsymbol{F}(\boldsymbol{r}') = \nabla' \cdot \boldsymbol{F}(\boldsymbol{r}') - \frac{\partial}{\partial n'}\left(\hat{\boldsymbol{n}}' \cdot \boldsymbol{F}(\boldsymbol{r}')\right). \tag{2.22}$$

The Green's function of the Helmholtz operator for an infinite homogeneous free space is

$$G(\boldsymbol{r}, \boldsymbol{r}') = \frac{e^{ik|\boldsymbol{r}-\boldsymbol{r}'|}}{4\pi\,|\boldsymbol{r} - \boldsymbol{r}'|}. \tag{2.23}$$

The quantities $\hat{\boldsymbol{n}} \times \boldsymbol{H}$ and $\hat{\boldsymbol{n}} \times \boldsymbol{E}$ are often defined in terms of so called equivalent electric and magnetic surface current densities $\boldsymbol{J}$ and $\boldsymbol{M}$ [4] as

$$\begin{aligned} \boldsymbol{J} &= \hat{\boldsymbol{n}} \times \boldsymbol{H} \\ \boldsymbol{M} &= -\hat{\boldsymbol{n}} \times \boldsymbol{E}. \end{aligned} \tag{2.24}$$

The equivalent electric surface current density $\boldsymbol{J}$ is actually equal to the physical surface current that would induce on a PEC surface.

The results of equations (2.14) and (2.15) mean that the fields in any homogeneous medium can be calculated when the tangential fields are known on a closed surface. This fact is classically referred to as Huygens' principle.

2.2.1 Alternative forms of the surface equivalence principle

The surface equivalence principle itself can be used to represent fields inside any domain where the Green's function that satisfies equation (2.20) is known. The fields are calculated by using representation formulas (2.14) and (2.15) with integral operators (2.17)-(2.19) which gives

$$\Omega_D(\boldsymbol{r})\,\boldsymbol{E}(\boldsymbol{r}) = -\frac{1}{i\omega\epsilon}\nabla\mathcal{S}\left(\nabla_s' \cdot \boldsymbol{J}\right)(\boldsymbol{r}) + i\omega\mu\mathcal{S}\left(\boldsymbol{J}\right)(\boldsymbol{r}) - \nabla \times \mathcal{S}\left(\boldsymbol{M}\right)(\boldsymbol{r}) \tag{2.25}$$

$$\Omega_D(\boldsymbol{r})\,\boldsymbol{E}(\boldsymbol{r}) = -\frac{1}{i\omega\mu}\nabla\mathcal{S}\left(\nabla_s' \cdot \boldsymbol{M}\right)(\boldsymbol{r}) + i\omega\epsilon\mathcal{S}\left(\boldsymbol{M}\right)(\boldsymbol{r}) + \nabla \times \mathcal{S}\left(\boldsymbol{J}\right)(\boldsymbol{r}) \tag{2.26}$$

The problem is that the first term in equations (2.25) and (2.26) tends to infinity as ω tends to zero. This causes so-called low frequency breakdown in numerics [5]. However, the Faraday's law (2.1) and the Ampere's law (2.3) can be used to see that

$$\begin{aligned} \hat{\boldsymbol{n}} \cdot \nabla \times \boldsymbol{H} &= -\nabla_S \cdot \boldsymbol{J} = -i\omega\epsilon\hat{\boldsymbol{n}} \cdot \boldsymbol{E} \\ \hat{\boldsymbol{n}} \cdot \nabla \times \boldsymbol{E} &= \nabla_S \cdot \boldsymbol{M} = i\omega\mu\hat{\boldsymbol{n}} \cdot \boldsymbol{H}. \end{aligned} \tag{2.27}$$

A general vector rule was used here, that can be proved by dividing a general vector field $\boldsymbol{F}$ on a surface to normal component $\boldsymbol{F}_n = \hat{\boldsymbol{n}}\hat{\boldsymbol{n}} \cdot \boldsymbol{F}$ and two tangential components $\boldsymbol{F}_{t_1} = \hat{\boldsymbol{t}}_1\hat{\boldsymbol{t}}_1 \cdot \boldsymbol{F}$ and $\boldsymbol{F}_{t_2} = \hat{\boldsymbol{t}}_2\hat{\boldsymbol{t}}_2 \cdot \boldsymbol{F}$ which results as

$$\hat{\boldsymbol{n}} \cdot \nabla \times \boldsymbol{F} = a_{t_1}(\boldsymbol{r})\,\partial_{t_1}F_{t_2} - a_{t_2}(\boldsymbol{r})\,\partial_{t_2}F_{t_1} = -\nabla_S \cdot \hat{\boldsymbol{n}} \times \boldsymbol{F}. \tag{2.28}$$

With equations (2.27) we see that the surface divergences of the equivalent surface currents are related to the normal components of the fields. The relations are actually similar to the continuity relation between charge density ρ and current density $\boldsymbol{J}_V$ in volume (2.5), if equivalent electric surface charge density ρ_E and equivalent magnetic surface charge density ρ_H are defined as

$$\begin{aligned} \rho_E &= \hat{\boldsymbol{n}} \cdot \boldsymbol{D} \\ \rho_H &= \hat{\boldsymbol{n}} \cdot \boldsymbol{B}. \end{aligned} \tag{2.29}$$

Actually ρ_E is equal to the physical electric charge surface density on a PEC surface. This is in line with the fact that the equivalent surface current density $\boldsymbol{J}$ is equal to the real current that would induce on a PEC surface. Since the induced surface current must also satisfy the continuity requirement similar to (2.5), it would as itself imply results (2.27).

The results (2.27) can be used to develop an alternative form for the representation formulas (2.14) and (2.15) as

$$\begin{aligned} \Omega_D(\boldsymbol{r})\,\boldsymbol{E}(\boldsymbol{r}) &= -\nabla\mathcal{S}(\hat{\boldsymbol{n}}\cdot\boldsymbol{E})(\boldsymbol{r}) + i\omega\mu\mathcal{S}(\boldsymbol{J})(\boldsymbol{r}) - \mathcal{K}(\boldsymbol{M})(\boldsymbol{r}) \qquad (2.30)\\ \Omega_D(\boldsymbol{r})\,\boldsymbol{H}(\boldsymbol{r}) &= -\nabla\mathcal{S}(\hat{\boldsymbol{n}}\cdot\boldsymbol{H})(\boldsymbol{r}) + i\omega\epsilon\mathcal{S}(\boldsymbol{M})(\boldsymbol{r}) + \mathcal{K}(\boldsymbol{J})(\boldsymbol{r}) \qquad (2.31) \end{aligned}$$

These representation formulas are equal to the original formulas by Stratton and Chu given in [2]. These representation formulas don't have the low frequency breakdown problem and can be used to develop integral equation formulations applicable also to low frequency problems [6]. The difference of these formulas compared to the formulas (2.14) and (2.15) is that these formulas also use the normal components of the surface fields to represent the fields whereas the earlier presented formulas only use the tangential components of the surface fields. When using the normal components of the fields, the Lorenz gauge conditions

$$\begin{aligned} \nabla\cdot\mathcal{S}(\boldsymbol{J}) &= i\omega\epsilon\mathcal{S}(\hat{\boldsymbol{n}}\cdot\boldsymbol{E})\\ \nabla\cdot\mathcal{S}(\boldsymbol{M}) &= i\omega\mu\mathcal{S}(\hat{\boldsymbol{n}}\cdot\boldsymbol{H}) \end{aligned} \qquad (2.32)$$

need to be included as additional equations in order to get a proper solution satisfying the Maxwell's equations [7]. The Lorenz conditions are equal to the conditions (2.27) that are operated on both sides with integral operator $\mathcal{S}$ (2.19). However, since antenna problems of this thesis don't have real problems with the low frequency breakdown, the formulas that only use the tangential surface fields will be used to solve the problems.

2.3 Polarization currents

The surface representation formulas (2.14) and (2.15) are easier to use in a homogeneous free space than in a general case. One can use the free space Green's function (2.23), and there's no need to find more complicated Green's functions such as that for layered media [8]. So one would prefer to solve problems only in homogeneous free space.

Let's consider a problem, where an ostacle of arbitrary shape with isotropic material parameters (ϵ_1, μ_1) is placed in vacuum and in a known incident field $\boldsymbol{E}_0^p$ and $\boldsymbol{H}_0^p$.

The Maxwell's curl equations (2.1) and (2.3) inside the obstacle can be rewritten as

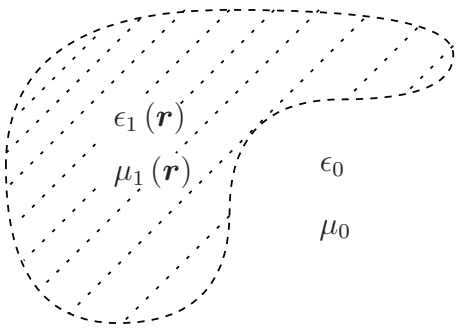

Figure 3: Inhomogeneity (ϵ_1, μ_1) inside vacuum (ϵ_0, μ_0). The material parameters inside the inhomogeneity can be non-constant.

$$\begin{aligned}
\nabla \times \boldsymbol{E}_1 &= i\omega\mu_1(\boldsymbol{r})\boldsymbol{H}_1(\boldsymbol{r}) = i\omega\mu_0\boldsymbol{H}_1(\boldsymbol{r}) + i\omega(\mu_1(\boldsymbol{r}) - \mu_0)\boldsymbol{H}_1(\boldsymbol{r}) \\
&= i\omega\mu_0\boldsymbol{H}_1(\boldsymbol{r}) - \boldsymbol{M}_{pol}(\boldsymbol{r}) \qquad (2.33) \\
\nabla \times \boldsymbol{H}_1 &= -i\omega\epsilon_1(\boldsymbol{r})\boldsymbol{E}_1(\boldsymbol{r}) = -i\omega\epsilon_0\boldsymbol{E}_1(\boldsymbol{r}) - i\omega(\epsilon_1(\boldsymbol{r}) - \epsilon_0)\boldsymbol{E}_1(\boldsymbol{r}) \\
&= -i\omega\epsilon_0\boldsymbol{E}_1(\boldsymbol{r}) + \boldsymbol{J}_{pol}(\boldsymbol{r}). \qquad (2.34)
\end{aligned}$$

We see, that by simply using the polarization currents $\boldsymbol{J}_{pol} = -i\omega(\epsilon_1 - \epsilon_0)\boldsymbol{E}_1$ and $\boldsymbol{M}_{pol} = -i\omega(\mu_1 - \mu_0)\boldsymbol{H}_1$, which depend on the material parameters ϵ_1 and μ_1 and the unknown fields $\boldsymbol{E}_1$ and $\boldsymbol{H}_1$ inside the scatterer, the space is homogenized into vacuum (ϵ_0, μ_0). Since the polarization currents are non-zero only inside the obstacle, the field caused by the polarization currents is sourceless outside the obstacle in the homogenized space. This means that by placing the equivalent surface current densities $\boldsymbol{J}$ and $\boldsymbol{M}$ (2.24) on the boundary surface of the obstacle, the surface representation formulas (2.14) and (2.15) with the free space Green's function (2.23) and material parameters of the vacuum can be used to represent the change of the field, i.e. the scattered field, caused by the obstacle in the vacuum outside the obstacle.

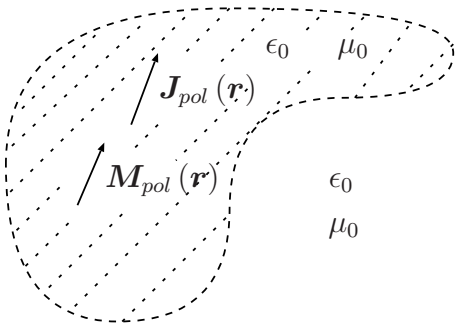

Figure 4: Replacement of inhomogeneity with electric polarization current $\boldsymbol{J}_{pol}$ and magnetic polarization current $\boldsymbol{M}_{pol}$. The domain with the dashed line is where the polarization currents are non-zero. The scattered field caused by the polarization currents is sourceless outside the inhomogenities.

If the scattered fields in the vacuum caused by the polarization currents are denoted $\boldsymbol{E}_0^s$ and $\boldsymbol{H}_0^s$, the total fields in the vacuum outside the obstacle are the sum of the incident fields and the scattered fields as

$$\begin{aligned} \boldsymbol{E}_0^t &= \boldsymbol{E}_0^p + \boldsymbol{E}_0^s \\ \boldsymbol{H}_0^t &= \boldsymbol{H}_0^p + \boldsymbol{H}_0^s. \end{aligned} \tag{2.35}$$

2.3.1 Relative polarization currents

Now let's assume that the space can be described by finite number of homogeneous subdomains D_i. The subdomains can have arbitrary constitutive parameters ϵ_i and μ_i, that are constant inside D_i. The subdomains can even be made of PEC or PMC with the total field inside such domains being zero.

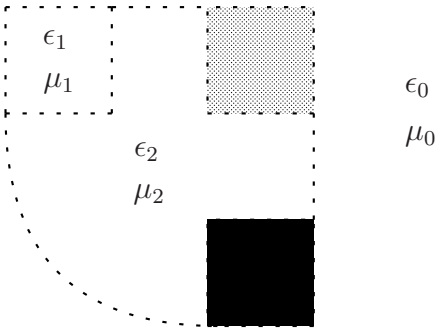

Figure 5: General field problem with piecewise homogeneous space. The PEC domains are denoted by solid black and the PMC domains are shaded.

This kind of a problem can also be simplified with the polarization currents. If for each subdomain D_i we define relative polarization currents as

$$\begin{aligned} \boldsymbol{J}_{pol,i} &= -i\omega\left(\epsilon\left(\boldsymbol{r}\right) - \epsilon_i\right)\boldsymbol{E} \\ \boldsymbol{M}_{pol,i} &= -i\omega\left(\mu\left(\boldsymbol{r}\right) - \mu_i\right)\boldsymbol{H}, \end{aligned} \tag{2.36}$$

the problem with homogeneous subdomains D_i is transformed into a set of polarization current problems each in a homogeneous space with constitutive parameters ϵ_i and μ_i. The relative polarization currents $\boldsymbol{J}_{pol,i}$ and $\boldsymbol{M}_{pol,i}$ lie outside the domain D_i itself, which means that the field of these relative polarization currents is sourceless in D_i. This further means that the surface representation formulas (2.14) and (2.15) with the free space Green's function (2.23) of D_i and material parameters ϵ_i and μ_i can be used to represent the field of the relative polarization currents $\boldsymbol{J}_{pol,i}$ and $\boldsymbol{M}_{pol,i}$ inside D_i.

By using the surface equivalence principle to represent the field of the polarization currents $\boldsymbol{J}_{pol,i}$ and $\boldsymbol{M}_{pol,i}$ inside the subdomain D_i, the problem with a finite number of homogeneous subdomains is further transformed into a problem of solving a system of surface integral equations for the field inside the subdomains D_i in terms

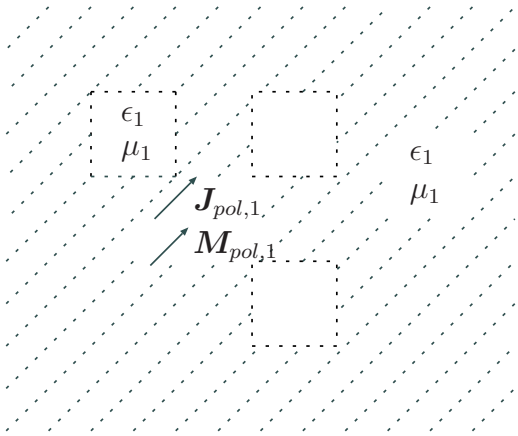

Figure 6: Replacement of the surrounding space of a homogeneous domain D_1 with relative polarization currents $\boldsymbol{J}_{pol,1}$ and $\boldsymbol{M}_{pol,1}$ and homogeneous material with constitutive parameters equal to the ones inside the domain (ϵ_1, μ_1).

of the unknown equivalent surface current densities $\boldsymbol{J}_i$ and $\boldsymbol{M}_i$ on the boundaries ∂D_i.

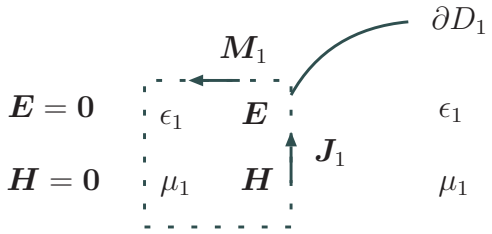

Figure 7: Representation of the field of the relative polarization currents $\boldsymbol{J}_{pol,1}$ and $\boldsymbol{M}_{pol,1}$ of Figure 6 inside the subdomain D_1 (ϵ_1, μ_1) in terms of the equivalent surface current densities $\boldsymbol{J}_1$ and $\boldsymbol{M}_1$ on ∂D_1.

The way how this kind of piecewise homogeneous problems are solved with the surface integral representation formulas is treated in Chapter 3.

2.4 Impedance boundary condition

Electromagnetic properties of metals are mostly characterized by high electric conductivity σ. As was shown in (2.9), the conductivity in time harmonics can be replaced by complex permittivity ϵ_c. If the conductivity is very high, the permittivity is mainly imaginary as $\epsilon_c \approx i\sigma/\omega$ when the frequency is low enough at $\omega << \sigma/\epsilon_0$. If it's further assumed that the magnetic permeability μ is equal to the permeability μ_0 of vacuum, the wave number inside the conductive medium is

$$k_c = \omega\sqrt{\mu_0\epsilon_c} = (1+i)\sqrt{\frac{\omega\mu_0\sigma}{2}} = \frac{1+i}{\delta}, \tag{2.37}$$

where

$$\delta = \sqrt{\frac{2}{\omega\mu\sigma}} \tag{2.38}$$

is the skin depth [1] of the conductive medium. The plane waves that have electric field $\boldsymbol{E} = \boldsymbol{E}_0 e^{i\boldsymbol{k}\cdot\boldsymbol{r}}$ damp exponentially inside a conductive medium. This additional damping is also seen, if the wavenumber k_c is substituted into Green's function (2.23) of homogeneous space, when we get

$$G(\boldsymbol{r}, \boldsymbol{r}') = e^{-R/\delta} \cdot \frac{e^{iR/\delta}}{4\pi R}. \tag{2.39}$$

As conductivity σ tends to infinity, the skin depth δ tends to zero, which means that the fields are zero inside the conductive domain. In this case the polarization currents $\boldsymbol{J}_{pol}$ and $\boldsymbol{M}_{pol}$ of the conductive domain would in limit reside only on the boundary surface of the conductive domain.

The effects of a well conducting medium outside the conductive domain can in most cases be well approximated by the impedance boundary condition [1]

$$\boldsymbol{E}_{tan} = Z_s \hat{\boldsymbol{n}} \times \boldsymbol{H} = Z_s \boldsymbol{J}, \tag{2.40}$$

where Z_s is the surface impedance of the conductive medium. When using the impedance boundary condition, it's assumed that the fields at different points on the conductive surface don't interact through the conductive medium. This is mostly true if both the dimensions of the conductive medium and the curvature of the boundary surface are large enough compared to the skin depth δ.

On the surface of conductive half-space, the surface impedance is simply equal to the wave impedance of the conductive medium as

$$Z_s = \sqrt{\frac{\mu_0}{\epsilon_c}} = \frac{1+i}{\sigma\delta}. \tag{2.41}$$

The total power loss to the conductive medium having a closed boundary surface S is

$$P_c = \frac{1}{2}\Re \int_S Z_s \left|\boldsymbol{J}\right|^2 \mathrm{d}S. \tag{2.42}$$

The surface impedance of conductive half space can also be used for sufficiently smooth surfaces of small curvature in order to approximate the losses inside the conductive medium. The problems with the surface impedance approximation arise when the local dimensions of the conductive medium are small compared to the skin depth or when there are sharp edges on the conductive surface. Near a sharp edge, the surface impedance is supposed to be higher than on a smooth surface, since the surface current flowing along the edge basically has less of the conductive medium around it, which increases the effective surface resistance [9, 10].

2.5 Method of Moments

Method of moments as applied to electromagnetic problems was first thoroughly investigated by Harrington in [11]. The method is used in numerics to find an approximative solution to a general integral or differential operator equation

$$\mathcal{L}_0 \left(\boldsymbol{f}\right)\left(\boldsymbol{r}\right) = \boldsymbol{g}\left(\boldsymbol{r}\right), \qquad \boldsymbol{r} \in D, \tag{2.43}$$

where $\mathcal{L}_0$ is an arbitrary linear differential or integral operator. In the method of moments, the solution $\boldsymbol{f}\left(\boldsymbol{r}\right)$ is sought as linear combination of known basis functions $\boldsymbol{b}_n\left(\boldsymbol{r}\right)$.

$$\boldsymbol{f}\left(\boldsymbol{r}\right) \approx \sum_{n=1}^{N} \alpha_n \boldsymbol{b}_n\left(\boldsymbol{r}\right) \tag{2.44}$$

Since the operator $\mathcal{L}_0$ is linear, it can be moved to operate directly on the basis functions giving the equation

$$\sum_{n=1}^{N} \alpha_n \mathcal{L}_0 \left(\boldsymbol{b}_n\right)\left(\boldsymbol{r}\right) \approx \boldsymbol{g}\left(\boldsymbol{r}\right). \tag{2.45}$$

The basis functions should be such that they fulfil the continuity requirements and the boundary conditions of the unknown $\boldsymbol{f}\left(\boldsymbol{r}\right)$. The set of basis functions should also be able to represent all the properties of the unknown, such as some specific singularities.

The approximative solution (2.44) can't exactly satisfy original equation (2.43) at all points in the problem domain D. Since there are only N degrees of freedom in

(2.44), the original equation can maximally be forced to hold in $M = N$ different points $\boldsymbol{r}_m \in D$ giving the system of equations for $m = 1, \ldots, M$

$$\sum_{n=1}^{N} \alpha_n \mathcal{L}_0 \left(\boldsymbol{b}_n\right)\left(\boldsymbol{r}_m\right) \approx \boldsymbol{g}\left(\boldsymbol{r}_m\right). \tag{2.46}$$

Since the definition of the delta function (2.21) this can be rewritten as

$$\int_D \delta\left(\boldsymbol{r}, \boldsymbol{r}_m\right) \sum_{n=1}^{N} \alpha_n \mathcal{L}_0 \left(\boldsymbol{b}_n\right)\left(\boldsymbol{r}\right) \mathrm{d}\boldsymbol{r} \approx \int_D \delta\left(\boldsymbol{r}, \boldsymbol{r}_m\right) \boldsymbol{g}\left(\boldsymbol{r}\right) \mathrm{d}\boldsymbol{r}. \tag{2.47}$$

This is called the point-matching method [11] since the original equation is forced to hold exactly at certain matching points $\boldsymbol{r}_m$. However, there's generally no guarantee for the accuracy of the solution between the matching points in D.

In order to include the solution values between the matching points $\boldsymbol{r}_m$ also into the system of equations, a more general testing procedure is introduced. Let's define inner product between two general vector functions for the problem as

$$\langle \boldsymbol{f}, \boldsymbol{g} \rangle = \int_D \boldsymbol{f}\left(\boldsymbol{r}\right) \cdot \boldsymbol{g}\left(\boldsymbol{r}\right) \mathrm{d}\boldsymbol{r}, \tag{2.48}$$

If we now define a set of testing functions $\boldsymbol{t}_m$, that are in the range of $\mathcal{L}_0$ and take the inner products of approximative equation (2.45) with all the testing functions, we get a system of equations

$$\sum_{n=1}^{N} \alpha_n \left\langle \boldsymbol{t}_m, \mathcal{L}_0 \left(\boldsymbol{b}_n\right) \right\rangle \approx \left\langle \boldsymbol{t}_m, \boldsymbol{g} \right\rangle. \tag{2.49}$$

The set of testing functions $\boldsymbol{t}_m$ should be in the range of $\mathcal{L}_0$ and it should also be able to represent the excitation $\boldsymbol{g}$ well enough. The resulting system of equations can of course be written in matrix form as

$$L\alpha = \beta, \tag{2.50}$$

where

$$L = \begin{bmatrix} \langle \boldsymbol{t}_1, \mathcal{L}_0\left(\boldsymbol{b}_1\right) \rangle & \langle \boldsymbol{t}_1, \mathcal{L}_0\left(\boldsymbol{b}_2\right) \rangle & \ldots \\ \langle \boldsymbol{t}_2, \mathcal{L}_0\left(\boldsymbol{b}_1\right) \rangle & \langle \boldsymbol{t}_2, \mathcal{L}_0\left(\boldsymbol{b}_2\right) \rangle & \ldots \\ \vdots & \vdots & \ddots \end{bmatrix}$$

$$\alpha = \begin{bmatrix} \alpha_1 \\ \alpha_2 \\ \vdots \end{bmatrix}$$

$$\beta = \begin{bmatrix} \langle \boldsymbol{t}_1, \boldsymbol{g} \rangle \\ \langle \boldsymbol{t}_2, \boldsymbol{g} \rangle \\ \vdots \end{bmatrix}$$

This is the method of moments as represented in [11]. If the general MoM is compared to the point-matching method, we see that the point matching is a specific case of MoM with Dirac delta functions as testing functions. A special choice $\boldsymbol{t}_n = \boldsymbol{b}_n$ is called Galerkin's method. Galerkin's method will be used in this thesis to solve antenna problems with the surface integral equation method.

The basis functions and the testing functions can be non-zero either on the entire problem domain D or only on a subset of D. By dividing the domain D into simple subdomains such as triangles or tetrahedrons, one can use local basis functions that are non-zero only in a limited number of subdomains. Generally it's easier to generate the local basis and testing functions than to find specific entire domain basis functions for arbitrary D that satisfy the continuity requirements and the boundary conditions.

One of the most important results of the scientific work with MoM in the past has actually been with finding correct kinds of local basis and testing functions for different problems. Local basis and testing functions defined for triangular meshes by Rao, Wilton and Glisson in [12] will be used in this thesis to solve the resulting surface integral equations numerically with MoM.

3 Surface Integral Equation Method

Surface equivalence principle together with simplification of problems with the relative polarization currents can be used to develop a method to solve complex electromagnetic problems. As will be shown, any problem with piecewise homogeneous space can be described by polarization currents, surface equivalence principle and a set of solutions of simple scattering problems.

3.1 Scattering problem

Let's consider a simple scattering problem, where a homogeneous scatterer with arbitrary material parameters (ϵ_2, μ_2) is placed in a homogeneous media (ϵ_1, μ_1) and in a known incident electric field $\boldsymbol{E}^p$ and incident magnetic field $\boldsymbol{H}^p$. Let's denote the domain outside of the scatterer by D_1, the domain inside the scatterer by D_2 and the surface of the scatterer by S. And let's decide, that the unit normal vector $\hat{\boldsymbol{n}}_1$ points to the domain D_1 and $\hat{\boldsymbol{n}}_2$ to the domain D_2.

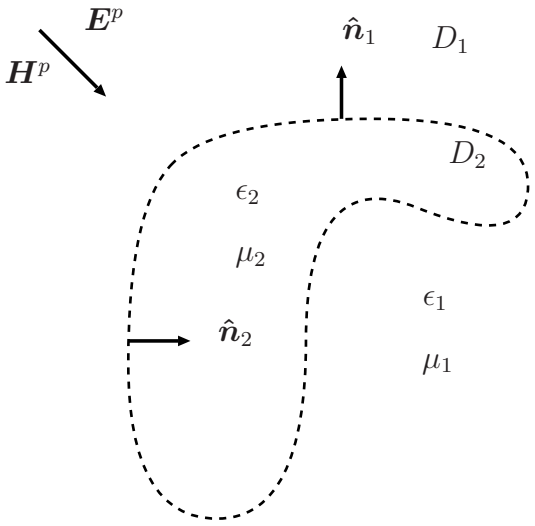

Figure 8: A simple scattering problem with a homogeneous scatterer in a known incident field $\boldsymbol{E}^p$ and $\boldsymbol{H}^p$.

Let's also define the equivalent currents for both sides of the surface S with the aforementioned normal vectors, i.e.

$$\begin{aligned} \boldsymbol{J}_1 &= \hat{\boldsymbol{n}}_1 \times \boldsymbol{H}_1 \\ \boldsymbol{J}_2 &= \hat{\boldsymbol{n}}_2 \times \boldsymbol{H}_2 \\ \boldsymbol{M}_1 &= -\hat{\boldsymbol{n}}_1 \times \boldsymbol{E}_1 \\ \boldsymbol{M}_2 &= -\hat{\boldsymbol{n}}_2 \times \boldsymbol{E}_2. \end{aligned} \tag{3.1}$$

Let's now use relative polarization currents (2.36) to simplify the problem. Let's assume that the sources $\boldsymbol{J}_V^p(\boldsymbol{r})$ and $\rho(\boldsymbol{r})$ of the incident field are in D_1. As was shown in Chapter 2.3.1, the homogeneous scatterer can be replaced by relative polarization

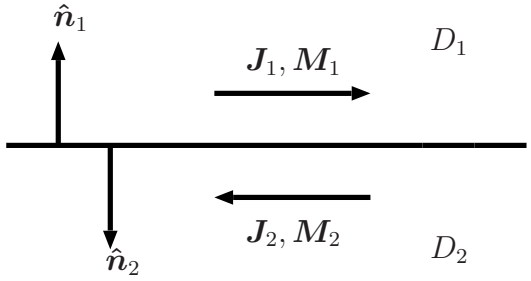

Figure 9: Definition of normal vectors and equivalent surface currents on a surface.

currents $\boldsymbol{J}_{pol,1} = -i\omega\left(\epsilon_2 - \epsilon_1\right)\boldsymbol{E}$ and $\boldsymbol{M}_{pol,1} = -i\omega\left(\mu_2 - \mu_1\right)\boldsymbol{H}$ residing in D_2 after which the space is homogenized with constant material parameters ϵ_1 and μ_1 of D_1.

In order to solve the problem, we now use the representation formulas (2.14) and (2.15) for the scattered field, which has the relative polarization currents $\boldsymbol{J}_{pol,1}$ and $\boldsymbol{M}_{pol,1}$ as sources. The space of this subproblem for the scattered field is now homogeneous with constitutive parameters ϵ_1 and μ_1. Since domain D_1 is outside the sources of the scattered field, the scattered field satisfies the homogeneous Helmholtz equations in D_1 meaning that the scattered field can be represented in D_1 with unknown equivalent surface currents $\boldsymbol{J}_1^s = \hat{\boldsymbol{n}}_1 \times \boldsymbol{H}_1^s$ and $\boldsymbol{M}_1^s = -\hat{\boldsymbol{n}}_1 \times \boldsymbol{E}_1^s$ as

$$\begin{aligned} \Omega_{D_1}\left(\boldsymbol{r}\right)\boldsymbol{E}_1^s\left(\boldsymbol{r}\right) &= \eta_1\mathcal{L}_1\left(\boldsymbol{J}_1^s\right)\left(\boldsymbol{r}\right) - \mathcal{K}_1\left(\boldsymbol{M}_1^s\right)\left(\boldsymbol{r}\right) \\ \Omega_{D_1}\left(\boldsymbol{r}\right)\boldsymbol{H}_1^s\left(\boldsymbol{r}\right) &= \frac{1}{\eta_1}\mathcal{L}_1\left(\boldsymbol{M}_1^s\right)\left(\boldsymbol{r}\right) + \mathcal{K}_1\left(\boldsymbol{J}_1^s\right)\left(\boldsymbol{r}\right). \end{aligned} \tag{3.2}$$

Since we assume that the sources of the incident field are in D_1, which means that the incident field is sourceless in D_2, the representation formulas (2.14) and (2.15) for the domain D_2 can be used for the incident fields with equivalent surface currents $\boldsymbol{J}_1^{\boldsymbol{p}} = \hat{\boldsymbol{n}}_1 \times \boldsymbol{H}_1^p$ and $\boldsymbol{M}_1^{\boldsymbol{p}} = -\hat{\boldsymbol{n}}_1 \times \boldsymbol{E}_1^p$ as

$$\begin{aligned} -\Omega_{D_2}\left(\boldsymbol{r}\right)\boldsymbol{E}_1^p\left(\boldsymbol{r}\right) &= \eta_1\mathcal{L}_1\left(\boldsymbol{J}_1^p\right)\left(\boldsymbol{r}\right) - \mathcal{K}_1\left(\boldsymbol{M}_1^p\right)\left(\boldsymbol{r}\right) \\ -\Omega_{D_2}\left(\boldsymbol{r}\right)\boldsymbol{H}_1^p\left(\boldsymbol{r}\right) &= \frac{1}{\eta_1}\mathcal{L}_1\left(\boldsymbol{M}_1^p\right)\left(\boldsymbol{r}\right) + \mathcal{K}_1\left(\boldsymbol{J}_1^p\right)\left(\boldsymbol{r}\right). \end{aligned} \tag{3.3}$$

The minus sign is needed because the fields in D_2 are represented by the surface currents defined by unit normal vector $\hat{\boldsymbol{n}}_1 = -\hat{\boldsymbol{n}}_2$ pointing into D_1. It's important to note here, that the incident field satisfies the homogeneous Maxwell's equations inside D_2, but with the material parameters of the domain D_1, i.e. it's the field without any scatterer in place. The notations $\mathcal{L}_1$ and $\mathcal{K}_1$ mean the respective integral operators (2.17) and (2.18) with the free space Green's function (2.23) of the homogenized space using the material parameters ϵ_1 and μ_1 of D_1.

If the equations in (3.2) and (3.3) are summed up together, and the incident fields $\boldsymbol{E}_1^p$ and $\boldsymbol{H}_1^p$ are added to the both sides of the respective equations, we get the representation formulas for the total fields $\boldsymbol{E}_1 = \boldsymbol{E}_1^p + \boldsymbol{E}_1^s$ and $\boldsymbol{H}_1 = \boldsymbol{H}_1^p + \boldsymbol{H}_1^s$ in

D_1 as

$$\begin{aligned}\Omega_{D_1}(\boldsymbol{r})\,\boldsymbol{E}_1(\boldsymbol{r}) &= \boldsymbol{E}_1^p(\boldsymbol{r}) + \eta_1\mathcal{L}_1\left(\boldsymbol{J}_1^t\right)(\boldsymbol{r}) - \mathcal{K}_1\left(\boldsymbol{M}_1^t\right)(\boldsymbol{r})\\ \Omega_{D_1}(\boldsymbol{r})\,\boldsymbol{H}_1(\boldsymbol{r}) &= \boldsymbol{H}_1^p(\boldsymbol{r}) + \frac{1}{\eta_1}\mathcal{L}_1\left(\boldsymbol{M}_1^t\right)(\boldsymbol{r}) + \mathcal{K}_1\left(\boldsymbol{J}_1^t\right)(\boldsymbol{r}),\end{aligned} \tag{3.4}$$

where $\boldsymbol{J}_1^t = \boldsymbol{J}_1^p + \boldsymbol{J}_1^s$ and $\boldsymbol{M}_1^t = \boldsymbol{M}_1^p + \boldsymbol{M}_1^s$.

Now we know how to represent the total field outside the scatterer with the unknown equivalent surface currents $\boldsymbol{J}_1^t$ and $\boldsymbol{M}_1^t$. In order to represent the field inside the scatterer, the space can now be homogenized to constant material parameters ϵ_2 and μ_2 by using the relative polarization currents $\boldsymbol{J}_{pol,2}$ and $\boldsymbol{M}_{pol,2}$, which in this case would lie in D_1. The resulting field inside the homogenized space with constitutive parameters of D_2 is sourceless inside D_2, so the representation formulas (2.14) and (2.15) can be directly used for the total fields $\boldsymbol{E}_2$ and $\boldsymbol{H}_2$ inside D_2 as

$$\begin{aligned}\Omega_{D_2}(\boldsymbol{r})\,\boldsymbol{E}_2(\boldsymbol{r}) &= \eta_2\mathcal{L}_2(\boldsymbol{J}_2)(\boldsymbol{r}) - \mathcal{K}_2(\boldsymbol{M}_2)(\boldsymbol{r})\\ \Omega_{D_2}(\boldsymbol{r})\,\boldsymbol{H}_2^t(\boldsymbol{r}) &= \frac{1}{\eta_2}\mathcal{L}_2(\boldsymbol{M}_2)(\boldsymbol{r}) + \mathcal{K}_2(\boldsymbol{J}_2)(\boldsymbol{r}).\end{aligned} \tag{3.5}$$

The continuity properties (2.10) of the fields and equations (2.27) force for the equivalent surface currents $\boldsymbol{J}_1 = \boldsymbol{J}_1^t$ and $\boldsymbol{M}_1 = \boldsymbol{M}_1^t$ the continuity requirements

$$\begin{aligned}\boldsymbol{J}_1 &= -\boldsymbol{J}_2\\ \boldsymbol{M}_1 &= -\boldsymbol{M}_2.\end{aligned} \tag{3.6}$$

A piecewise homogeneous problem with multiple domains is just a generalization of this problem with two domains. The field inside each homogeneous subdomain D_i can be represented as sum of the incident field inside the domain and the field of the unknown equivalent surface current densities $\boldsymbol{J}_i$ and $\boldsymbol{M}_i$ on the boundary surface of the domain.

If any of the subdomains D_i of a piecewise homogeneous problem is perfectly conducting, the field inside such domains would be zero. Since the representation formulas (2.14) and (2.15) give zero field to the complement of the representation space, the requirement of the zero field is directly fulfilled by just using the equivalent surface currents to represent the field outside the perfectly conducting domain and by using the boundary conditions similar to (2.12) to simplify the representation formulas. The field inside the perfectly conducting domains need not be represented.

3.2 Surface integral equations

The surface equivalence principle and results of Chapter 3.1 show how the fields in a piecewise homogeneous medium can be represented as integrals of the unknown surface currents over the material interface surfaces. The unknown surface currents $\boldsymbol{J}$ and $\boldsymbol{M}$ can be solved by finding the surface current distributions that give the

fields that satisfy the continuity requirements and the boundary conditions for the total fields. Since these requirements are set at the material interfaces, it implies that the surface integrals need to be evaluated at the same surfaces as the unknown surface currents in order to develop valid surface integral equations that can be used to find correct surface current distributions.

Here we go through some of the most important integral equations. These equations can then be used as building blocks to develop integral equation formulations applicable to different kinds of electromagnetic problems with different kinds of boundary conditions. Some of the formulations are presented in Chapter 3.3

On a material interface surface S, one can either find the tangential components or the normal component of the represented fields. Since any problem of time harmonic electromagnetics has unique solution if the tangential fields are known on a closed surface, most of the formulations use only tangential components [13].

3.2.1 Tangential equations

Representation formulas (3.4) and (3.5) can also be used on a material interface surface S, where the relative solid angle is $\Omega_D = \frac{1}{2}$ for any smooth surface. For a general vector field $\boldsymbol{F}(\boldsymbol{r})$ we get the tangential component $\boldsymbol{F}_{tan}(\boldsymbol{r})$ on a surface with unit normal vector $\hat{\boldsymbol{n}}(\boldsymbol{r})$ by

$$\boldsymbol{F}_{tan}(\boldsymbol{r}) = -\hat{\boldsymbol{n}}(\boldsymbol{r}) \times \hat{\boldsymbol{n}}(\boldsymbol{r}) \times \boldsymbol{F}(\boldsymbol{r}), \tag{3.7}$$

which further gives us

$$\begin{aligned} \boldsymbol{E}_{tan} &= \hat{\boldsymbol{n}} \times \boldsymbol{M} \\ \boldsymbol{H}_{tan} &= -\hat{\boldsymbol{n}} \times \boldsymbol{J}. \end{aligned} \tag{3.8}$$

If we pick up the tangential components of equations (3.4) on the surface S and use (3.8), we get the tangential surface integral equations for the fields as

$$\eta_1 \mathcal{L}_1(\boldsymbol{J}_1)(\boldsymbol{r})_{tan} - \mathcal{K}_1(\boldsymbol{M}_1)(\boldsymbol{r})_{tan} - \frac{1}{2}\hat{\boldsymbol{n}}_1 \times \boldsymbol{M}_1(\boldsymbol{r}) = -\boldsymbol{E}_1^p(\boldsymbol{r})_{tan} \tag{3.9}$$

$$\frac{1}{\eta_1}\mathcal{L}_1(\boldsymbol{M}_1)(\boldsymbol{r})_{tan} + \mathcal{K}_1(\boldsymbol{J}_1)(\boldsymbol{r})_{tan} + \frac{1}{2}\hat{\boldsymbol{n}}_1 \times \boldsymbol{J}_1(\boldsymbol{r}) = -\boldsymbol{H}_1^p(\boldsymbol{r})_{tan}. \tag{3.10}$$

These are referred to as T-EFIE$_1$ and T-MFIE$_1$ [14], because these are equations for the tangential electric field $\boldsymbol{E}_{tan}$ and tangential magnetic field $\boldsymbol{H}_{tan}$ in D_1. Similar equations are also obtained for the fields in D_2 with the integral operators of D_2 and incident fields $\boldsymbol{E}_2^p = \boldsymbol{0}$ and $\boldsymbol{H}_2^p = \boldsymbol{0}$, since the sources of the incident field are assumed to be in D_1. This can also be generalized to a piecewise homogeneous multidomain problem with notations T-EFIE$_i$ and T-MFIE$_i$. It is important to note, that these equations only fix the tangential fields on the surface S. Normal components of the

fields are not directly fixed. However, once the tangential components are fixed, the normal components are obtained with continuity equations (2.27) excluding the low frequency limit $\omega = 0$.

3.2.2 N-equations

Tangential components of the fields on a material interface surface S can also be fixed by operating with $\hat{\boldsymbol{n}}\times$ on both sides of equations (3.4) and (3.5) on the surface S to get surface integral equations

$$\eta_1 \hat{\boldsymbol{n}}_1 \times \mathcal{L}_1 (\boldsymbol{J}_1)(\boldsymbol{r}) - \hat{\boldsymbol{n}}_1 \times \mathcal{K}_1 (\boldsymbol{M}_1)(\boldsymbol{r}) + \frac{1}{2}\boldsymbol{M}_1(\boldsymbol{r}) = -\hat{\boldsymbol{n}}_1 \times \boldsymbol{E}_1^p(\boldsymbol{r}) \quad (3.11)$$

$$\frac{1}{\eta_1}\hat{\boldsymbol{n}}_1 \times \mathcal{L}_1 (\boldsymbol{M}_1)(\boldsymbol{r}) + \hat{\boldsymbol{n}}_1 \times \mathcal{K}_1 (\boldsymbol{J}_1)(\boldsymbol{r}) - \frac{1}{2}\boldsymbol{J}_1(\boldsymbol{r}) = -\hat{\boldsymbol{n}}_1 \times \boldsymbol{H}_1^p(\boldsymbol{r}). \quad (3.12)$$

These are referred to as N-EFIE$_1$ and N-MFIE$_1$ [14], because these are equations for $\hat{\boldsymbol{n}} \times \boldsymbol{E}$ and $\hat{\boldsymbol{n}} \times \boldsymbol{H}$ in D_1. Similar to tangential equations, the N-equations can be generalized to a piecewise homogeneous multidomain problem with notations N-EFIE$_i$ and N-MFIE$_i$.

3.3 Integral equation formulations

Integral equations defined in Chapter 3.2 can be used to introduce integral equation formulations applicable to different kinds of problems. Mostly the choice of formulation is dependent of the material properties and geometrical shapes. Here we go through some of the most important formulations for different situations.

3.3.1 PEC surfaces

On a PEC surface, i.e. a surface of metal with infinite conductivity σ, the boundary condition states that the total tangential electric field $\boldsymbol{E}_{tan}$ vanishes. This means that the unknowns associated to $\boldsymbol{M} = -\hat{\boldsymbol{n}} \times \boldsymbol{E}$ can be removed. This simplifies equations (3.9)-(3.12) into

$$\eta_1 \mathcal{L}_1 (\boldsymbol{J}_1)(\boldsymbol{r})_{tan} = -\boldsymbol{E}_1^p(\boldsymbol{r})_{tan} \quad (3.13)$$

$$\mathcal{K}_1 (\boldsymbol{J}_1)(\boldsymbol{r})_{tan} + \frac{1}{2}\hat{\boldsymbol{n}}_1 \times \boldsymbol{J}_1(\boldsymbol{r}) = -\boldsymbol{H}_1^p(\boldsymbol{r})_{tan} \quad (3.14)$$

$$\eta_1 \hat{\boldsymbol{n}}_1 \times \mathcal{L}_1 (\boldsymbol{J}_1)(\boldsymbol{r}) = -\hat{\boldsymbol{n}}_1 \times \boldsymbol{E}_1^p(\boldsymbol{r}) \quad (3.15)$$

$$\hat{\boldsymbol{n}}_1 \times \mathcal{K}_1 (\boldsymbol{J}_1)(\boldsymbol{r}) - \frac{1}{2}\boldsymbol{J}_1(\boldsymbol{r}) = -\hat{\boldsymbol{n}}_1 \times \boldsymbol{H}_1^p(\boldsymbol{r}). \quad (3.16)$$

PEC can be undestood as a limit of the impedance boundary condition (2.40) with the surface impedance $Z_s = 0$. The impedance boundary condition itself shows

that the tangential electric field $\boldsymbol{E}_{tan}$ and the electric surface current $\boldsymbol{J}$ on a well conducting surface are equally directed. This means that the scattered field on the left hand side of (3.13) (i.e. the range of $\mathcal{L}_1\left(\boldsymbol{J}_1\right)\left(\boldsymbol{r}\right)_{tan}$) is equally directed to $\boldsymbol{J}$, what is desired. This can also be understood by the plane waves. Equations $1/\eta_1*$(3.13) and (3.16) have the same dimensions as $\boldsymbol{J}$ and are equally directed to $\boldsymbol{J}$ and hence they are used with PEC surfaces. Equations (3.15) and η_1*(3.14) have the same dimensions as $\boldsymbol{M}$, which is zero on a PEC surface, and therefore they are not adequate for PEC surfaces [14].

If the dimensions of a PEC domain are such that an internal resonant solution would occur inside similar metallic volume filled with the material outside the PEC volume, both T-EFIE (3.13) and N-MFIE (3.16) fail to give good results. This is simply because resonant solutions can satisfy the PEC boundary condition $\boldsymbol{E}_{tan} = \boldsymbol{0}$ also with the field inside the volume not being zero, as would be needed for the PEC volume. In order to guarantee that the field inside the PEC domain is zero, one needs to use both of these equations at least in some part of the PEC boundary [15]. The weighted sum of these two is the CFIE formulation, which is defined as

$$\text{CFIE} = \frac{1}{\eta_1}\left(\text{T}-\text{EFIE}\right) + \left(\text{N}-\text{MFIE}\right) \tag{3.17}$$

3.3.2 Lossy metallic surfaces

PEC boundary is an approximation of the real boundary condition on a metal surface. In reality, the conductivity of a metal is finite, which means that the tangential electric field isn't exactly zero. The normal component of the magnetic flux also doesn't perfectly vanish.

Impedance boundary condition can be used to approximate the effects of finite conductivity on metallic surfaces. Impedance boundary condition (2.40) can be modified into

$$\boldsymbol{M} = -Z_s\hat{\boldsymbol{n}}\times\hat{\boldsymbol{n}}\times\boldsymbol{H} = -Z_s\hat{\boldsymbol{n}}\times\boldsymbol{J}. \tag{3.18}$$

Substituting this into T-EFIE (3.9) and N-MFIE (3.12) results as IBC-EFIE

$$\eta_1\mathcal{L}_1\left(\boldsymbol{J}_1\right)\left(\boldsymbol{r}\right)_{tan} + \mathcal{K}_1\left(Z_s\hat{\boldsymbol{n}}_1\times\boldsymbol{J}_1\right) - \frac{1}{2}Z_s\left(\boldsymbol{r}\right)\boldsymbol{J}_1\left(\boldsymbol{r}\right) = -\boldsymbol{E}_1^p\left(\boldsymbol{r}\right)_{tan} \tag{3.19}$$

and IBC-MFIE

$$-\frac{1}{\eta_1}\hat{\boldsymbol{n}}_1\times\mathcal{L}_1\left(Z_s\hat{\boldsymbol{n}}_1\times\boldsymbol{J}_1\right)\left(\boldsymbol{r}\right) + \hat{\boldsymbol{n}}_1\times\mathcal{K}_1\left(\boldsymbol{J}_1\right)\left(\boldsymbol{r}\right) - \frac{1}{2}\boldsymbol{J}_1\left(\boldsymbol{r}\right) = -\hat{\boldsymbol{n}}_1\times\boldsymbol{H}_1^p\left(\boldsymbol{r}\right) \tag{3.20}$$

which can both be used to solve the equivalent surface current $\boldsymbol{J}$ on a lossy metallic surface.

Similar to PEC surfaces, both IBC-EFIE and IBC-MFIE fail to give good results at internal resonant frequencies. In order to avoid the resonance problems, a combined field integral equation similar to CFIE (3.17) can be used. This results as IBC-CFIE

$$\mathrm{IBC-CFIE} = \frac{1}{\eta_1}\left(\mathrm{IBC-EFIE}\right) + \left(\mathrm{IBC-MFIE}\right). \tag{3.21}$$

The losses of real metals are often quite small and the resulting surface impedance typically doesn't alter the surface current $\boldsymbol{J}$ very much. Thus, in this thesis the problems with metallic structures are solved with the PEC assumption. The effect of the impedance boundary is only included as an added loss power (2.42), which is approximated with $\boldsymbol{J}_{PEC}$, i.e. the electric surface current of the problem solved with PEC assumption on metallic surfaces.

3.3.3 Dielectric surfaces

On general dielectric surface, there are no other boundary conditions than the continuity requirements (2.10). The continuities themself result as the continuity requirement of the equivalent surface currents (3.6). By properly combining electric and magnetic field integral equations on both sides of the material interface, a combined formulation free of internal resonances is obtained [13]. These combinations can be made in infinitely many ways [16, 14].

In this thesis we use so called Poggio-Miller-Chang-Harrington-Wu-Tsai (PMCHWT) formulation on the dielectric surfaces. The PMCHWT formulation [17, 18, 19] on a surface between two dielectric domains D_i and D_j is an equation system

$$\begin{matrix}\left(\mathrm{T-EFIE}_i\right) - \left(\mathrm{T-EFIE}_j\right) \\ \left(\mathrm{T-MFIE}_i\right) - \left(\mathrm{T-MFIE}_j\right)\end{matrix} \tag{3.22}$$

which results for T-EFIE part as

$$\begin{matrix}\eta_i\mathcal{L}_i\left(\boldsymbol{J}_i\right)_{tan} - \eta_j\mathcal{L}_j\left(\boldsymbol{J}_j\right)_{tan} \\ -\mathcal{K}_i\left(\boldsymbol{M}_i\right)_{tan} + \mathcal{K}_j\left(\boldsymbol{M}_j\right)_{tan} \\ -\frac{1}{2}\hat{\boldsymbol{n}}_i\times\boldsymbol{M}_i + \frac{1}{2}\hat{\boldsymbol{n}}_j\times\boldsymbol{M}_j = -\boldsymbol{E}_i^p\left(\boldsymbol{r}\right)_{tan}\end{matrix} \tag{3.23}$$

and for T-MFIE part as

$$\begin{matrix}\frac{1}{\eta_i}\mathcal{L}_i\left(\boldsymbol{M}_i\right)\left(\boldsymbol{r}\right)_{tan} - \frac{1}{\eta_j}\mathcal{L}_j\left(\boldsymbol{M}_j\right)\left(\boldsymbol{r}\right)_{tan} \\ +\mathcal{K}_i\left(\boldsymbol{J}_i\right)\left(\boldsymbol{r}\right)_{tan} - \mathcal{K}_j\left(\boldsymbol{J}_j\right)\left(\boldsymbol{r}\right)_{tan} \\ +\frac{1}{2}\hat{\boldsymbol{n}}_i\times\boldsymbol{J}_i\left(\boldsymbol{r}\right) - \frac{1}{2}\hat{\boldsymbol{n}}_j\times\boldsymbol{J}_j\left(\boldsymbol{r}\right) = -\boldsymbol{H}_i^p\left(\boldsymbol{r}\right)_{tan}\end{matrix} \tag{3.24}$$

if the incident fields $\boldsymbol{E}_i^p$ and $\boldsymbol{H}_i^p$ are assumed to be in the domain D_i. The continuity

(3.6) of the surface currents and definition of the normal vectors as $\hat{\boldsymbol{n}}_j = -\hat{\boldsymbol{n}}_i$ reduces the equations into

$$\begin{aligned} \left(\eta_i \mathcal{L}_i + \eta_j \mathcal{L}_j\right)\left(\boldsymbol{J}_i\right)\left(\boldsymbol{r}\right)_{tan} - \left(\mathcal{K}_i + \mathcal{K}_j\right)\left(\boldsymbol{M}_i\right)\left(\boldsymbol{r}\right)_{tan} &= -\boldsymbol{E}_i^p\left(\boldsymbol{r}\right)_{tan} \\ \left(\frac{1}{\eta_i}\mathcal{L}_i + \frac{1}{\eta_j}\mathcal{L}_j\right)\left(\boldsymbol{M}_i\right)\left(\boldsymbol{r}\right)_{tan} + \left(\mathcal{K}_i + \mathcal{K}_j\right)\left(\boldsymbol{J}_i\right)\left(\boldsymbol{r}\right)_{tan} &= -\boldsymbol{H}_i^p\left(\boldsymbol{r}\right)_{tan}. \end{aligned} \tag{3.25}$$

The PMCHWT formulation basically states that $\boldsymbol{E}^s_{tan,i} - \boldsymbol{E}^s_{tan,j} = -\boldsymbol{E}^p_i$ and $\boldsymbol{H}^s_{tan,i} - \boldsymbol{H}^s_{tan,j} = -\boldsymbol{H}^p_i$, i.e. the continuity of the tangential fields (2.10) through the dielectric material interface, since the total fields in D_i are $\boldsymbol{E}_i = \boldsymbol{E}^p_i + \boldsymbol{E}^s_i$ and $\boldsymbol{H}_i = \boldsymbol{H}^p_i + \boldsymbol{H}^s_i$ and in D_j they are $\boldsymbol{E}_j = \boldsymbol{E}^s_j$ and $\boldsymbol{H}_j = \boldsymbol{H}^s_j$.

3.3.4 General problems

The PMCHWT is a natural choice of formulation for dielectric surfaces in the computation of general problems with composite metallic and dielectric structures. The T-EFIE as used on PEC surfaces and T-MFIE, which would be used on PMC surfaces, are included in the PMCHWT formulation, which means that formulations on both PEC and PMC surfaces are special cases of the formulation on dielectric surface.

A general problem can consist of metallic PEC domains D^e_i, PMC domains D^m_j and dielectric domains D_k. The problem is solved with PMCHWT on surfaces between two dielectric domains. On surfaces between a PEC domain D^e_i and a dielectric domain D_k, the PMCHWT is reduced into T-EFIE$_k$ with $\boldsymbol{M}_k = \boldsymbol{0}$. Similarly on surfaces between a PMC domain D^m_j and a dielectric domain D_k, the PMCHWT is reduced into T-MFIE$_k$ with $\boldsymbol{J}_k = \boldsymbol{0}$. This results as an integral equation system that can be used to solve general problems.

4 Numerical solutions of surface integral equations

It would be very hard to find analytical solutions for the above mentioned surface integral equations in general case. A much easier option is to find a numerical solution to the problem. Method of moments with correct sets of basis functions and testing functions has been used succesfully to solve the equivalent currents from the resulting integral equations. In this chapter the choice of basis and testing functions is clarified and the procedures needed to compute the resulting MoM system matrix are also treated.

4.1 Method of moments for EM field problems

This chapter includes a new look to the classical method of moments. The testing procedure, which is classically rationalized as a generalization of the point matching method [11] receives a new interpretation in this chapter.

Method of moments first needs the set of basis functions to represent the unknown. In the case of the electromagnetic surface integral equations, the unknowns are the domain specific equivalent electric and magnetic surface current densities $\boldsymbol{J}_D = \hat{\boldsymbol{n}} \times \boldsymbol{H}_D$ and $\boldsymbol{M}_D = -\hat{\boldsymbol{n}} \times \boldsymbol{E}_D$ lying on a surface $S_D = \partial D$ between domain D and any other domain. Since the equivalent surface currents are tangential to S_D, they can be approximated as a linear combination of tangential basis functions $\boldsymbol{b}_j^{J_D}$ and $\boldsymbol{b}_m^{M_D}$ as

$$\begin{aligned} \boldsymbol{J}_D(\boldsymbol{r}) &\approx \sum_{j=1}^{N_j^D} J_j^D \boldsymbol{b}_j^{J_D}(\boldsymbol{r}), \qquad \boldsymbol{r} \in \partial D \\ \boldsymbol{M}_D(\boldsymbol{r}) &\approx \sum_{m=1}^{N_m^D} M_m^D \boldsymbol{b}_m^{M_D}(\boldsymbol{r}), \qquad \boldsymbol{r} \in \partial D. \end{aligned} \tag{4.1}$$

Domain specific surface currents must fulfil the continuity requirements (3.6). This is attained by defining the basis functions for domain specific surface current densities simply as

$$\begin{aligned} \boldsymbol{b}_j^{J_{D2}} &= -\boldsymbol{b}_j^{J_{D1}} \\ \boldsymbol{b}_m^{M_{D2}} &= -\boldsymbol{b}_m^{M_{D1}} \end{aligned} \tag{4.2}$$

on a surface between domains $D1$ and $D2$, and requiring that the unknown coefficients related to the two basis functions are equal by combining the respective

coefficients as single unknowns [20]

$$\begin{aligned} J_{nj} &= J_j^{D1} = J_j^{D2} \\ M_{nm} &= M_m^{D1} = M_m^{D2}. \end{aligned} \tag{4.3}$$

By substituting the approximations (4.1) to the surface integral equations (3.9) and (3.10) we get

$$\eta_D \sum_{j=1}^{N_j^D} J_j^D \mathcal{L}_D \left(\boldsymbol{b}_j^{J_D}\right)_{tan} - \sum_{m=1}^{N_m^D} M_m^D \left(\mathcal{K}_D \left(\boldsymbol{b}_m^{M_D}\right)_{tan} + \frac{1}{2}\hat{\boldsymbol{n}} \times \boldsymbol{b}_m^{M_D}\right) = -\boldsymbol{E}_{D,tan}^p \tag{4.4}$$

$$\frac{1}{\eta_D} \sum_{m=1}^{N_m^D} M_m^1 \mathcal{L}_D \left(\boldsymbol{b}_m^{M_D}\right)_{tan} + \sum_{j=1}^{N_j^D} J_j^D \left(\mathcal{K}_D \left(\boldsymbol{b}_j^{J_D}\right)_{tan} + \frac{1}{2}\hat{\boldsymbol{n}} \times \boldsymbol{b}_j^{J_D}\right) = -\boldsymbol{H}_{D,tan}^p \tag{4.5}$$

Since the integral operators $\mathcal{L}_D$ and $\mathcal{K}_D$ are linear, the summations can be moved outside the integral operators as has already been done.

In order to avoid a mess with discrete unknowns and continuous incident fields, the testing procedure is introduced. Let's approximate the incident fields $\boldsymbol{E}_{D,tan}^p(\boldsymbol{r})$ and $\boldsymbol{H}_{D,tan}^p(\boldsymbol{r})$ as a linear combination of tangential testing functions $\boldsymbol{t}_e^{E_D}$ and $\boldsymbol{t}_h^{H_D}$ as

$$\boldsymbol{E}_{D,tan}^p(\boldsymbol{r}) = \sum_{e=1}^{M_e^D} E_e^D \boldsymbol{t}_e^{E_D}(\boldsymbol{r}), \qquad \boldsymbol{r} \in S \tag{4.6}$$

$$\boldsymbol{H}_{D,tan}^p(\boldsymbol{r}) = \sum_{h=1}^{M_h^D} H_h^D \boldsymbol{t}_h^{H_D}(\boldsymbol{r}), \qquad \boldsymbol{r} \in S. \tag{4.7}$$

Let's define inner product between two vector functions $\boldsymbol{f}(\boldsymbol{r})$ and $\boldsymbol{g}(\boldsymbol{r})$ on a surface S as

$$\langle \boldsymbol{f}, \boldsymbol{g} \rangle = \int_S \boldsymbol{f}(\boldsymbol{r}) \cdot \boldsymbol{g}(\boldsymbol{r}) \, \mathrm{d}S \tag{4.8}$$

The coefficients E_e^D and H_h^D in the series representations of $\boldsymbol{E}_{D,tan}^p(\boldsymbol{r})$ and $\boldsymbol{H}_{D,tan}^p(\boldsymbol{r})$ are calculated by inner products as

$$E_e^D = \frac{1}{\alpha_e^D} \left\langle \boldsymbol{t}_e^{E_D}, \boldsymbol{E}_D^p \right\rangle = \frac{1}{\alpha_e^D} \int_{S_e} \boldsymbol{t}_e^{E_D}(\boldsymbol{r}) \cdot \boldsymbol{E}_D^p(\boldsymbol{r}) \, \mathrm{d}S \tag{4.9}$$

$$H_h^D = \frac{1}{\beta_h^D} \left\langle \boldsymbol{t}_h^{H_D}, \boldsymbol{H}_D^p \right\rangle = \frac{1}{\beta_h^D} \int_{S_h} \boldsymbol{t}_h^{H_D}(\boldsymbol{r}) \cdot \boldsymbol{H}_D^p(\boldsymbol{r}) \, \mathrm{d}S. \tag{4.10}$$

The coefficients α_e^D and β_h^D are just the normalization coefficients

$$\alpha_e^D = \left\langle \boldsymbol{t}_e^{E_D}, \boldsymbol{t}_e^{E_D} \right\rangle$$
$$\beta_h^D = \left\langle \boldsymbol{t}_h^{H_D}, \boldsymbol{t}_h^{H_D} \right\rangle .$$

If the equivalent inner pruducts with testing functions $\boldsymbol{t}_m^{E_D}$ or $\boldsymbol{t}_m^{H_D}$ are calculated also for the left hand sides of the respective equations (4.4) and (4.5), and the series representations (4.6) and (4.7) are substituted to $\boldsymbol{E}_{D,tan}^p$ and $\boldsymbol{H}_{D,tan}^p$ of the same equations we get

$$\begin{aligned}
&\frac{\eta_D}{\alpha_e^D} \sum_{j=1}^{N_j^D} J_j^D \left\langle \boldsymbol{t}_e^{E_D}, \mathcal{L}_D\left(\boldsymbol{b}_j^{J_D}\right) \right\rangle - \frac{1}{\alpha_e^D} \sum_{m=1}^{N_m^D} M_m^D \left\langle \boldsymbol{t}_e^{E_D}, \mathcal{K}_D\left(\boldsymbol{b}_m^{M_D}\right) + \frac{1}{2}\hat{\boldsymbol{n}} \times \boldsymbol{b}_m^{M_D} \right\rangle = -E_e^D \\
&\frac{1}{\beta_h^D \eta} \sum_{m=1}^{N_m^D} M_m^D \left\langle \boldsymbol{t}_h^{H_D}, \mathcal{L}_D\left(\boldsymbol{b}_m^{M_D}\right) \right\rangle + \frac{1}{\beta_h^D} \sum_{j=1}^{N_j^D} J_j^D \left\langle \boldsymbol{t}_h^{H_D}, \mathcal{K}_D\left(\boldsymbol{b}_j^{J_D}\right) + \frac{1}{2}\hat{\boldsymbol{n}} \times \boldsymbol{b}_j^{J_D} \right\rangle = -H_h^D
\end{aligned} \tag{4.11}$$

Since the normalization coefficients α_e^D and β_h^D are on both sides of the respective equations, they can be ignored. The equations (4.11) must be satisfied with every $e = 1, \ldots, M_e^D$ and $h = 1, \ldots, M_h^D$. If the basis functions are able to represent the equivalent surface currents accurately and the testing functions are able to represent both the incident fields and the ranges of the surface integral operators, the results of this numerical treatment should be accurate.

In this thesis the PMCHWT formulation is used for dielectric boundaries and the T-EFIE formulation is used for perfectly conducting surfaces. This means that the terms including $\hat{\boldsymbol{n}} \times \boldsymbol{b}_m^M$ and $\hat{\boldsymbol{n}} \times \boldsymbol{b}_j^J$ will be cancelled out in the total system of equations, so they can be ignored altogether. The PMCHWT formulation on a surface between two dielectric domains $D1$ and $D2$ is basically the equation system of (T-EFIE$_{D1}$) - (T-EFIE$_{D2}$) and (T-MFIE$_{D1}$) - (T-MFIE$_{D2}$). Let's define domain specific testing functions simply as

$$\begin{aligned}
\boldsymbol{t}_e^{E_{D2}} &= -\boldsymbol{t}_e^{E_{D1}} \\
\boldsymbol{t}_h^{H_{D2}} &= -\boldsymbol{t}_h^{H_{D1}}
\end{aligned} \tag{4.12}$$

on a surface between domains $D1$ and $D2$. This definition also fulfils the Galerkin method requirement of the set of testing functions being the same as the set of basis functions, since a similar definition was also used for the basis functions (4.2).

Now let the integral equations for the fields in $D1$ be tested with $\boldsymbol{t}_e^{E_{D1}}$ and $\boldsymbol{t}_h^{H_{D1}}$. Similarly let the integral equations for the fields in $D2$ be tested with $\boldsymbol{t}_e^{E_{D2}}$ and $\boldsymbol{t}_h^{H_{D2}}$. The PMCHWT formulation is given by simply adding up the contributions of (4.11) for both of the domains $D1$ and $D2$ with the domain specific testing functions of the dielectric domains around a dielectric surface.

Testing of equations with the domain specific testing functions (4.12) and addition of the contributions effectively combines the two testings as a single testing. The subtraction of the two field representations of the PMCHWT formulation (3.22) is transformed into addition simply because of the definition of the domain specific testing functions (4.12). This way to test the equations with domain specific testing functions closely resembles the treatment in [20] and is also applicable to problems with junctions, i.e. material interfaces with more than two domains around some parts of the material interfaces [13], and as such is a solution to the junction problem pointed out in [21].

The T-EFIE formulation on PEC surfaces (3.13) is a special case of the PMCHWT formulation without unknowns and testing for the PEC domain and without magnetic testing functions $\boldsymbol{t}_h^{H_D}$ and magnetic basis functions $\boldsymbol{b}_m^{M_D}$ for the domains surrounding the PEC. Assuming that only two dielectric domains exist for the problem, the resulting system matrix of the T-EFIE-PMCHWT formulation for the two dielectric domains $D1$ and $D2$ can of course be represented in matrix form as

$$\boldsymbol{A}x = b, \tag{4.13}$$

where the system matrix $\boldsymbol{A}$ consists of

$$A = \begin{bmatrix} \boldsymbol{A}_{EJ} & \boldsymbol{A}_{EM} \\ \boldsymbol{A}_{HJ} & \boldsymbol{A}_{HM} \end{bmatrix}$$

with the submatrices

$$\begin{aligned}
\boldsymbol{A}_{EJ}\,(\mathrm{e},\mathrm{j}) &= \left\langle \boldsymbol{t}_e^{E_{D1}}, \eta_{D1}\mathcal{L}_{D1}\left(\boldsymbol{b}_j^{J_{D1}}\right)\right\rangle + \left\langle \boldsymbol{t}_e^{E_{D2}}, \eta_{D2}\mathcal{L}_{D2}\left(\boldsymbol{b}_j^{J_{D2}}\right)\right\rangle \\
\boldsymbol{A}_{EM}\,(\mathrm{e},\mathrm{m}) &= -\left\langle \boldsymbol{t}_e^{E_{D1}}, \mathcal{K}_{D1}\left(\boldsymbol{b}_m^{M_{D1}}\right)\right\rangle - \left\langle \boldsymbol{t}_e^{E_{D2}}, \mathcal{K}_{D2}\left(\boldsymbol{b}_m^{M_{D2}}\right)\right\rangle \\
\boldsymbol{A}_{HJ}\,(\mathrm{h},\mathrm{j}) &= \left\langle \boldsymbol{t}_h^{H_{D1}}, \mathcal{K}_{D1}\left(\boldsymbol{b}_j^{J_{D1}}\right)\right\rangle + \left\langle \boldsymbol{t}_h^{H_{D2}}, \mathcal{K}_{D2}\left(\boldsymbol{b}_j^{J_{D2}}\right)\right\rangle \\
\boldsymbol{A}_{HM}\,(\mathrm{h},\mathrm{m}) &= \left\langle \boldsymbol{t}_h^{H_{D1}}, \tfrac{1}{\eta_{D1}}\mathcal{L}_{D1}\left(\boldsymbol{b}_m^{M_{D1}}\right)\right\rangle + \left\langle \boldsymbol{t}_{eh}^{H_{D2}}, \tfrac{1}{\eta_{D2}}\mathcal{L}_{D2}\left(\boldsymbol{b}_m^{M_{D2}}\right)\right\rangle
\end{aligned} \tag{4.14}$$

$$x = \begin{bmatrix} J_1 \\ \vdots \\ J_{N_j} \\ M_1 \\ \vdots \\ M_{N_m} \end{bmatrix}$$

$$b = \begin{bmatrix} \left\langle \boldsymbol{t}_1^{E_{D1}}, \boldsymbol{E}^p \right\rangle \\ \vdots \\ \left\langle \boldsymbol{t}_{M_e}^{E_{D1}}, \boldsymbol{E}^p \right\rangle \\ \left\langle \boldsymbol{t}_1^{H}, \boldsymbol{H}^p \right\rangle \\ \vdots \\ \left\langle \boldsymbol{t}_{M_h}^{H}, \boldsymbol{H}^p \right\rangle \end{bmatrix}$$

On PEC surfaces, the T-EFIE system matrix is $\boldsymbol{A}_{EJ}$ with the unknowns and testing inside the PEC domain removed.

In order to get an equally determined system, the number of degrees of freedom $N_j + N_m$ for the unknowns should match the number of testing functions $M_e + M_h$ everytime. This means that the number of basis functions for $\boldsymbol{J}$ should match the number of electric testing functions and the number of basis functions for $\boldsymbol{M}$ should match the number of magnetic testing functions, i.e.

$$\begin{aligned} N_j &= M_e \\ N_m &= M_h \end{aligned} \tag{4.15}$$

which then gives $e = 1, \ldots, M_e$, $j = 1, \ldots, N_j$, $h = 1, \ldots, M_h$, $m = 1, \ldots, N_m$.

This is naturally achieved when the Galerkin method is used, which is the case in this thesis. The basis and testing functions that will be used are clarified in the next section.

4.2 Basis functions and geometry discretization

The method of moments requires the representations of the equivalent surface current densities $\boldsymbol{J}$ and $\boldsymbol{M}$ as linear combination of known basis functions $\boldsymbol{b}_j^J$ and $\boldsymbol{b}_m^M$. In rare cases such as on the surface of a homogeneous sphere [37], the equivalent currents can be analytically represented as sum of special characteristic functions. Most of the time the optimal choice of basis functions in such cases would be to choose a finite subset of the characteristic functions as a set of basis functions. For an arbitrary geometry a more versatile option is to discretize the surfaces of the geometry by representing the geometry as an union of canonical geometrical elements and by developing the basis functions for the discretized geometries.

The simplest discretization of surfaces is the linear discretization, where the surface is divided into finite number of non-overlapping planar polygons. The simplest and most versatile linear discretization of surfaces is attained by using triangles. Triangles can represent a curved surface such as surface of a sphere better than e.g. quadrangles. Numerics is also simpler for triangles, so the triangular geometry discretization will be used in this thesis.

In a homogeneous media outside the sources, all the field components are always continuous. This means that on a smooth surface between two homogeneous domains

the tangential field components are continuous on both sides of the surface. Even if two neighboring triangles of a triangulated surface are not on a same plane, they still share an edge. This continuity of the tangential EM fields implies that the field components parallel to the edges are continuous through the edges. Since the surface current densities $\boldsymbol{J}$ and $\boldsymbol{M}$ are 90 degrees rotated tangential fields, the components of $\boldsymbol{J}$ and $\boldsymbol{M}$ perpendicular to the edges are continuous. In order to get good results, the basis functions of (4.1) representing $\boldsymbol{J}$ and $\boldsymbol{M}$ should have this continuity property.

In addition to the continuity requirements of the basis functions, the basis functions of $\boldsymbol{J}$ and $\boldsymbol{M}$ should also have well defined surface divergence, because the integral operator $\mathcal{L}$ (2.17) needs the surface divergence of the equivalent surface current densities. The ability to represent the surface divergence and continuity of the basis function component perpendicular to all the edges of the triangular mesh are the requirements for the basis functions $\boldsymbol{b}^J$ and $\boldsymbol{b}^M$ in (4.1).

4.2.1 RWG functions

Undoubtedly the most used basis functions for electromagnetic surface integral equations with Galerkin method in triangular meshes are the RWG-functions [12]. The RWG-functions are related to a single edge of the triangular mesh at a time. The RWG-function for the particular edge is other than zero only on the two triangles T^+ and T^- that share the edge. The RWG-function $\boldsymbol{f}_n$ for the edge n can be calculated as

$$\boldsymbol{f}_n(\boldsymbol{r}) = \begin{cases} \frac{L_n}{2A_n^+}(\boldsymbol{r} - \boldsymbol{p}_n^+), & \boldsymbol{r} \in T_n^+ \\ -\frac{L_n}{2A_n^-}(\boldsymbol{r} - \boldsymbol{p}_n^-), & \boldsymbol{r} \in T_n^- \\ 0, & \text{otherwise,} \end{cases} \tag{4.16}$$

where L_n is the length of the edge n, A_n^+ and A_n^- are the surface areas of the triangles and $\boldsymbol{p}_n^+$ and $\boldsymbol{p}_n^-$ are the free points of the triangles T_n^+ and T_n^- which are not on the edge n.

It can be proved [12] that the surface divergence of the RWG-functions is piecewise constant as

$$\nabla_s \cdot \boldsymbol{f}_n(\boldsymbol{r}) = \begin{cases} \frac{L_n}{A_n^+}, & \boldsymbol{r} \in T_n^+ \\ -\frac{L_n}{A_n^-}, & \boldsymbol{r} \in T_n^- \\ 0, & \text{otherwise} \end{cases} \tag{4.17}$$

The piecewise constant surface divergence means, that the equivalent surface charge densities ρ_E and ρ_H (2.29) (i.e. the normal components of the fields) have zeroth

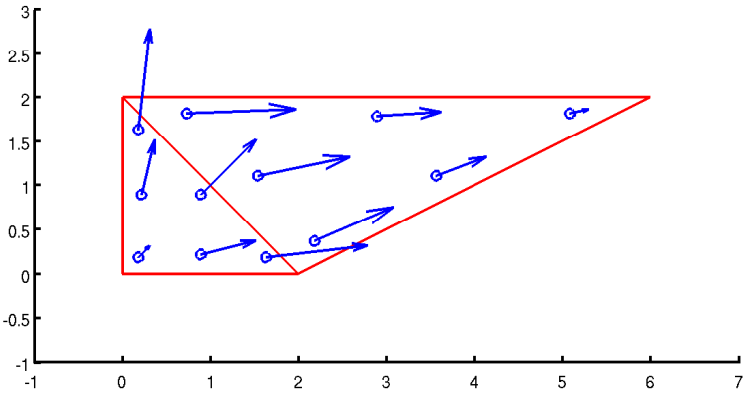

Figure 10: RWG function on a neighboring triangle pair. The RWG function is non-zero inly on these two triangles.

order approximations when RWG-functions are used as basis functions for the equivalent surface current densities $\boldsymbol{J}$ and $\boldsymbol{M}$.

The component of the RWG-functions perpendicular to the shared edge is continuous through the shared edge and constant as $\hat{\boldsymbol{m}}_n \cdot \boldsymbol{f}_n = \pm 1$. The component of the RWG function perpendicular to the other edges is zero on the edges. This results as a continuity property that is needed in order to guarantee that no equivalent net surface charge is produced by the basis functions, which is an important property of a physical solution.

The continuity of the normal component through the edges of the triangles means that the RWG-functions have a very special property

$$\int_S \nabla_s \cdot \left(u\left(\boldsymbol{r}\right) \boldsymbol{f}_n\left(\boldsymbol{r}\right)\right) \mathrm{d}S = 0 \tag{4.18}$$

with any continuous function u. This kind of basis functions are called as divergence conforming functions.

The surface curl of the RWG-functions is zero [22], i.e.

$$\hat{\boldsymbol{n}} \cdot \nabla \times \boldsymbol{f}_n\left(\boldsymbol{r}\right) = \nabla_s \times \boldsymbol{f}_n\left(\boldsymbol{r}\right) = 0. \tag{4.19}$$

This is not a general property of the divergence conforming functions, but rather a deficit of the lowest order RWG functions. The superposition of different RWG-functions can represent surface curl on a triangle, but a single RWG-function can't. Higher order divergence conforming functions [23, 24] can directly represent surface curl which can in some circumstances be an important factor driving for the use of higher order basis functions.

A deficit of RWG functions in some cases is that they can't represent a totally continuous function. This is simply because normal component through the edges of a

triangular mesh is constant. On a perfectly flat surface, the tangential fields and the equivalent surface currents are totally continuous, which the RWG functions can't represent. However, the RWG-functions still fulfil the most important continuity requirement, i.e. the conservation of charge, by the continuity of the normal component through all the edges of the triangle mesh. In this thesis the RWG functions will be used as basis functions $\boldsymbol{b}^J$ and $\boldsymbol{b}^M$ for $\boldsymbol{J}$ and $\boldsymbol{M}$.

4.3 Testing and forming of the matrix equation

Galerkin method is used in this thesis to numerically solve the equivalent surface current densities $\boldsymbol{J}$ and $\boldsymbol{M}$. This means that the set of electric testing functions is the same set of RWG functions as that used as basis for $\boldsymbol{J}$ and the set of magnetic testing functions is the same set of RWG functions as that used as basis for $\boldsymbol{M}$.

The resulting system matrix entries in (4.13) can be composed from two different testing integrals I_L and I_K.

$$I_L = \int_{S_m} \boldsymbol{t}_m(\boldsymbol{r}) \cdot \mathcal{L}(\boldsymbol{b}_n)(\boldsymbol{r}) \, \mathrm{d}S \tag{4.20}$$

$$I_K = \int_{S_m} \boldsymbol{t}_m(\boldsymbol{r}) \cdot \mathcal{K}(\boldsymbol{b}_n)(\boldsymbol{r}) \, \mathrm{d}S \tag{4.21}$$

The integral I_L related to $\mathcal{L}$ (2.17) is too singular, since the kernel of the integral operator includes the gradient of the Green's function (2.23), which is

$$\begin{aligned} \nabla G(\boldsymbol{r}, \boldsymbol{r}') &= \frac{e^{ikR}}{4\pi R^2}(ikR - 1)\frac{(\boldsymbol{r} - \boldsymbol{r}')}{R} = g(\boldsymbol{r}, \boldsymbol{r}')\frac{(\boldsymbol{r} - \boldsymbol{r}')}{R} \\ &= -\nabla' G(\boldsymbol{r}, \boldsymbol{r}'). \end{aligned} \tag{4.22}$$

The problem with the singularity arises especially when the support $S_m = T_m^+ \cup T_m^-$ of the testing function overlaps with the support $S_n = T_n^+ \cup T_n^-$ of the basis function. However, with divergence conforming testing functions the integral can be modified into

$$\begin{aligned} I_L &= \int_{S_m} \boldsymbol{t}_m(\boldsymbol{r}) \cdot \left(-\frac{1}{ik} \nabla \mathcal{S}(\nabla_s \cdot \boldsymbol{b}_n)(\boldsymbol{r}) + ik\mathcal{S}(\boldsymbol{b}_n)(\boldsymbol{r}) \right) \mathrm{d}S(\boldsymbol{r}) \\ &= \frac{1}{ik} \int_{S_m} \nabla_s \cdot \boldsymbol{t}_m(\boldsymbol{r}) \int_{S_n} G(\boldsymbol{r}, \boldsymbol{r}') \nabla_s' \cdot \boldsymbol{b}_n(\boldsymbol{r}') \, \mathrm{d}S(\boldsymbol{r}') \mathrm{d}S(\boldsymbol{r}) \\ &\quad + ik \int_{S_m} \boldsymbol{t}_m(\boldsymbol{r}) \cdot \int_{S_n} G(\boldsymbol{r}, \boldsymbol{r}') \boldsymbol{b}_n(\boldsymbol{r}') \, \mathrm{d}S(\boldsymbol{r}') \mathrm{d}S(\boldsymbol{r}), \end{aligned} \tag{4.23}$$

where $\boldsymbol{t}_m$ is either electric or magnetic RWG testing function and $\boldsymbol{b}_n$ is either electric

or magnetic RWG basis function. The gradient of the first term is moved to the testing function $\boldsymbol{t}_m$ by applying Gauss' law to a divergence formula

$$\nabla \cdot (u\boldsymbol{v}) = \nabla u \cdot \boldsymbol{v} + u\nabla \cdot \boldsymbol{v}, \tag{4.24}$$

and using the result of formula (4.18) for the divergence conforming RWG-functions and the fact that the normal component of RWG-function through the edge that it is related to is continuous.

The integral I_K related to $\mathcal{K}$ (2.18) is also too singular. However, it helps that the integral vanishes when the basis function and (tangential) testing function reside on a same planar surface. The integral can be modified by using identity $\nabla G(\boldsymbol{r}, \boldsymbol{r}') = -\nabla' G(\boldsymbol{r}, \boldsymbol{r}')$ and by dividing the gradient into normal gradient and surface gradient as $\nabla' = \frac{\partial}{\partial n'}\hat{\boldsymbol{n}}' + \nabla'_s$, when we get

$$\begin{aligned} I_K &= -\int_{S_m} \boldsymbol{t}_m(\boldsymbol{r}) \cdot \int_{S_n} \nabla' G(\boldsymbol{r}, \boldsymbol{r'}) \times \boldsymbol{b}_n(\boldsymbol{r'})\, \mathrm{d}S(\boldsymbol{r'}) \mathrm{d}S(\boldsymbol{r}) \\ &= -\int_{S_m} \boldsymbol{t}_m(\boldsymbol{r}) \cdot \int_{S_n} \frac{\partial G}{\partial n'}(\boldsymbol{r}, \boldsymbol{r'})\, \hat{\boldsymbol{n}}' \times \boldsymbol{b}_n(\boldsymbol{r'})\, \mathrm{d}S(\boldsymbol{r'}) \mathrm{d}S(\boldsymbol{r}) \\ &\quad -\int_{S_m} \boldsymbol{t}_m(\boldsymbol{r}) \cdot \int_{S_n} \nabla'_s G(\boldsymbol{r}, \boldsymbol{r'}) \times \boldsymbol{b}_n(\boldsymbol{r'})\, \mathrm{d}S(\boldsymbol{r'}) \mathrm{d}S(\boldsymbol{r}) \end{aligned} \tag{4.25}$$

Let's divide the integral I_K into two parts $I_K = I_N + I_S$. The integral I_N related to the normal derivative is integrable as is [22], i.e.

$$I_N = -\int_{S_m} \boldsymbol{t}_m(\boldsymbol{r}) \cdot \int_{S_n} \frac{\partial G}{\partial n'}(\boldsymbol{r}, \boldsymbol{r'})\, \hat{\boldsymbol{n}}' \times \boldsymbol{b}_n(\boldsymbol{r'})\, \mathrm{d}S(\boldsymbol{r'}) \mathrm{d}S(\boldsymbol{r}) \tag{4.26}$$

The integral I_S related to the surface gradient is too singular to integrate as is. By using the divergence formula (4.24) and by expressing (tangential) RWG basis function $\boldsymbol{b}_n(\boldsymbol{r}')$ on triangles T_n^+ and T_n^- with normal vectors $\hat{\boldsymbol{n}}' = \hat{\boldsymbol{n}}'_+$ and $\hat{\boldsymbol{n}}' = \hat{\boldsymbol{n}}'_-$ as $\boldsymbol{b}_n = -\hat{\boldsymbol{n}}' \times \hat{\boldsymbol{n}}' \times \boldsymbol{b}_n$, the integral I_S related to the surface gradient can be modified into

$$\begin{aligned} I_S &= -\int_{S_m} \boldsymbol{t}_m(\boldsymbol{r}) \cdot \int_{S_n} \nabla'_s G(\boldsymbol{r}, \boldsymbol{r'}) \times \boldsymbol{b}_n(\boldsymbol{r'})\, \mathrm{d}S(\boldsymbol{r'}) \mathrm{d}S(\boldsymbol{r}) \\ &= \int_{S_m} \boldsymbol{t}_m(\boldsymbol{r}) \cdot \int_{T_n^+ \cup T_n^-} \nabla'_s G(\boldsymbol{r}, \boldsymbol{r'}) \times \hat{\boldsymbol{n}}' \times \hat{\boldsymbol{n}}' \times \boldsymbol{b}_n(\boldsymbol{r'})\, \mathrm{d}S(\boldsymbol{r'}) \mathrm{d}S(\boldsymbol{r}) \end{aligned}$$

Now let's treat this integral on one of triangles T_n^+ or T_n^- at time, which means that the normal vector $\hat{\boldsymbol{n}}'$ is constant. Since $\hat{\boldsymbol{n}}' \cdot \nabla'_s \Phi = 0$ for any function Φ, on triangle T_n^+ we get

$$
\begin{aligned}
I_S &= \int_{S_m} \hat{\boldsymbol{n}}'_+ \cdot \boldsymbol{t}_m(\boldsymbol{r}) \int_{T_n^+} \nabla'_s G(\boldsymbol{r},\boldsymbol{r'}) \cdot \hat{\boldsymbol{n}}'_+ \times \boldsymbol{b}_n(\boldsymbol{r'})\, \mathrm{d}S(\boldsymbol{r'}) \mathrm{d}S(\boldsymbol{r}) \\
&= \int_{S_m} \hat{\boldsymbol{n}}'_+ \cdot \boldsymbol{t}_m(\boldsymbol{r}) \int_{T_n^+} \nabla'_s \cdot \left(G(\boldsymbol{r},\boldsymbol{r'})\, \hat{\boldsymbol{n}}'_+ \times \boldsymbol{b}_n(\boldsymbol{r'}) \right) \mathrm{d}S(\boldsymbol{r'}) \mathrm{d}S(\boldsymbol{r}) \\
&\quad - \int_{S_m} \hat{\boldsymbol{n}}'_+ \cdot \boldsymbol{t}_m(\boldsymbol{r}) \int_{T_n^+} G(\boldsymbol{r},\boldsymbol{r'})\, \nabla'_s \cdot \hat{\boldsymbol{n}}'_+ \times \boldsymbol{b}_n(\boldsymbol{r'})\, \mathrm{d}S(\boldsymbol{r'}) \mathrm{d}S(\boldsymbol{r}) \\
&= \int_{S_m} \hat{\boldsymbol{n}}'_+ \cdot \boldsymbol{t}_m(\boldsymbol{r}) \int_{\partial T_n^+} G(\boldsymbol{r},\boldsymbol{r'})\, \hat{\boldsymbol{m}}'_+ \cdot \hat{\boldsymbol{n}}'_+ \times \boldsymbol{b}_n(\boldsymbol{r'})\, \mathrm{d}l(\boldsymbol{r'}) \mathrm{d}S(\boldsymbol{r}) \\
&= \int_{\partial T_n^+} \left(\hat{\boldsymbol{m}}'_+ \cdot \hat{\boldsymbol{n}}'_+ \times \boldsymbol{b}_n(\boldsymbol{r'}) \right) \hat{\boldsymbol{n}}'_+ \cdot \int_{S_m} G(\boldsymbol{r},\boldsymbol{r'})\, \boldsymbol{t}_m(\boldsymbol{r})\, \mathrm{d}S(\boldsymbol{r})\, \mathrm{d}l(\boldsymbol{r'}). \quad (4.27)
\end{aligned}
$$

Similar can also be done for the other traingle T_n^-. General divergence formula (4.24) was used at the first stage. Then the Gauss' divergence formula on surface was used to get the boundary line integral, where $\hat{\boldsymbol{m}}'_+$ are the edge outer unit normal vectors of the three edges of T_n^+ and ∂T_n^+ is the union of the three edges. Finally the order of integration is changed in order to make this double integral integrable [22]. Since the surface curl of the lowest order divergence conforming RWG functions is zero (4.19), the term containing $\nabla'_s \cdot \hat{\boldsymbol{n}}' \times \boldsymbol{b}_n$ is also zero by (2.28).

The matrix entries are calculated by numerically integrating the presented integrals I_L, I_N and I_S by using standard Gaussian quadrature for the triangles [25, 26]. The Gaussian quadrature can accurately integrate a function that can be well approximated as a polynomial. Such is not the case for the Green's function when the support of the testing function and the support of the basis functions are close to each other, i.e. when $|\boldsymbol{r} - \boldsymbol{r}'|$ is relatively small. In such cases, a semi-analytic integration is used by representing the exponential of the Green's function in terms of Maclaurin series [27] and integrating some of the singular lowest order terms of the inner integral analytically [28, 29, 30]. The way how this is implemented closely resembles [31]. The remaining non-singular part of the Green's function, i.e. the part with higher order terms, poses no problem for the Gaussian quadrature and can be accurately integrated numerically.

5 Antenna theory

This chapter includes a short review of the electromagnetic theory behind antennas. The way how antennas can be numerically simulated with the surface integral equation method is treated in Chapter 6.

The analysis of the characteristics of the antennas is based on the Maxwell's equations, especially the curl equations (2.1) and (2.3). Antenna problems are characterized by the specific feed of the antenna, such as an open end of a coaxial cable, and the boundary conditions that the antenna structure imposes for the total fields.

It would be very hard to directly find the solution for the boundary value problem that satisfies both the Maxwell's equations and the boundary conditions. A much simpler way to analyze antennas is to use the equivalence principle and replace the antenna structure with equivalent sources that lie in free space. The dielectric domains can be replaced by the relative polarization currents as clarified in Chapter 2.3.1. The metallic domains are replaced by equivalent electric surface current density on the boundary surfaces of the metal. The difficult boundary value problem is then transformed into an integral equation problem, which can be solved numerically using method of moments as clarified in Chapter 4.

5.1 Connection between two antennas as two-port

Antennas are the most crucial part of typical radio systems. Antennas are used as the interface between the surrounding space and an electric circuit. The use of antennas in the communication technology most often leads to a problem of defining the amount of transferred power between a transmitting electric circuit and a receiving electric circuit, where antennas are used at the both ends as tools to transfer power between the electromagnetic field in the surrounding space and the field of the transmission line that connects the electric circuit and the antenna together. The connection of the two electric circuits through the radio channel can be described as a linear and reciprocal two-port which can be characterized by a Z-matrix, which is symmetric in the reciprocal case ($Z_{12} = Z_{21}$). A T-circuit model can be constructed for the reciprocal two-port [32].

The impedance parameters can be determined as follows. The antenna impedances Z_{11} and Z_{22} are the impedances, which a feeding transmission line would see as the load if the antennas are connected to the lines in free space. The impedances can be defined by measuring the reflection coefficient ρ in free space, which practically means measurements inside a reflection free chamber. The connection between the reflection coefficient and input impedance is further studied in Chapter 6.1.3. The impedance parameter Z_{21} describes the coupling of the antennas and it can be defined by holding the terminals of the receiving antenna open ($Z_{0r} = \infty$), when we

get

$$Z_{21} = \frac{U_2}{I_1}. \tag{5.1}$$

The determination of Z_{21} requires accurate simulations, if the antennas are relatively near to each other. But when the antennas are far enough away from each other, the impedance parameter Z_{21} is very small and the presence of the receiving antenna basically doesn't alter the characteristics of the transmitting antenna, i.e. the equivalent surface current densities $\boldsymbol{J}$ and $\boldsymbol{M}$. This also means that the impedances seen from the connection terminals of the antennas are $Z_1 \approx Z_{11}$ and $Z_2 \approx Z_{22}$. In this case the amount of received power can simply be determined by solving the antenna impedances Z_{11} and Z_{22} with accurate simulations and by determining the impedance parameter Z_{21} analytically.

The antennas at both ends are connected to transmission lines. The antenna impedances $Z_1 \approx Z_{11}$ and $Z_2 \approx Z_{22}$ are in general non-matched to the characteristic impedances Z_{0t} and Z_{0r} of the transmission lines. This drops the amount of power transferred from the transmitting electric circuit to the receiving electric circuit.

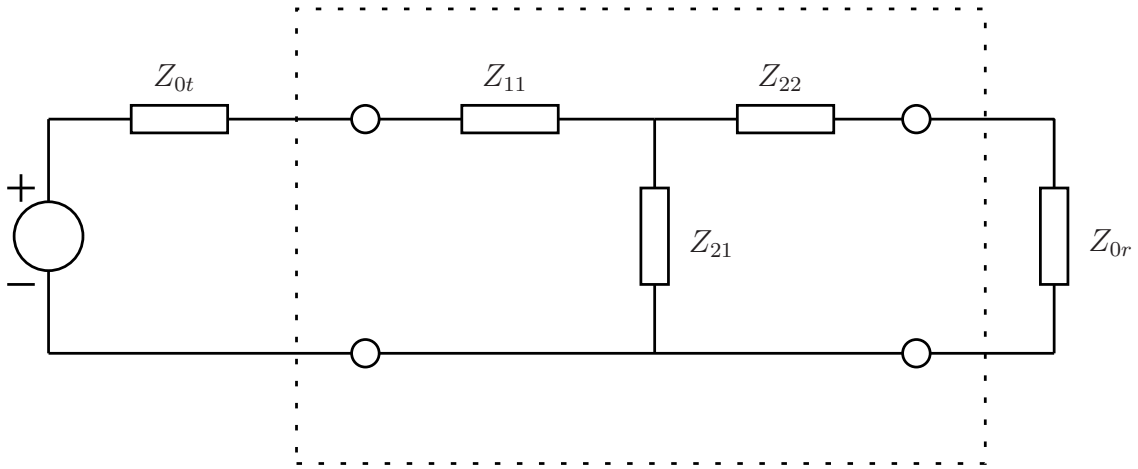

Figure 11: Two port model which describes the connection between a transmitting antenna and a receiving antenna. The transmitting antenna and the receiving antenna are connected to transmission lines with characteristic impedances Z_{0t} and Z_{0t}. The antenna impedance Z_{11} of the transmitting antenna and the antenna impedance Z_{22} of the receiving antenna determine the impedance matching at the ends in free space. The impedance parameter Z_{21} determines the coupling between the two antennas and it's very small when the distance between the two antennas is large.

5.2 Antenna fields

If the equivalent surface current densities $\boldsymbol{J}$ and $\boldsymbol{M}$ of the transmitting antenna problem have been solved, the field created by the equivalent surface currents can simply be determined by using representation formulas (2.14) and (2.15). This would result as an accurate representation of the fields anywhere out of the antenna structure.

Electromagnetic field around the transmitting antenna can roughly be divided into three different regions [32]

- The reactive nearfield region
- The radiating nearfield region (Fresnel region)
- The radiating farfield region (Fraunhofer region)

The properties of the fields in these regions differ significantly from each other.

In the radiating farfield, which is the region furthest away from the antenna, the fields $\boldsymbol{E}_1$ and $\boldsymbol{H}_1$ of the transmitting antenna can in any direction be locally approximated as a TEM wave. In a spherical coordinate system that's centered at the location of the transmitting antenna, the resulting sperical TEM wave then satisfies the equations [32]

$$\boldsymbol{E}_1(\boldsymbol{r}) = \left(-i\omega\mu\hat{\boldsymbol{u}}_r \times \hat{\boldsymbol{u}}_r \times \boldsymbol{N}(\theta,\phi) - ik\hat{\boldsymbol{u}}_r \times \boldsymbol{N}_m(\theta,\phi)\right)\frac{e^{ikr}}{4\pi r} \tag{5.2}$$

$$\boldsymbol{H}_1(\boldsymbol{r}) = \left(-i\omega\epsilon\hat{\boldsymbol{u}}_r \times \hat{\boldsymbol{u}}_r \times \boldsymbol{N}_m(\theta,\phi) + ik\hat{\boldsymbol{u}}_r \times \boldsymbol{N}(\theta,\phi)\right)\frac{e^{ikr}}{4\pi r}, \tag{5.3}$$

where the electric radiation vector $\boldsymbol{N}$ and the magnetic radiation vector $\boldsymbol{N}_m$ are

$$\boldsymbol{N}(\theta,\phi) = \int_{\partial D_0} e^{-ik\hat{\boldsymbol{u}}_r\cdot\boldsymbol{r}'}\boldsymbol{J}(\boldsymbol{r}')\,\mathrm{d}S' \tag{5.4}$$

$$\boldsymbol{N}_m(\theta,\phi) = \int_{\partial D_0} e^{-ik\hat{\boldsymbol{u}}_r\cdot\boldsymbol{r}'}\boldsymbol{M}(\boldsymbol{r}')\,\mathrm{d}S'. \tag{5.5}$$

The integration here is done over ∂D_0, i.e. the boundary surface of the surrounding free space D_0, which in practice is the outmost surface of an antenna structure. These field repreentations are approximations of the exact representation formulas (2.14) and (2.15) and are found by replacing the gradient of the Green's function (4.22) with $\nabla G(\boldsymbol{r},\boldsymbol{r}') \approx ikG(\boldsymbol{r},\boldsymbol{r}')\hat{\boldsymbol{u}}_r$ and by an approximation in the denominator of the Green's function (2.23) with $|\boldsymbol{r}-\boldsymbol{r}'| \approx r$ and in the numerator with $|\boldsymbol{r}-\boldsymbol{r}'| \approx r - \hat{\boldsymbol{u}}_r\cdot\boldsymbol{r}'$.

It's clearly seen that the phase of the radiating field changes radially as that of a plane wave propagating in direction $\hat{\boldsymbol{u}}_r$, i.e. away from the origin. The amplitude

decays as $1/r$. Also the dependence of the fields on the direction is separated from the radial dependence. The connection between the electric field $\boldsymbol{E}_1$ and the magnetic field $\boldsymbol{H}_1$ in farfield and vacuum with $\epsilon = \epsilon_0$ and $\mu = \mu_0$ is

$$\boldsymbol{E}_1(\boldsymbol{r}) = -\eta_0 \hat{\boldsymbol{u}}_r \times \boldsymbol{H}_1(\boldsymbol{r}) \tag{5.6}$$

$$\boldsymbol{H}_1(\boldsymbol{r}) = \frac{1}{\eta_0} \hat{\boldsymbol{u}}_r \times \boldsymbol{E}_1(\boldsymbol{r}), \tag{5.7}$$

i.e. the fields $\boldsymbol{E}_1$ and $\boldsymbol{H}_1$ of the antenna are purely transverse compared to the direction of propagation $\hat{\boldsymbol{u}}_r$ of the spherical wave with $\hat{\boldsymbol{u}}_r \cdot \boldsymbol{E}_1 = 0$ and $\hat{\boldsymbol{u}}_r \cdot \boldsymbol{H}_1 = 0$. Wave impedance η of this TEM wave is equal to the plane wave impedance $\eta_0 = \sqrt{\mu_0/\epsilon_0}$ of the media in all the directions, which means that the field can very well be locally approximated in any direction by a plane wave travelling away from the origin.

In the farfield, the distribution of the fields $\boldsymbol{E}_1$ and $\boldsymbol{H}_1$ to different directions at a constant large enough distance $r = r_0$ from the origin, i.e. the normalized radiation pattern

$$F(\theta, \phi) = \frac{|\boldsymbol{E}_1(r_0, \theta, \phi)|}{|\boldsymbol{E}_1(r_0, \theta, \phi)|_{max}} \tag{5.8}$$

is constant as a function of distance and is equal for both of the fields.

The intensity of the radiation, i.e. the power flux per unit area is given by the complex Poynting vector

$$\boldsymbol{S}_1 = \frac{1}{2} \boldsymbol{E}_1 \times \boldsymbol{H}_1^* = \frac{1}{2} \eta_0 |\boldsymbol{H}_1|^2 \hat{\boldsymbol{u}}_r = \frac{1}{2\eta_0} |\boldsymbol{E}_1|^2 \hat{\boldsymbol{u}}_r, \tag{5.9}$$

which is purely resistive in the farfield, because the fields are associated to each other by the resistive plane wave impedance η_0 of the media.

In the radiating nearfield, the complex Poynting vector (5.9) still has the dominant outgoing radiating part $(\hat{\boldsymbol{u}}_r \cdot \boldsymbol{S}_1)\hat{\boldsymbol{u}}_r$, but the wave impedance is generally not constant anymore. The wave impedance is a function of both the distance r and the direction (θ, ϕ), i.e. the distance alters the wave impedance. The wave impedance gets more and more dominated by the antenna rather than the surrounding media when going nearer to the antenna.

In the reactive nearfield, the complex Poynting vector (5.9) can basically have any components and the outgoing part isn't dominant anymore. The power flux can both pulsate to and from the antenna and also circulate around the antenna. All in all, the time average of the net power flow away from the antenna remains the same as in the regions further away, but the pulsating power flux causes the stored energy to be even higher than the radiation in the nearfield. The stored energy can be both capacitive and inductive as in electric circuits.

Complex antenna power S_{a1} is related to the antenna input impedance Z_{11} and the input current I in free space by [32]

$$S_{a1} = P_{rad} + P_{loss} - i2\omega \left(W_m - W_e\right) = \frac{1}{2} Z_{11} \left|I\right|^2, \tag{5.10}$$

where P_{rad} is the radiated resistive power, P_{loss} is the resistive power loss in the antenna structures and W_m and W_e are the stored magnetic energy and the stored electric energy of the antenna nearfield. This relation is identical to a similar relation of a RLC circuit consisting of resistors, inductors and capacitors.

5.3 Directivity and gain

From the total radiated power P_{rad} and the distribution of the radiated power (5.9) to different directions in the farfield, the directivity pattern of the antenna is defined as [32]

$$D\left(\theta, \phi\right) = \frac{4\pi r^2 \left|\boldsymbol{S}\left(\boldsymbol{r}\right)\right|^2}{P_{rad}} = \frac{4\pi r^2 \left|\boldsymbol{E}\left(\boldsymbol{r}\right)\right|^2}{\oint \left|\boldsymbol{E}\left(\boldsymbol{r}\right)\right|^2 \mathrm{d}S}, \tag{5.11}$$

where the field is evaluated on a surface of a sphere with radius r that's large enough compared to the dimensions of the antenna. Directivity is often given only as a single figure, which means the maximum directivity. Directivity can be given in logarithmic scale in dBi units, which means directivity in decibels compared to a hypothetical isotropic radiator, which would radiate evenly to all directions with constant directivity $D = 1$.

In order to be of good use in communications, an antenna needs to radiate a field with a given polarization. Polarization is defined as the orientation of the oscillation of the radiated electric field and can be of linear, circular or elliptical type. When a receiver knows the polarization of the field of a transmitting antenna, the receiving antenna can be engineered to optimally receive only that polarization. Since any vector on a surface can be divided into two orthogonal components, the polarization of the radiated field can also be divided into two orthogonal components. The polarization that the antenna is designed for is the co-polarization, and the polarization orthogonal to the co-polarization is the cross polarization. Directivity pattern (5.11) can be defined for both the co-polarization and the cross polarization of the antenna. For antennas with either vertical or horizontal co-polarization, the directivity patterns of the co-polarization and the cross polarization are simply the directivities of the θ- and ϕ-components of the electric field $\boldsymbol{E}$ on the spherical surface far away,

i.e.

$$\begin{aligned} D_\theta(\theta,\phi) &= \frac{4\pi r^2 \left|\hat{\boldsymbol{u}}_\theta \cdot \boldsymbol{E}(\boldsymbol{r})\right|^2}{\oint \left|\boldsymbol{E}(\boldsymbol{r})\right|^2 \mathrm{d}S} \\ D_\phi(\theta,\phi) &= \frac{4\pi r^2 \left|\hat{\boldsymbol{u}}_\phi \cdot \boldsymbol{E}(\boldsymbol{r})\right|^2}{\oint \left|\boldsymbol{E}(\boldsymbol{r})\right|^2 \mathrm{d}S}. \end{aligned} \tag{5.12}$$

Often the directivity patterns of antennas are given in terms of the directivities of $\hat{\boldsymbol{u}}_\theta$- and $\hat{\boldsymbol{u}}_\phi$-polarizations even if neither of them matches to the co-polarization of the antenna, so a similar practice will also be used in this thesis.

If the input power P_{in} of the antenna is known, the gain of the antenna in terms of the distribution of the radiated power (5.9) is defined as

$$G(\theta,\phi) = \frac{4\pi r^2 \left|\boldsymbol{S}(\boldsymbol{r})\right|^2}{P_{in}}, \tag{5.13}$$

where again the field is evaluated on a surface of a sphere with radius r large enough. Antenna radiation efficiency is often defined as

$$\eta_{rad} = \frac{P_{rad}}{P_{in}}, \tag{5.14}$$

so the gain in terms of the directivity (5.11) is simply

$$G = \eta_{rad} D. \tag{5.15}$$

Gain is always smaller than the directivity D because of the losses of the antenna structure. Gain can also be defined by replacing the input power P_{in} with the incident available power P_i at the antenna input. In this case the drop in the transmitted power caused by the impedance mismatch at the antenna input is also included in the losses, which reduces the antenna efficiency.

5.4 Lorentz reciprocity theorem

Lorentz reciprocity theorem can link two sets of solutions of Maxwell's equations (2.1)-(2.4) together in a specific way. Let these sets be $\boldsymbol{E}_1$, $\boldsymbol{H}_1$, $\boldsymbol{J}_1$ and $\boldsymbol{E}_2$, $\boldsymbol{H}_2$, $\boldsymbol{J}_2$. A vector quantity $\nabla \cdot (\boldsymbol{E}_1 \times \boldsymbol{H}_2 - \boldsymbol{E}_2 \times \boldsymbol{H}_1)$ can be rewritten as

$$\nabla \times \boldsymbol{E}_1 \cdot \boldsymbol{H}_2 - \boldsymbol{E}_1 \cdot \nabla \times \boldsymbol{H}_2 - \nabla \times \boldsymbol{E}_2 \cdot \boldsymbol{H}_1 + \boldsymbol{E}_2 \cdot \nabla \times \boldsymbol{H}_1.$$

If the Maxwell's curl equations are used, integration over a volume V is applied and

the Gauss' divergence theorem is used we get [32]

$$\oint_S \hat{\boldsymbol{n}} \cdot (\boldsymbol{E}_1 \times \boldsymbol{H}_2 - \boldsymbol{E}_2 \times \boldsymbol{H}_1)\,\mathrm{d}S = \int_V (\boldsymbol{J}_1 \cdot \boldsymbol{E}_2 - \boldsymbol{J}_2 \cdot \boldsymbol{E}_1)\,\mathrm{d}V, \tag{5.16}$$

which is the Lorentz reciprocity theorem. The surface integral is actually cancelled out, if the sources $\boldsymbol{J}_1$ and $\boldsymbol{J}_2$ are assumed to be of finite size and the integration is applied over the whole space. This is simply because in the farfield region of any finite sources the field is spherical TEM wave satisfying (5.7), which then implies $\boldsymbol{E}_1 \times \boldsymbol{H}_2 = \boldsymbol{E}_1 \cdot \boldsymbol{E}_2/\eta_0$ and $\boldsymbol{E}_2 \times \boldsymbol{H}_1 = \boldsymbol{E}_2 \cdot \boldsymbol{E}_1/\eta_0$. These terms cancel each other out in (5.16), which gives

$$\int_V (\boldsymbol{J}_1 \cdot \boldsymbol{E}_2)\,\mathrm{d}V = \int_V (\boldsymbol{J}_2 \cdot \boldsymbol{E}_1)\,\mathrm{d}V, \tag{5.17}$$

which is often referred to as Rayleigh-Carson reciprocity theorem [33]. If the (equivalent) magnetic current $\boldsymbol{J}_m$ similar to the magnetic polarization current in (2.36) is added into the Maxwell's equations, the reciprocity theorem further gives

$$\int_V (\boldsymbol{J}_1 \cdot \boldsymbol{E}_2 - \boldsymbol{J}_{m1} \cdot \boldsymbol{H}_2)\,\mathrm{d}V = \int_V (\boldsymbol{J}_2 \cdot \boldsymbol{E}_1 - \boldsymbol{J}_{m1} \cdot \boldsymbol{H}_1)\,\mathrm{d}V. \tag{5.18}$$

The reciprocity theorem can be used to see, that the receiving properties of antennas are closely connected to the transmitting properties [32, 33], i.e. in most cases it suffices to only analyze the transmitting properties of antennas. This is the case when the coupling between the transmitting antenna and the receiving antenna is minimal, i.e. when the two are far away from each other and the impedance parameter Z_{21} (5.1) is small. However, when the two antennas are close to each other, the problem is a lot more challenging and needs solution of the Maxwell's equation e.g. with the surface integral equation method. In this thesis the case where two antennas are close to each other is not treated, so the antennas are only simulated as transmitting antennas.

6 Simulation of antennas

The surface integral equation method based on EFIE-PMCHWT formulation as described in Chapter 4 can be used to calculate the characteristics of transmitting antennas. Antenna problems are very close in nature to basic scattering problems. What is needed to simulate a transmitting antenna is the construction of the triangle mesh for the antenna geometry, the definition of the incident field that excites the characteristic current distribution of the antenna, the calculation of the MoM system matrix elements (4.14), solving of the equivalent surface current distribution of the antenna by solving the MoM matrix equation (4.13), and calculation of all the wanted antenna parameters from the results. In this chapter the specific procedures that are needed in the calculation of antenna properties with the method are treated.

6.1 Antenna feed

In order to calculate the field of a transmitting antenna, the characteristic current distribution of the antenna has to be excited somehow. The feed can either be a distributed excitation resembling a real feed or it can be approximated by a highly localized feed.

The excitation of the antenna in real life comes most often from a TEM waveguide. The TEM feed can be modelled either by including the waveguide to the model or by assuming that the field were in the known TEM mode on the antenna-waveguide interface aperture. The latter isn't exactly true, which is well seen for a coaxial cable in [13]. However, this frill approximation is still used very often to simplify the feeding of antennas.

6.1.1 Localized delta-gap feed

Feed area of an antenna can be very localized in certain situations. One example of this is a small gap between two metallic bodies, where a voltage is forced between the objects as in Figure 12.

If the gap length d is small, a quasi-static approximation can be used by assuming that the incident electric field $\boldsymbol{E}^p$ is other than zero only in the gap with constant field strength $E = V/d$. If the distance between the metal bodies is pushed in limit to zero and voltage is kept as constant, the incident electric field tends to delta-function on the interface between the metal bodies. This effectively connects the two metal bodies together. If the gap coincides with an edge of the triangular mesh, the delta function causes for the electric part of the excitation vector b in matrix equation (4.13) an excitation vector coefficient

$$b_{i(m)} = V l_m \tag{6.1}$$

where V is the voltage of the gap, l_m is the length of the edge m related to the gap

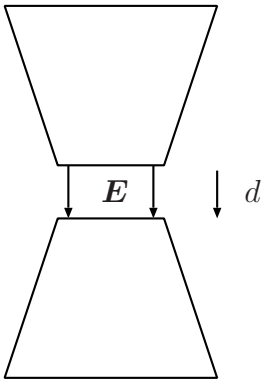

Figure 12: A small voltage gap.

and $i(m)$ is the matrix index number of the electric testing function for the edge m of the triangular mesh. If the gap is extended on more than one edge, the excitation vector b has more than one non-zero coefficients.

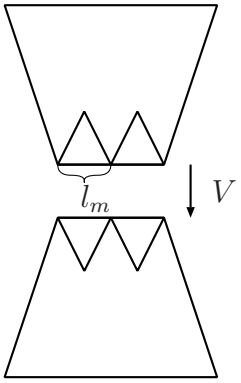

Figure 13: Delta-gap excitation.

Delta-gap is actually an accurate and realistic feed for small wire antennas such as simple dipole antennas. However, the use of delta-gap in situations when the aperture of the feed is larger in size is questionable, since the infinitesimally small approximation for the aperture shouldn't be relevant any more.

6.1.2 Coaxial frill

Maybe one of the most used methods in practice to feed an antenna is the use of a coaxial probe, i.e. an open end of a coaxial cable with a lenghtened inner conductor and possibly the inner and outer conductors connected somewhere in the antenna geometry. If it is assumed, that only TEM mode exists at the opening aperture of the coaxial line, the fields are tangential to the opening aperture.

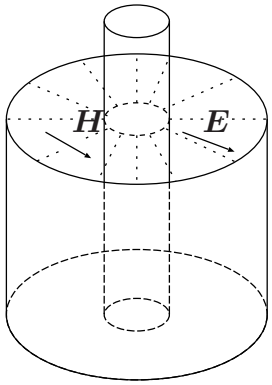

Figure 14: Coaxial probe.

The fields of the idealized coaxial aperture are aaaumed to be equal to the characteristic TEM coaxial fields $\boldsymbol{E}^{coax}$ and $\boldsymbol{H}^{coax}$. The transverse fields of the coaxial frill thendefine the equivalent surface currents of the frill as

$$\begin{aligned} \boldsymbol{J}^{coax} &= \hat{\boldsymbol{n}} \times \boldsymbol{H}^{coax} \\ \boldsymbol{M}^{coax} &= -\hat{\boldsymbol{n}} \times \boldsymbol{E}^{coax} \end{aligned}, \tag{6.2}$$

which are the sources of the incident field of the antenna.

If the coaxial frill is in the same plane with a ground plane that is much larger than the size of the frill, an approximation can be made. By assuming that the size of the ground plane is infinite, the frill itself can be replaced with metal and equivalent magnetic current [13]

$$\boldsymbol{M}^{coax}(\boldsymbol{r}) = -2\hat{\boldsymbol{n}} \times \boldsymbol{E}^{coax} = \frac{-2V_0}{log\,(b/a)\,r}, \tag{6.3}$$

The magnetic current is doubled because the image source of $\boldsymbol{M}(\boldsymbol{r})$ on an infinite PEC plane is $\boldsymbol{M}(\boldsymbol{r})$, i.e. equal to the source itself. The electric current $\boldsymbol{J}^{coax}$ on the other hand is removed because the image source of $\boldsymbol{J}(\boldsymbol{r})$ is $-\boldsymbol{J}(\boldsymbol{r})$, i.e. the image source cancels the source.

However, as is well seen in [13], the field on the coaxial aperture is not in the characteristic coaxial mode at the opening aperture in general. If the most accurate results are desired, the actual feeding structure should also be included in the model itself. The frill approximation and the assumption of image source of an infinite ground plane will not be used in this work, but a more sophisticated model will instead be used to implement the coaxial feed.

6.1.3 Accurate modelling of the coaxial feed

Let's consider a case where the antenna is connected to an infinitely long coaxial cable. The coaxial line is assumed to be oriented along z-axis and the antenna-cable

interface is at $z = 0$. The TEM voltage wave inside the cable has both the forward tarvelling wave and the backward travelling wave as

$$V(z) = V_+ e^{i\beta z} + V_- e^{-i\beta z}, \tag{6.4}$$

where V_+ is the voltage of the forward going wave and V_- is the voltage of the backward going wave. The backward going wave is caused by the impedance mismatch at the antenna-cable interface, where the reflection coefficient $\rho = V_-/V_+$ of the TEM-mode is

$$\rho_a = \frac{Z_a - Z_0}{Z_a + Z_0}. \tag{6.5}$$

Here Z_a is the antenna input impedance and Z_0 is the characteristic impedance of the coaxial cable. Antenna impedance is a circuit parameter itself and is more treated in Chapter 5.

The reflection often excites some other higher order modes of the coaxial cable. If the frequency is well below the cutoff frequencies of the higher order modes they should vanish quickly inside the cable, and only TEM mode is expected to exist well inside the cable. Since the coaxial cable is assumed infinitely long, no further reflections should exist.

One way to accurately model the physical behavior of the coaxial feed with antennas is to extend the coaxial cable for a long enough distance and use some localized excitation inside the cable far enough away from the antenna interface of the cable. If the cable extension is long enough and the frequency is low enough, all the higher order modes that can be excited by the localized excitation inside the cable should be well attenuated before the antenna interface, which is desired.

Let's assume that the incident TEM wave is $V_0 e^{i\beta z}$. The antenna interface then causes a reflection which again excites the TEM mode and some higher order evanescent waves. Since the antenna interface is assumed to be at $z = 0$, the reflected TEM wave is $V_0 \rho_a e^{-i\beta z}$, where the reflection coefficient ρ_a is the reflection coefficient of the cable antenna interface (6.5). The desired result now would be that the reflected TEM wave never causes another reflection.

Let's consider a case with the coaxial cable extension of length l_c that is short circuited at the other end and connected to the antenna at the other end. The incident wave and the first reflected wave are as clarified earlier. However, in this case the first reflected wave travels to the short circuited end at $z = -l_c$, which then causes a reflected wave $V_0 \rho_a e^{i\beta l_c} \rho_0 e^{i\beta(z+l_c)}$, where the reflection coefficient of the short circuited cable end is $\rho_0 = -1$. As a total, infinite number of reflections occur, and the amplitudes V_+ and V_- of the forward and backward going waves are

$$\begin{aligned} V_+ &= V_0 \left(1 - \rho_a e^{i2\beta l_c} + \rho_a^2 e^{i4\beta l_c} - \dots\right) \\ V_- &= V_0 \left(\rho_a - \rho_a^2 e^{i2\beta l_c} + \rho_a^3 e^{i4\beta l_c} - \dots\right). \end{aligned} \tag{6.6}$$

These can be represented as sums of a general geometric series $\sum_{n=0}^{\infty} q^n = \frac{1}{1-q}$ for $|q| < 1$, so we get

$$V_+ = \frac{V_0}{1 + \rho_a e^{i2\beta l_c}} \tag{6.7}$$

$$V_- = \frac{V_0 \rho_a}{1 + \rho_a e^{i2\beta l_c}}. \tag{6.8}$$

The reflection coefficient is then $V_-/V_+ = \rho_a$, as is expected and desired.

The only artifact of this kind of a feed is that the impedance Z_b seen from the antenna-cable interface into the cable isn't matched to Z_0, but instead is equal to the impedance of a short circuited transmission line as

$$Z_b = -iZ_0 \tan(\beta l_c). \tag{6.9}$$

This can cause problems especially in the two special cases, when for any integer n the length of the cable extension is $l_c = n\lambda/2$ or $l_c = \lambda/4 + n\lambda/2$, which result as $Z_b = 0$ or $Z_b = \pm i\infty$. In these cases no TEM field should basically be able to enter the cable from outside, which is false, since the impedance as seen from the antenna-cable interface should be matched to the characteristic impedance Z_0 of the cable.

However, excluding the two cases when the impedance tends to zero or infinity, the short circuited coaxial cable extension should be closer to a real feed than the idealized frill model, and is used in this work to feed antennas with a coaxial cable feed.

6.2 Directivity pattern

As clarified in Chapter 5, most of the antenna parameters can be defined by the radiating farfield of the transmitting antenna. Computation of directivity patterns $D_\theta(\theta, \phi)$ and $D_\phi(\theta, \phi)$ is straightforward after the equivalent surface current densities $\boldsymbol{J}$ and $\boldsymbol{M}$ have been solved. What is only needed is the construction of a points $\boldsymbol{p}_F^i$ and integration weights w_F^i for numerical integration of the antenna farfield on a surface of a sphere far enough away and computation of the antenna electric field $\boldsymbol{E}$ in points $\boldsymbol{p}_F$ with the farfield representation formula (5.2) and use of (5.12) to compute the directivity patterns. Directivity of an antenna is often given as a single number. In such cases directivity means the maximum D_{max} of the directivity pattern (5.11), and is often given in logaritmic scale in units dBi as

$$D_{max} = 10 \log_{10}(\max(D(\theta, \phi))) \text{ dBi}, \tag{6.10}$$

which means maximum directivity in dB compared to an imaginary isotropic radiator, that has constant directivity pattern $D(\theta, \phi) = 1$.

6.3 Antenna impedance

The calculation of antenna impedance Z_{11} (Chapter 5.1) is a complicated task which has also created some opposing views in the past [35, 36]. It's important to understand that the antenna impedance $Z_a = Z_{11}$ is basically a circuit level parameter, i.e. it is used to define the reflection coefficient at the antenna-feed interface as

$$\rho = \frac{Z_a - Z_0}{Z_a + Z_0}, \tag{6.11}$$

where Z_0 is the characteristic impedance of the waveguide feeding the antenna. The definition of the characteristic impedance is unique for TEM waveguides such as coaxial cable, but TE- or TM-waveguides don't have one unique definition of characteristic impedance since the definition of voltage and current is non-unique. This means that the definition of the antenna impedance is also non-unique in such cases, even if the surface currents and the resulting electromagnetic field of the antenna are solved. This means that the only generalizable definition of the antenna impedance is achieved by first defining the voltage and current of the feeding waveguide, which give the characteristic impedance and then somehow defining the reflection coeffient $\rho = V_-/V_+$ in terms of the amplitudes V_+ and V_- of forward and backward travelling waves of the feeding waveguide. In this thesis, the antenna impedance calculations are limited to the TEM waveguide feeds, so the non-uniqueness of the antenna impedance is avoided, since the definition of the current and voltage are unique.

Let's assume that the antenna feed is a localized delta-gap as described in Chapter 6.1.1. The voltage of the delta-gap is unique and equal to the forced incident voltage of the feed. The current can be calculated by integrating the equivalent surface current density $\boldsymbol{J}$ over the edges of the feed. For localized ports with a forced localized incident electric field $\boldsymbol{E}^p$, the antenna impedance, which by the input voltage U_{in} and input current I_{in} is defined as $Z_{a,l} = U_{in}/I_{in}$, can generally be calculated by

$$Z_{a,l} = \frac{U_{in}}{I_{in}} = \frac{U_{in}I_{in}}{I_{in}^2} = \frac{1}{I_{in}^2}\int \boldsymbol{E}^p \cdot \boldsymbol{J}\mathrm{d}S = \frac{1}{I_{in}^2}\int (\boldsymbol{E} - \boldsymbol{E}^s) \cdot \boldsymbol{J}\mathrm{d}S, \tag{6.12}$$

where the secondary electric field $\boldsymbol{E}^s$ is calculated by using the representation formula (2.14). On a metallic PEC surface the total tangential electric field $\boldsymbol{E}_{tan}$ vanishes which further gives

$$Z_{a,l}^{PEC} = -\frac{1}{I_{in}^2}\int \boldsymbol{E}^s \cdot \boldsymbol{J}\mathrm{d}S. \tag{6.13}$$

In the case of the accurate coaxial cable model (Chapter 6.1.3), the calculation of the antenna impedance Z_a is logical in physical sense, but in practice more complicated. With the definition of the reflection coefficient as $\rho = V_-/V_+$, the determination of the antenna impedance is transformed into determination of coefficients V_+ and V_-, i.e. the amplitudes of the forward and backward travelling TEM voltage waves inside

the cable. After the reflection coefficient ρ is calculated, the antenna impedance by equation (6.11) can simply be calculated as

$$Z_a = Z_0 \frac{1+\rho}{1-\rho}. \tag{6.14}$$

The reflection coefficient can also be defined from the respective current coefficients $I_+ = V_+/Z_0$ and $I_- = V_-/Z_0$. By the direction dependent summation of currents, the only difference is the addition of a minus sign as the reflection coefficient is $\rho = -I_-/I_+$.

The current of a coaxial cable that's oriented along the z-axis is simply the line integral of the $\hat{\boldsymbol{u}}_z \cdot \boldsymbol{J}$ around the inner conductor surface at a plane where z is constant. Since the normal component of the RWG-functions (4.16) is one on the edge that the RWG function belongs to, the total current is simply

$$I_{tot}(z) = \sum_{i=1}^{N^z} l_i^z \cdot J_i^z, \tag{6.15}$$

where l_i^z is the length of the i:th edge around the wire at z and J_i^z is the RWG coefficient of the basis function of $\boldsymbol{J}$ at the same edge. The edges of these RWG-functions are assumed to lie on a plane of constant z.

After the total current I_{tot} is defined at different positions $z = z_i$ along the coaxial cable, the next problem is to define the coefficients I_+ and I_- from the total current waveform $I_{tot}(z)$. The coefficients can be determined by using the matrix pencil method [34] to find an exponential function fit

$$I_{tot}(z) = \sum_j A_j e^{b_j z} \tag{6.16}$$

for the waveform. The values of b_j can at this stage be used as an accuracy test for the current solution, since the coefficients b_j of the propagating TEM current waves should be $b_1 = i2\pi/\lambda$ for the forward propagating current and $b_2 = -i2\pi/\lambda$ for the backward propagating current.

The reflection coefficient is then simply

$$\rho = -\frac{A_2}{A_1}, \tag{6.17}$$

where A_1 is the amplitude of the forward travelling current wave and A_2 is the amplitude of the forward travelling current wave. The antenna impedance is then finally calculated from (6.14).

6.3.1 Antenna losses

Conductor losses can be approximated with the impedance boundary condition. The loss power in the impedance boundaries of the finite conductivity metal can be calculated by

$$P_c = \mathcal{R} \int_S \frac{1}{2} Z_s \left| \boldsymbol{J} \right|^2 \mathrm{d}S = \frac{1}{2} R_l \left| I_{in} \right|^2 , \tag{6.18}$$

where the loss resistance R_l is an effective resistance seen by the input current I_{in}. Conductor losses most often add the loss resistance as an additional series resistance increasing the real part of the antenna input impedance.

Ideal dielectric material would have no imaginary part of permittivity ϵ, i.e. no conductive losses. But in real materials the losses are present and cause imaginary part for the permittivity of the dielectric media. Since the losses are assumed to be small, the field penetrates well into the medium and the impedance boundary condition (2.40) can't be used for dielectric boundaries. Instead, the losses in a dielectric media must be calculated by directly using the representation formulas (2.14) and (2.15) to calculate the electromagnetic field inside the lossy media. The total dielectric loss power in a dielectric domain D with permittivity $\epsilon = \epsilon_{re} + i\epsilon_{im}$ is then calculated by

$$P_d = \frac{1}{2} \int_D \boldsymbol{E} \cdot \boldsymbol{J}^* \mathrm{d}V = \frac{\omega \epsilon_{im}}{2} \int_D \left| \boldsymbol{E} \right|^2 \mathrm{d}V. \tag{6.19}$$

Losses also change the input impedance Z_a of the antenna. Whereas conductor losses most often cause an additional series resistance increasing the real part of the antenna input impedance, the dielectric losses can cause a parallel conductance that decreases the real part of the antenna impedance. This depends on the geometry and can't be generalized.

The reflection caused by the impedance mismatch at the antenna input also causes less of the wanted signal to radiate. The input reflection can also be considered as one kind of a loss mechanism. The power transmission coefficient, i.e. the quotient of power P_t transmitted and the incident power P_i is calculated with the voltage reflection coefficient (6.11) as

$$\eta_i = 1 - \left| \rho \right|^2 . \tag{6.20}$$

But there is not a real need to directly match the antenna impedance itself to the reference impedance. If the antenna impedance is well behaved and mainly larger than the reference impedance Z_0 of the feeding line, the antenna can quite easily be matched to the reference impedance by designing an impedance matching circuit.

7 Programming and the data structures

This chapter describes the programming work and the datastructures used to construct the MoM system matrix (4.14) of EFIE-PMCHWT formulation. The numerical solver was implemented as a MEX-function, i.e. Matlab executable function programmed in C with a special interface replacing the standard main function. The advantage of MEX-functions over real external programs with a main function is that the results such as the system matrix can directly be returned to Matlab for post processing without a need to write to and read from a hard disk. In order to increase the portability of the implemented solver, the programming of the solver is done in pure C, i.e. Matlab is not called from the solver routine. The only sign of Matlab within the solver is the MEX interface that replaces the main function.

7.1 Datastructures

This chapter describes the data structures that are used to define the integral equation problem for the EFIE-PMCHWT solver routine. The problem is basically defined by describing the triangular mesh, the frequency, the constitutive parameters of the subdomains and the domain specific electric and magnetic basis and testing functions as in (4.11)-(4.14). The description of triangular mesh and domain specific basis and testing functions is non-trivial and is further treated here.

The triangular mesh in this thesis is described with stuctures for points, edges and triangles of the mesh. This kind of a geometry description can be classified as a rich structure since more than a minimal amount of info is stored in the structures.

The points of the mesh are stored in a table $\overline{\overline{\boldsymbol{P}}}$ of size $[3, NP]$, where NP is the number of points. The n:th column of the table contains the cartesian (x, y, z)-coordinates of the n:th point.

The edges of the mesh are described with a table $\overline{\overline{\boldsymbol{E}}}$ of size $[3, NE]$, where NE is the number of edges. The n:th column of the table describes the n:th edge of the mesh. The first two rows have the indices n_{p1} and n_{p2} of the points table for the startpoint and the endpoint of the edge and the third row includes the length of the edge, which is precalculated because it's needed many times in the computation of the MoM system matrix.

The triangles of the mesh are described with a table $\overline{\overline{\boldsymbol{T}}}$ of size $[7, NT]$, where NT is the number of triangles. The n:th column of the table describes the n:th triangle of the mesh. The first three rows have the indices n_{e1}, n_{e2} and n_{e3} of the edges of the triangle in $\overline{\overline{\boldsymbol{E}}}$ oriented counter-clockwise around the normal vector of the triangle that points to the domain with smaller domain index. The next three rows have the indices n_{p1}, n_{p2} and n_{p3} of the points of the triangle in $\overline{\overline{\boldsymbol{P}}}$ oriented similarly counter-clockwise as the edges so that the first local edge n_{e1} is between local points n_{p1} and n_{p2}. The seventh row includes the surface area of the triangle, which is precalculated because it's needed many times in the computation of the MoM system matrix.

As was said earlier, when the geometry is constructed, the normal vectors of the triangles always point to the domain with smaller domain index number. The domain index i_D of the free outer space is always the smallest as $i_D = 0$.

The type of the surface that a triangle represents defines the integral equation formulation used. This info for all the triangles is stored in a table $\overline{\overline{\boldsymbol{D}}}$ of size $[3, NT]$, where NT is the number of triangles. The first row indicates the type of surface of the triangle whereas second and third rows contain the two subdomains between which the triangle lies. In case of a PEC or PMC surface the two domains are marked as domain outside since the inner space of a perfect conductor isn't represented and domain specific basis and testing functions for those domains are not needed. Table 1 describes all different possibilities for the type of surface.

Table 1: The numbers that describe the type of surface of a triangle.

	Surface
0	Dielectric
1	PEC
2	PMC
3	IBC

The most crucial part of the datastructures used in this thesis are the structures that define the domain specific basis and testing functions. Since an RWG-function is related to a single edge of the triangle mesh, the problem of defining correct basis and testing functions is centered around the edges of the triangular mesh. In this thesis the solver routine is such that it can cope with any number of subregions around an edge, i.e. general material junctions [21] are solved. Special cases, such as combining the unknown RWG coefficients as single unknown and a PEC domain meeting dielectric domains, need to be treated correctly [20]. One good example of a special case is that the continuity of the tangential fields through any material interface forces the PEC boundary condition for all the domain specific RWG functions around an edge that has at least one PEC domain around it.

The correct behavior is achieved by defining the domain specific basis functions for $\boldsymbol{J}$ and $\boldsymbol{M}$ by using tables $\overline{\overline{\boldsymbol{J}}}$ and $\overline{\overline{\boldsymbol{M}}}$ of sizes $[5, NJ]$ and $[5, NM]$, where NJ is the number of domain specific RWG-functions for $\boldsymbol{J}$ and NM is the number of domain specific RWG-functions for $\boldsymbol{M}$. In the table, the first row indicates the domain index i_d of the domain specific basis function, second row is the edge index of the RWG-function in $\overline{\overline{\boldsymbol{E}}}$, the third and fourth rows include the triangle indices of the T_+/T_- in $\overline{\overline{\boldsymbol{T}}}$ and the fifth row includes the matrix index in the system matrix, i.e. basis functions that are to be combined have same matrix index.

Information that's found in $\overline{\overline{\boldsymbol{P}}}$, $\overline{\overline{\boldsymbol{E}}}$, $\overline{\overline{\boldsymbol{T}}}$ and $\overline{\overline{\boldsymbol{D}}}$ is used to construct $\overline{\overline{\boldsymbol{J}}}$ and $\overline{\overline{\boldsymbol{M}}}$ for arbitrary geometry. The routine that constructs these structures has been carefully validated, e.g. the orientation of the domain specific functions needs to satisfy (4.2)

and in order to combine the correct basis functions, the matrix indices need to be carefully constructed. After the structures are constructed, the system matrix of EFIE-PMCHWT (4.14) is constructed by simply testing the electric field integral equations of domain i with domain specific testing functions found in $\overline{\overline{\boldsymbol{J}}}$ and by testing the magnetic field integral equations of domain i with domain specific testing functions found in $\overline{\overline{\boldsymbol{M}}}$.

7.2 Speed optimization

In order to calculate real problems fast enough, the speed of the solver routine was optimized. The amount of memory usage is not minimized, but any data structures other than the system matrix having memory usage $\mathcal{O}(N^2)$ are avoided.

The solver uses threads in order to use all the CPU power available in the current multi-core CPU:s. The looping over basis functions is avoided. Instead looping over triangles is used in order to avoid doing numerical integration on a triangle numerous times. The integrals as in Chapter 4.3 are then constructed piecewise from the integrals including either T_+ or T_- of basis or testing function. The accuracy of the numerical integration, i.e. the amount of sample points is reduced when the basis function and the testing function are far enough away from each other, which further reduces the computation time without reducing the accuracy notably.

8 Results

This chapter includes the descriptions and the results of the simulations that were done for this work. The numrical results are first validated by solving plane wave scattering from two spherical scatterers and comparing the numerical results to the analytical results given by Mie-series. After validation, two different antenna problems are solved and antenna parameters are calculated from the numerical results.

8.1 Validation

The scattering of a plane wave from a metallic PEC sphere was solved in order to validate the numerical results of EFIE. The incident plane wave is linearly polarized with electric field $\boldsymbol{E} = E\hat{\boldsymbol{u}}_x$ and direction of propagation is to the positive z-axis. The frequency of the problem is $f = 300$ MHz and the radius of the sphere is $r = 1$ m, i.e. approximately one wavelength λ. Both the analytic scattering solution by Mie-series [37] and the numerical EFIE solution were calculated. The resulting bistatic radar cross sections

$$\sigma_{RCS} = \lim_{r\to\infty} 4\pi r^2 \frac{|\boldsymbol{E}^s|^2}{|\boldsymbol{E}^p|^2} \tag{8.1}$$

of the results are compared in Figure 15 in decibels compared to m^2 as $\sigma'_{RCS} = 10\log_{10}(\sigma_{RCS})$ dBm^2.

As is well seen from the results, the numerical EFIE results show almost perfect agreement against the analytical results given by the Mie series. Most surprising is the accuracy of the results even at the lower levels at the deep null of scattering in E-plane. One of the reasons for the high accuracy most definitely is good modeling of the geometry, since in this simulation the surface area of the discretized sphere is matched by hand to the surface area $A_s = 4\pi r^2$ of the real sphere. The number of triangles in this simulation was $NT = 4500$, and the number of unknown RWG functions, i.e. the number of edges, was $N = 6750$. This corresponds to a memory consumption of 680 MiB for the system matrix, which easily fits into memory space of typical PCs.

A similar scattering problem was also solved for a homogeneous magneto-dielectric sphere with complex relative constitutive parameters $\epsilon_r = 4 + 0.2i$ and $\mu_r = 2 + 0.1i$. Both the analytic solution and the numerical PMCHWT solution of the resulting bistatic radar cross sections are given in Figure 16.

As is well seen, the numerical PMCHWT results show almost perfect match to the analytical results. As was the case with EFIE for the PEC sphere, the results are very accurate even at the lower scattering levels, which is a sign of very high accuracy. The number of triangles in this simulation was $NT = 9536$, and the number of unknows was $N = 14304$. This corresponds to a memory consumption of 3 GiB for the system matrix, which still fits into memory space of many PCs

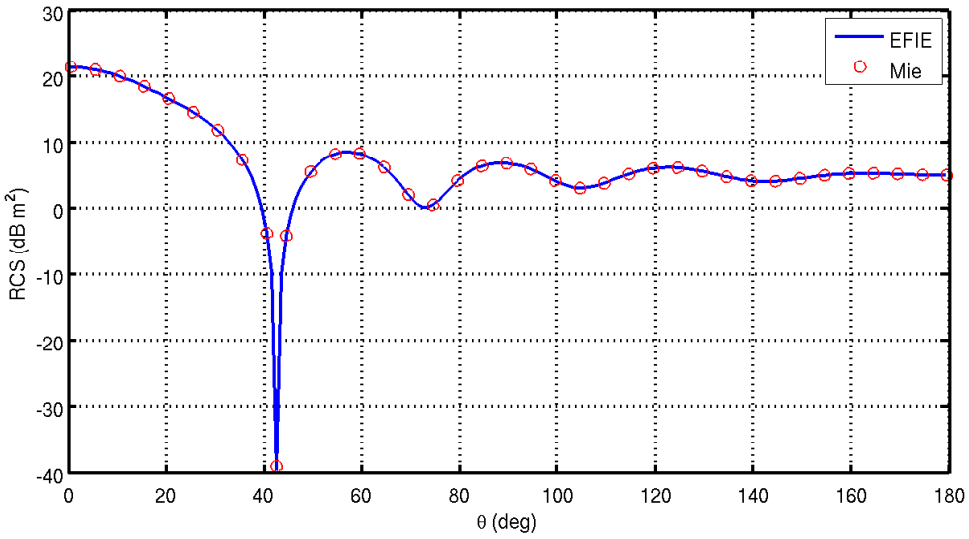

(a)

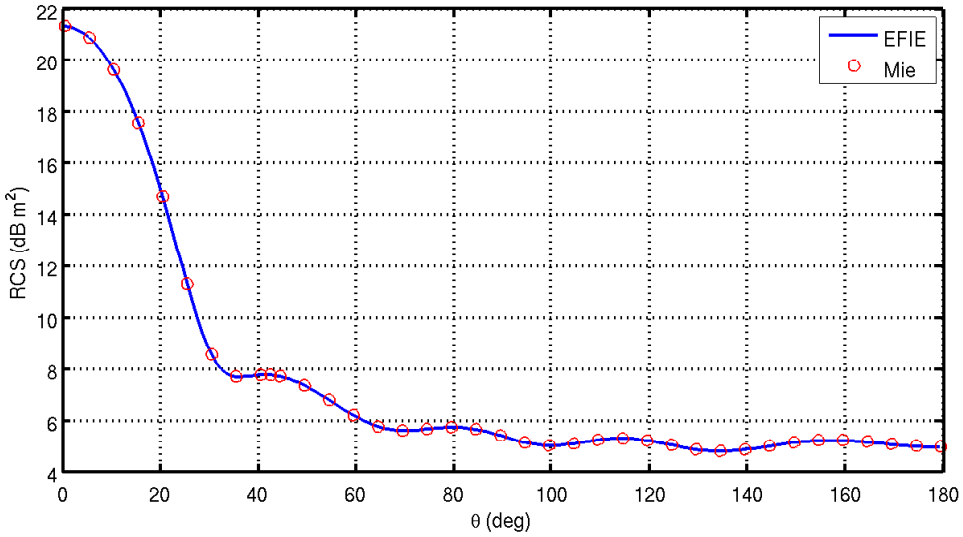

(b)

Figure 15: Bistatic radar cross section of a PEC sphere of radius $r_s = 1$ m at frequency $f = 300$ MHz in a) E-plane ($y = 0$). b) H-plane ($x = 0$). Both the numerical surface integral equation solution by EFIE and the analytical solution by Mie series are included. The angle θ is the angle between the scattering direction and the direction of arrival of the incident linearly polarized plane wave as seen from the scatterer.

nowadays.

This concludes the validation. The results that were achieved clearly show that the surface integral equation method with a good formulation and the divergence conforming RWG basis functions and testing functions can give so accurate results

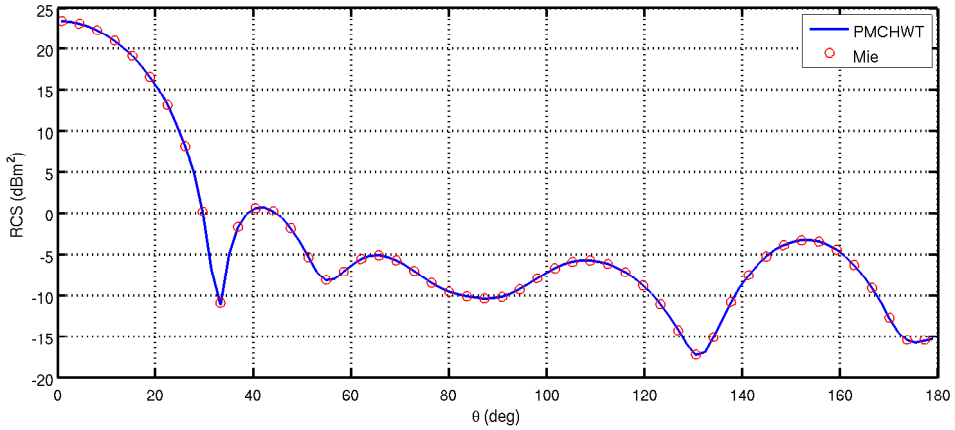

(a)

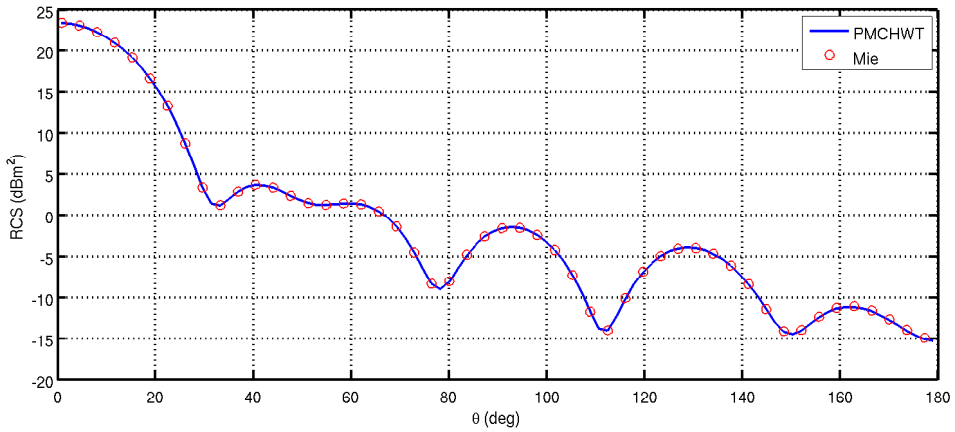

(b)

Figure 16: Bistatic radar cross section of a sphere of radius $r_s = 1$ m with relative constitutive parameters $\epsilon_r = 4 + 0.2i$ and $\mu_r = 2 + 0.1i$ at frequency $f = 300$ MHz in a) E-plane ($y = 0$). b) H-plane ($x = 0$). Both the numerical surface integral equation solution by PMCHWT and the analytical solution by Mie series are included. The angle θ is the angle between the scattering direction and the direction of arrival of the incident linearly polarized plane wave as seen from the scatterer.

that by using these kind of numerical simulations as a design tool, the amount of measured prototypes in design processes of e.g. antennas can be significantly reduced or ideally the prototyping can almost be avoided. If the simulation results given by the design tools aren't accurate enough, a lot more prototyping is needed in practice.

8.2 Dipole antenna

A dipole antenna made of a cylindrical wire was simulated. Dipole antenna has very well known characteristics and serves as a good reality check for the antenna parameter calculations. The simulated dipole antenna is such that the length of the wire is half a wavelength λ_0 at frequency $f_0 = 1$ GHz. The wire is assumed to be a circular cylinder with a radius of $r_c = \lambda_0/300$. Delta-gap is used as the feed of the antenna around the wire at the center.

The simulation is done over a wide frequency range $f = 0.5 \ldots 8$ GHz. The resulting input impedance calculated by (6.12) is given in Figure 17.

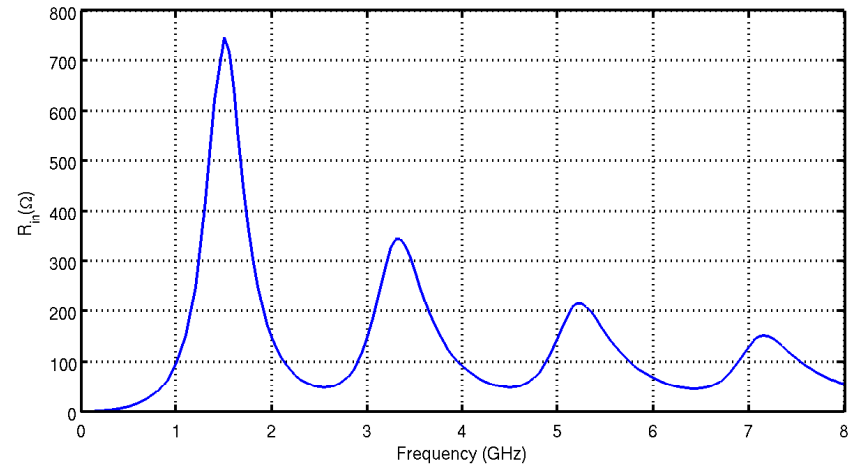

(a)

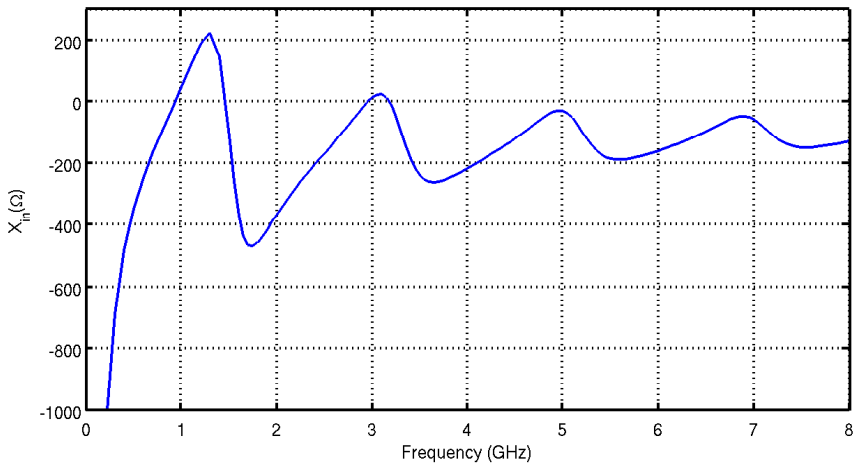

(b)

Figure 17: Input impedance of a cylindrical wire dipole antenna of length $\lambda_0/2$ at frequency $f_0 = 1$ GHz. The radius of the wire is $r_c = \lambda_0/300$.

The lowest resonance frequency, i.e. the frequency at which the input impedance is purely resistive, is $f_r = 935$ MHz. This is in line with the previously measured

results [32]. The shape of the impedance curve is also similar to the results published earlier.

The directivity pattern (5.11) is also calculated over the frequency band $f = 0.5 \ldots 8$ GHz. It was verified with the results that dipole only radiates $\hat{\boldsymbol{u}}_\theta$-polarization and that the directivity pattern is constant as a function of ϕ. The directivity is given in three different discrete angles $\theta = 90°, 120°, 150°$ as a function of frequency in Figure 18. The maximum directivity on the main axis $\theta = 90°$ is $D_{max,90} = 4.8$ dBi at frequency $f_{max,90} = 2.35$ GHz. Global maximum of the directivity on this frequency band is $D_{max} = 5.7$ dBi at frequency $f_{max} = 7$ GHz to angle $\theta = 150°$ (or $\theta = 30°$). The maximum directivity at $f = 1$ GHz is $D_{f_0} = 2.2$ dBi, which is as expected, since the directivity of an infinitely thin half wavelength dipole should be 2.15 dBi [32].

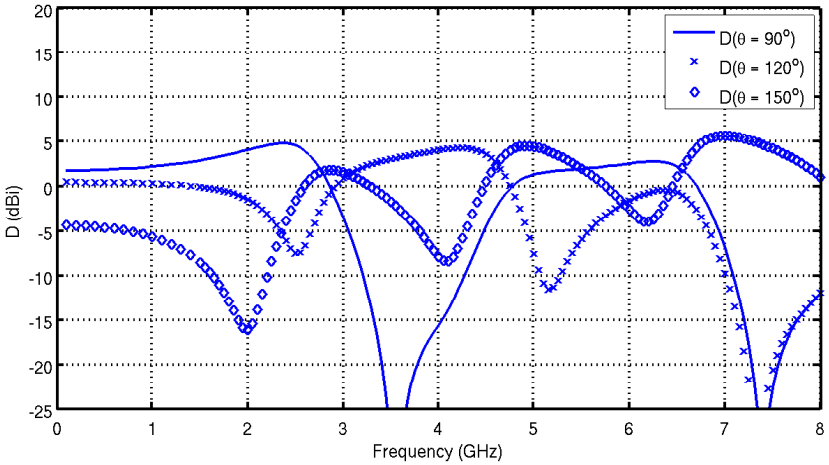

Figure 18: Frequency dependence of directivity of a cylindrical wire dipole antenna of length $\lambda_0/2$ and wire radius $\lambda_0/300$ at frequency $f_0 = 1$ GHz to angles $\theta = 90°, 120°, 150°$. The dipole is directed along the z-axis and the directivity is constant as a function of ϕ.

The 3D directivity pattern of the dipole antenna is given at two frequencies $f_1 = 1$ GHz and $f_2 = 3$ GHz in Figures 19 and 20. The dependence of the directivity on angle θ at the interesting frequency $f = 2.35$ GHz of maximum axial directivity is given in Figure 21.

As is well seen, the directivity pattern at $f_1 = 1$ GHz has a shape similar to the directivity pattern $D(\theta) = \sin^2(\theta)$ of a small dipole, though the maximum directivity of the half-wavelength dipole is higher and the pattern is more directive than that of a small dipole, as is expected. The shape of the directivity pattern at $f_1 = 1$ GHz is also very well seen in Figure 18. The directivity pattern is also as expected at the higher frequency $f_2 = 3$ GHz.

The loss power and the resulting loss resistance (6.18) of the dipole antenna is also calculated over the frequeny band $f = 0.5 \ldots 8$ GHz. Assuming that the antenna is made of annealed copper with conductivity $\sigma_{cu} = 58$ MS/m, the computed loss

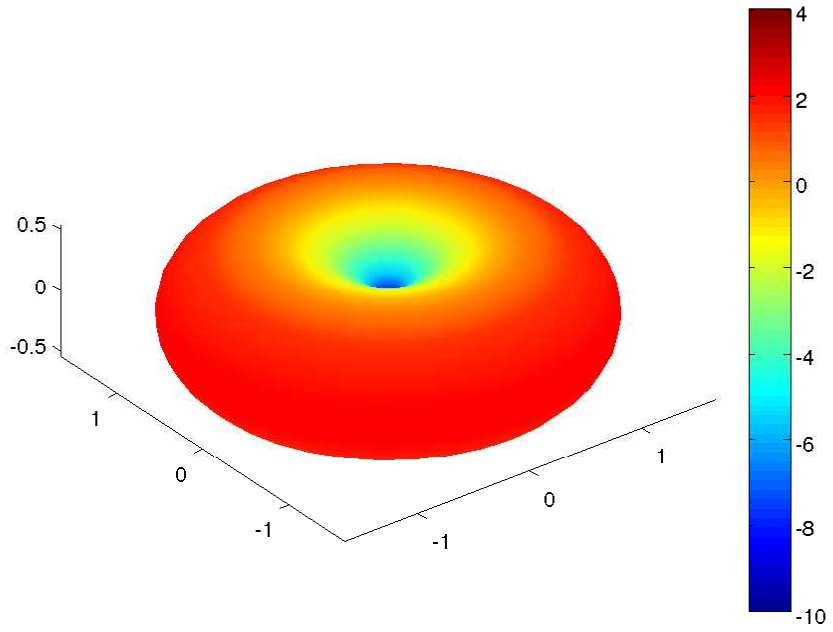

Figure 19: 3D directivity pattern of a cylindrical wire dipole of length $\lambda/2$ and wire radius $\lambda/300$ at frequency 1 GHz.

resistance remains under 0.7Ω through the whole frequency band, so it doesn't alter the real part of the antenna input impedance that much. However, the loss resistance affects the maximum available efficiency. The radiation efficiency which neglects the impedance mismatch at the antenna-cable interface is given in Figure 22.

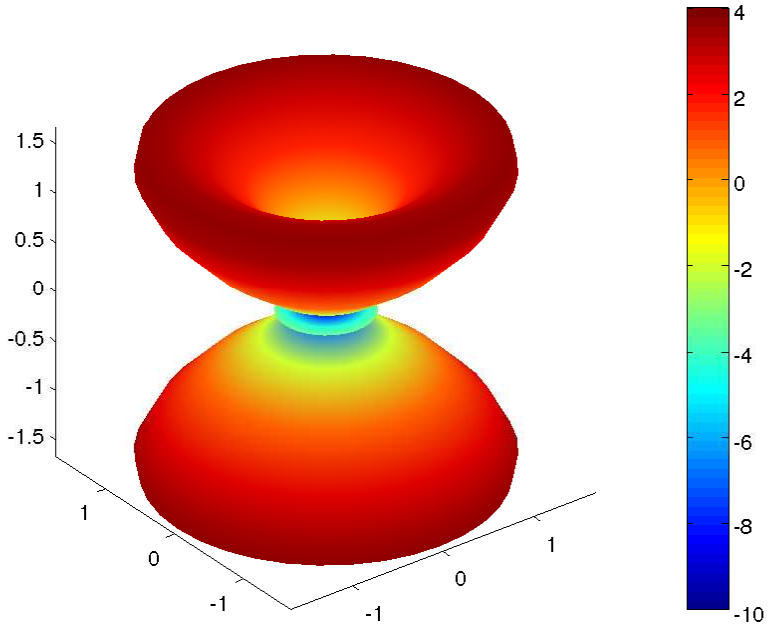

Figure 20: 3D directivity pattern of a cylindrical wire dipole of length $3\lambda/2$ and wire radius $\lambda/100$ at frequency 3 GHz.

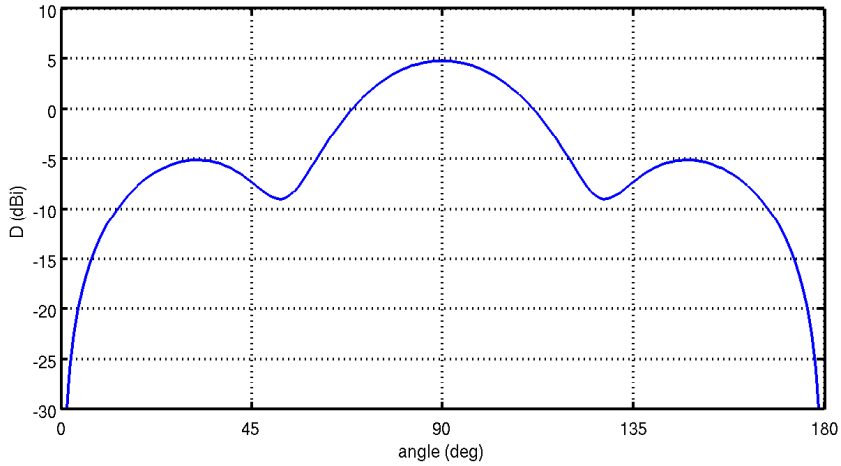

Figure 21: Directivity of a cylindrical wire dipole antenna of length $\lambda_0/2$ and wire radius $\lambda_0/300$ at frequency $f_0 = 1$ GHz as a function of θ calculated at frequency $f = 2.35$ GHz.

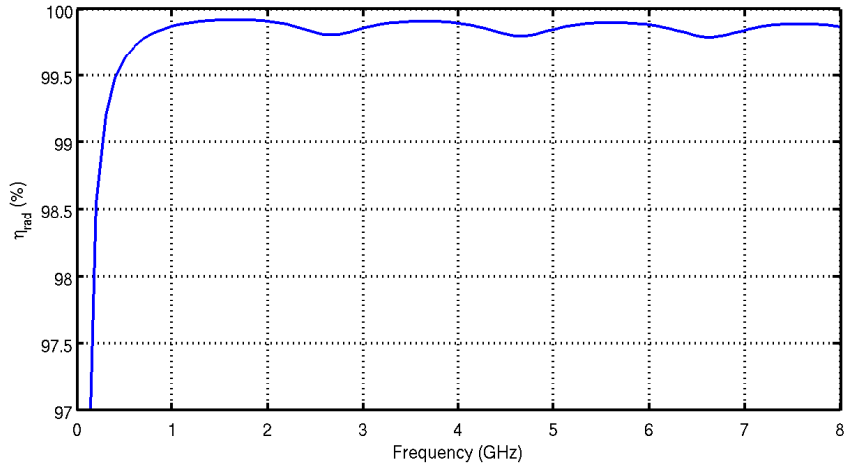

Figure 22: Radiation efficiency of a cylindrical wire dipole antenna of length $\lambda_0/2$ at frequency $f_0 = 1$ GHz as a function of frequency.

The radiation efficiency remains over 99.5 % through the frequency range $f = 0.5 \ldots 8$ GHz, so the conductive losses are neglicible. However, the reflection caused by the impedance mismatch at the antenna-feed interface without any impedance matching circuit causes less of the signal power to get through to the antenna. The resulting absolute value of the reflection coefficient $\rho = S_{11}$ (6.11) when connected either to a 50Ω or 75Ω transmission line is given in Figure 23.

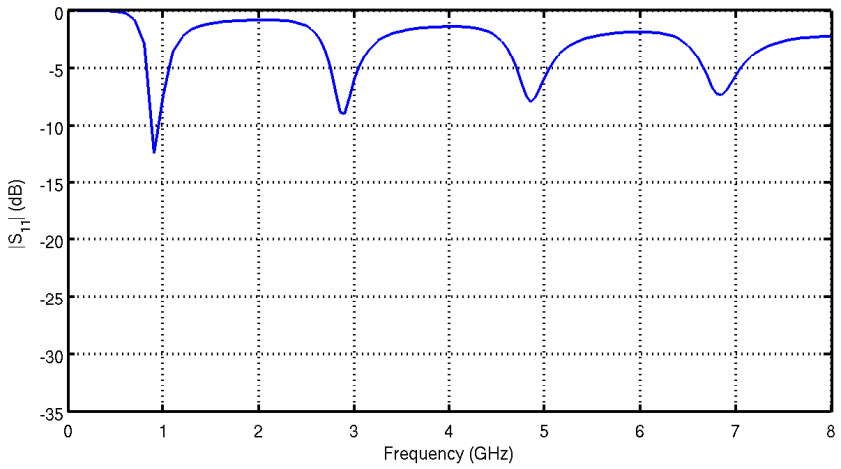

(a)

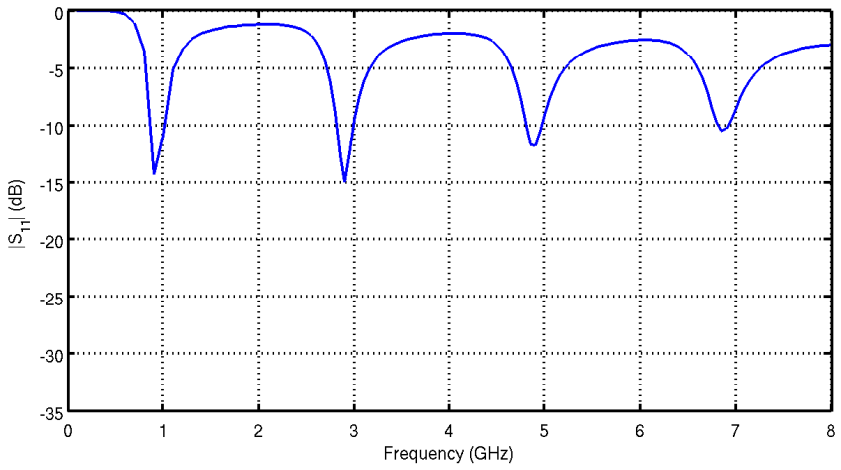

(b)

Figure 23: Reflection coefficient at the antenna cable interface looking from a) 50 Ω transmission line. b) 75 Ω transmission line.

The impedance is quite well matched near the lowest resonance frequency slightly below the half wavelength frequency $f_0 = 1$ GHz. However, simple dipole antenna can't be used over a really wide frequency range without an impedance matching circuit.

The resulting total gain to angles $\theta = 90°, 120°, 150°$ including the conductive losses and the reflection loss (6.20) caused by impedance mismatch when connected to a

75Ω transmission line is given in Figure 24.

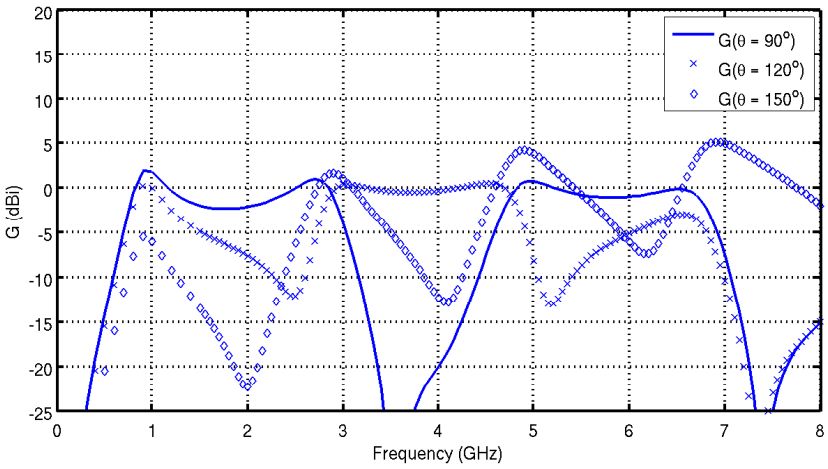

Figure 24: Frequency dependence of gain of a cylindrical wire dipole antenna of length $\lambda_0/2$ and wire radius $\lambda_0/300$ at frequency $f_0 = 1$ GHz to angles $\theta = 90°, 120°, 150°$. Conductor losses on the annealed copper surface and the insertion loss when connected to a 75Ω transmission line are included as losses. The dipole is directed along the z-axis and the gain is constant as a function of ϕ.

Maximum gain on the main axis $\theta = 90°$ is $G_{90,max} = 2.1$ dBi at frequency $f_{90,max} = 940$ MHz. The antenna efficiency is very good over this frequency range, since the conductor losses and losses caused by the impedance match at this frequency only cause loss of about 0.1 dB, which is negligible. The number of triangles in this simulation was $NT = 1464$, and the number of unknows was $N = 2196$. This corresponds to a memory consumption of 72 MiB for the system matrix, which very easily fits into memory space of all PCs nowadays.

8.3 Patch antenna

As a more general case, a patch antenna with a coaxial probe feed was simulated. The geometry of the antenna is represented in Figure 25

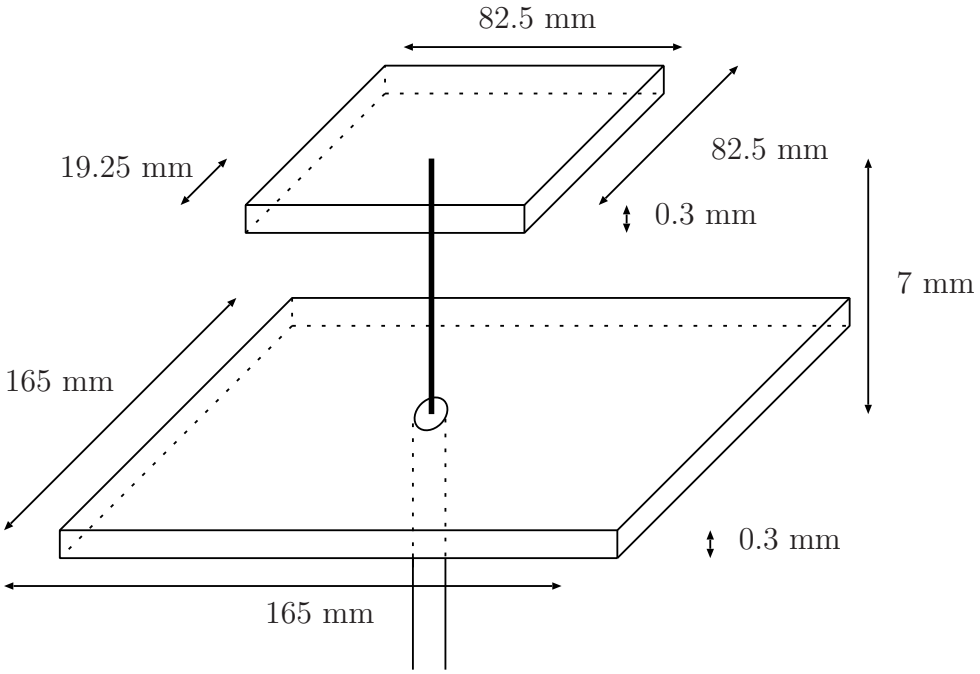

Figure 25: Geometry of the patch antenna with coaxial probe feed. The coaxial probe is centered on the ground plane and along the other dimension of the patch element.

The geometry is similar to that measured and simulated in [38, 39] with just an exception that the size of the ground plane is here only 165 mm × 165 mm compared to the original 600 mm × 600 mm ground plane. This shouldn't alter the antenna parameters that much because even the smaller ground plane should be large enough for the patch element to see the ground plane as being close to infinite. The patch antenna will also be simulated with a dielectric substrate between the lower side of the antenna element and the upper side of the ground plane.

Compared to the dipole antenna, the geometry of the patch antenna is more challenging to discretize well enough because of the expected rapid change of the field close to the coaxial feed and edges [40] of the geometry. The triangular mesh needs to be denser in these regions [41]. This resulted as a lot of optimization work for the triangularization of the patch geometry that was solely done by hand. Some details of the resultant triangularization that's used in the simulations of this section is presented in Figure 26.

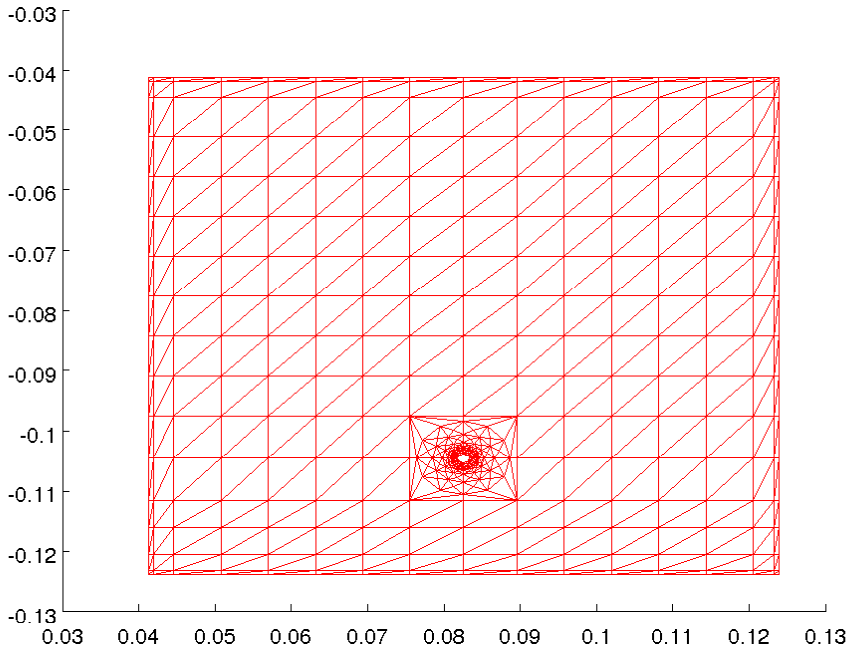

(a)

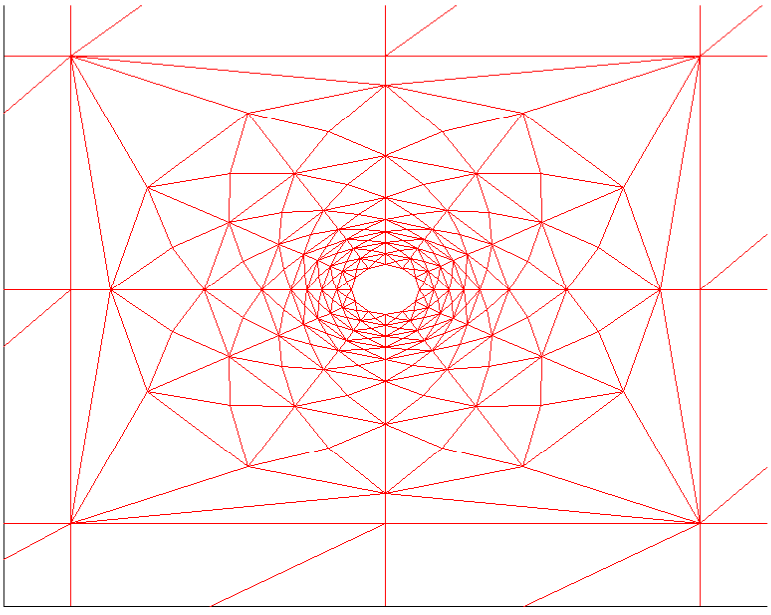

(b)

Figure 26: Triangularization of the patch antenna geometry a) on infinitely thin metallic patch element. b) close to the coaxial cable interface.

The patch antenna is only simulated with the accurate coaxial feed model. This means that the coaxial cable extension also needs to be added to the discretized geometry. The patch antenna is first simulated with a thin sheet approximation [13] applied for the ground plane and the patch element. The thin sheet approximation means that the thickness of the metallic sheet is ignored and the unknown surface current densities on the upper side and the lower side of the sheet are combined as single unknown, since they create equivalent fields in a homogeneous media. The antenna input impedance calculated from the simulation results with cable extension of length $\lambda_c/2$ at frequency $f_c = 1.54$ GHz is compared to the measured input impedance [38, 39] in Figure 27.

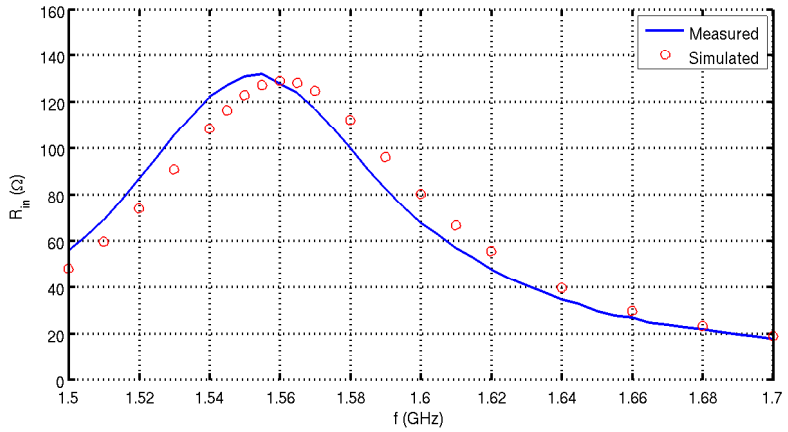

(a)

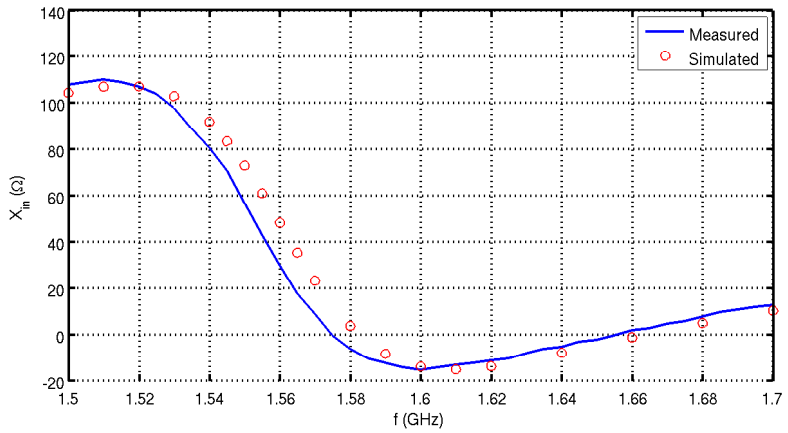

(b)

Figure 27: Input impedance of a coaxial probe fed patch antenna a) real part. b) imaginary part. The simulation is done with thin sheet approximation on both the ground plane and the antenna element. The length of the coaxial cable extension is $\lambda_c/2$ at frequency $f_c = 1.54$ GHz.

As is well seen from the impedance results, the shape of the impedance curve is correct, but the resonant frequency at which the real part of the impedance peaks

is not estimated accurately. This is as expected, since the thickness of the metallic sheet is not taken into account in this simulation. As is well known, adding thickness to the metallic sheet of microstrip structures such as the patch element makes them electrically seem larger [42]. This fact is often ignored in numerical simulations and the thin sheet approximation is widely used, which cannot be done if the most accurate results are desired.

The length of the coaxial cable extension is such, that at $f_c = 1.54$ GHz the impedance (6.9) seen from the antenna-cable interface into the short circuited cable would theoretically tend to zero. This seems to pose no problems for the antenna impedance results. The zero impedance actually means that the cable extension basically forces the tangential electric field on coaxial opening to zero, which is the PEC boundary condition (2.12). As the magnetic frill model described in Chapter 6.1.2 replaces the coaxial aperture itself on a ground plane with PEC, the result achieved here justifies the use of frill model. A good question is that how this correctness of the zero impedance at the aperture would change in a situation, when the ground plane is of smaller size or when there's no ground plane.

The patch antenna was also simulated without the thin sheet approximation. In order to test the quality of the coaxial feed model, the patch antenna is now simulated with two different lengths of the coaxial cable extensions. The antenna input impedance calculated from the simulation results with cable extension of length $3\lambda_c/4$ at frequency $f_c = 1.54$ GHz is compared to the measured impedance [38, 39] in Figure 28.

As is well seen from the impedance compared to the measured result, the results are false around frequency $f = 1.525$ GHz. This almost matches the frequency $f_c = 1.54$ GHz at which the impedance as seen from the opening of the coaxial cable into the short circuited cable would theoretically tend to $Z_b = -j\infty\Omega$. This clearly indicates that coaxial cable extension lengths which result as $|Z_b| = \infty$ should be avoided. However, the results well above this frequency seem to be very accurate, so better results could be achieved by simply lenghtening the cable extension so that the frequency at which the length is $l_c = 3\lambda/4$ would be below the frequency range of interest.

The patch antenna without the thin sheet approximation was also simulated with cable extension of length $0.875\lambda_c$ at frequency $f_c = 1.54$ GHz. The resulting input impedance is compared to the measured impedance in Figure 29.

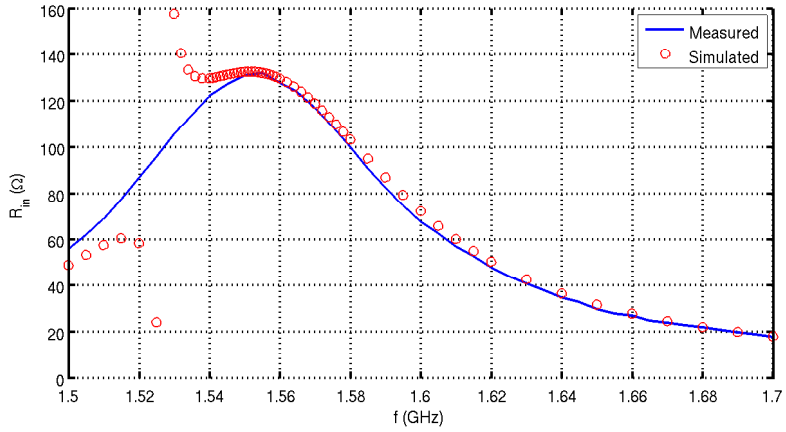

(a)

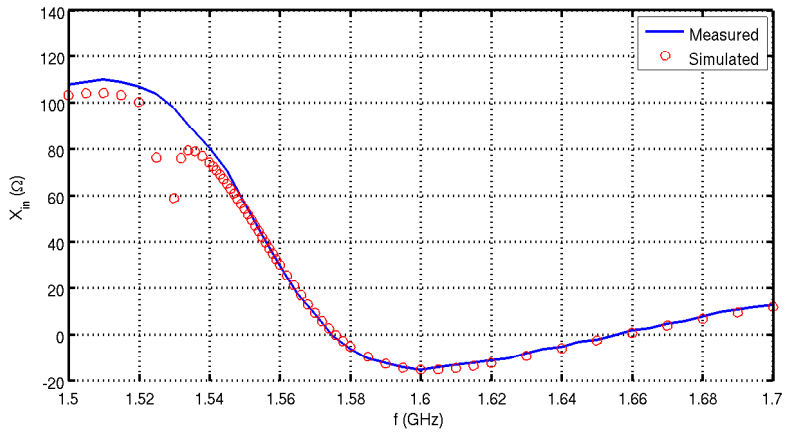

(b)

Figure 28: Input impedance of a coaxial probe fed patch antenna a) real part. b) imaginary part. The length of the short circuited coaxial cable extension is $3\lambda_c/4$ at frequency $f_c = 1.54$ GHz.

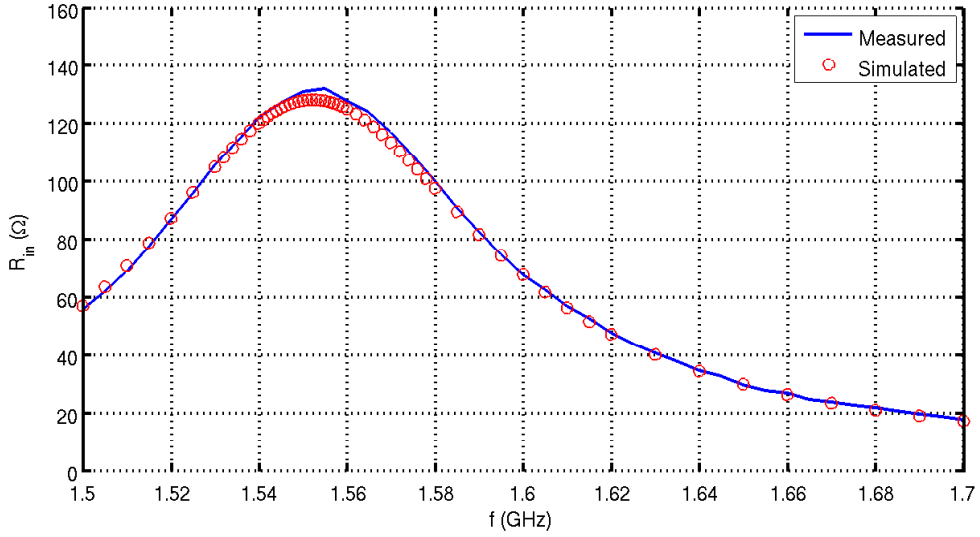

(a)

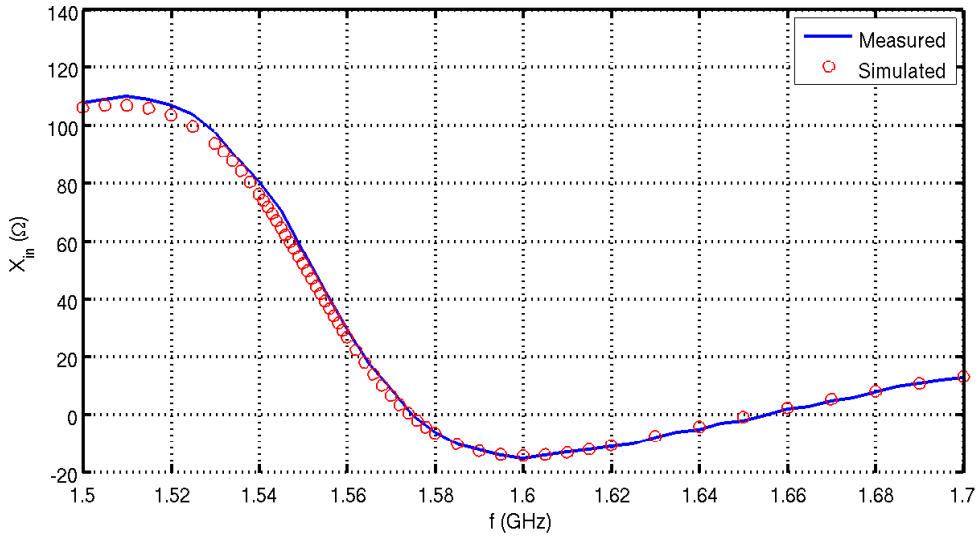

(b)

Figure 29: Input impedance of a coaxial probe fed patch antenna a) real part. b) imaginary part. The length of the short circuited coaxial cable extension is $0.875\lambda_c$ at frequency $f_c = 1.54$ GHz.

As is well seen, the resonance problem is removed. The antenna impedance actually matches very well to the measured input impedance. The frequency of maximum input resistance is almost perfectly estimated by the numerical result. Only real difference between the measured and numerical results is for the maximum value of the input resistance, which is 131.13 Ω in the measurements [39], and 128.18 Ω for the numerical results. The simulated value of maximum input resistance is actually very close to the simulated value of 128.28 Ω achieved in [39]. The frequency of maximum resistance is estimated better in this work, most probably because the thickness of the metallic sheet is taken into account here, which is not the case for the layered media model in [39].

The solution for the surface current density $\boldsymbol{J}$ on the lower side of the patch element is given in logarithmic units dB(A/m) in Figures 30 and 31. As is well seen, the surface current distribution tends to oscillate in the y-direction, which means that the E-plane of the antenna, i.e. the plane where the electric field is assumed to oscillate, is $x = 0$. Similarly the H-plane should be $y = 0$.

The directivity patterns (5.12) of the patch antenna are calculated over the frequency band $f = 1.5 \ldots 1.7$ GHz. The directivity of both the $\hat{\boldsymbol{u}}_\theta$-polarization and the $\hat{\boldsymbol{u}}_\phi$-polarization in E-plane ($x = 0$) and H-plane ($y = 0$) are given in three different discrete angles $\theta = 0°, 30°, 60°$ as a function of frequency in Figures 32-33. The maximum directivity on the main axis $\theta = 0°$ is $D_{max,0} = 9.35$ dBi at frequency $f_{max,0} = 1.6$ GHz.

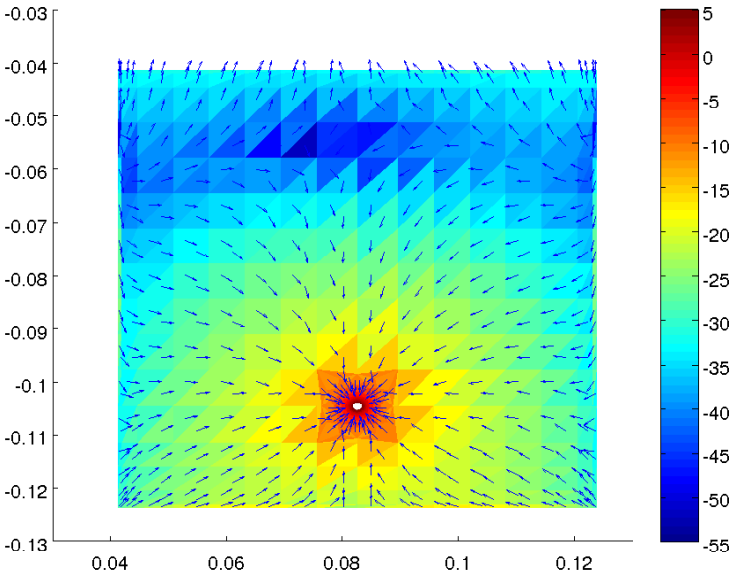

(a)

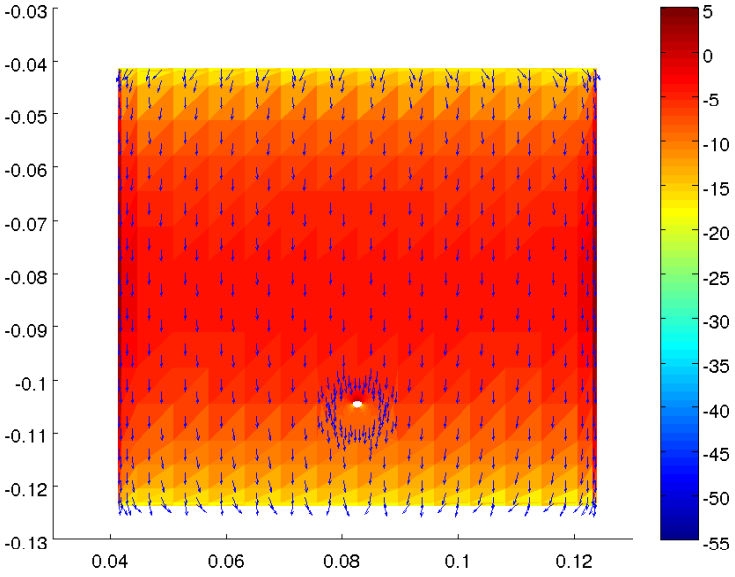

(b)

Figure 30: Equivalent surface current density $\boldsymbol{J}$ in units dB(A/m) on the lower side of the patch element at two time instances a) $t = 0$ and b) $t = T_0/4$ in the first half of the period T_0 at frequency $f_0 = 1.55$ GHz.

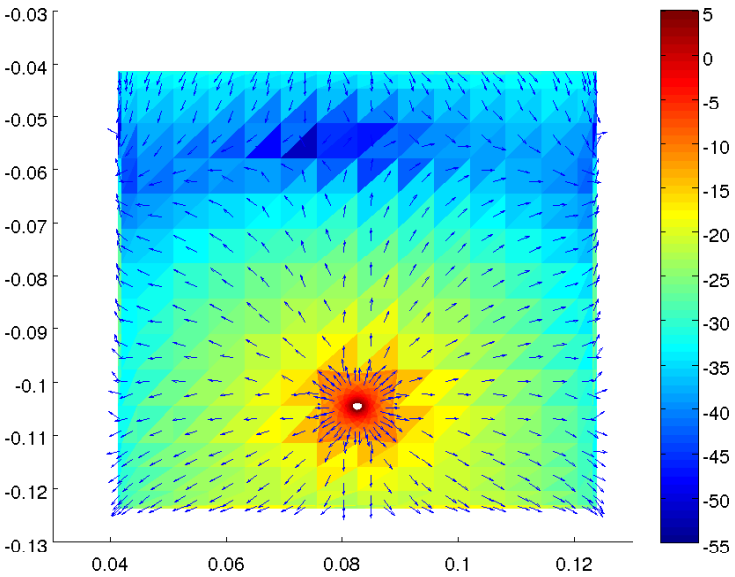

(a)

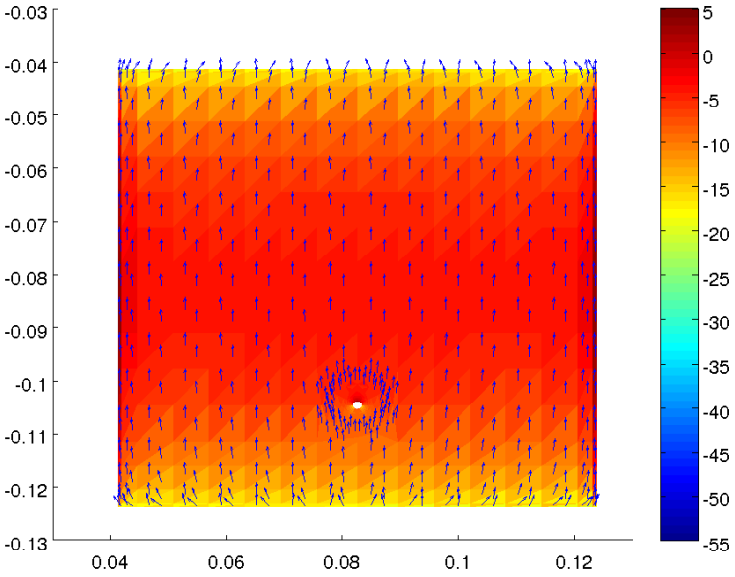

(b)

Figure 31: Equivalent surface current density $\boldsymbol{J}$ on the lower side of the patch element at two time instances a) $t = T_0/2$ and b) $t = 3T_0/4$ in the second half of the period T_0 at frequency $f_0 = 1.55$ GHz.

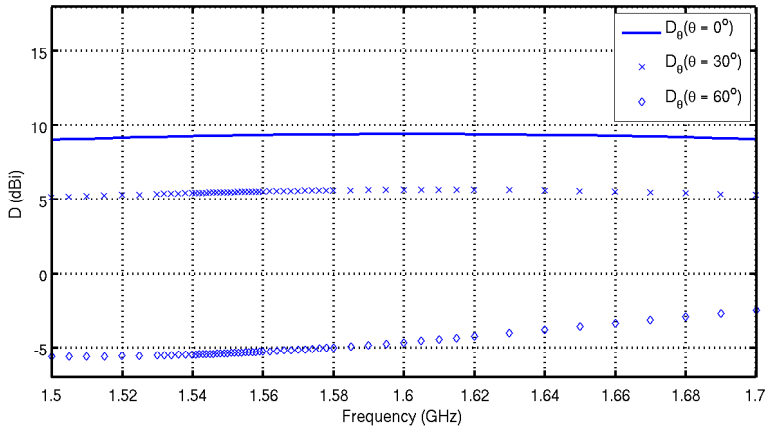

(a)

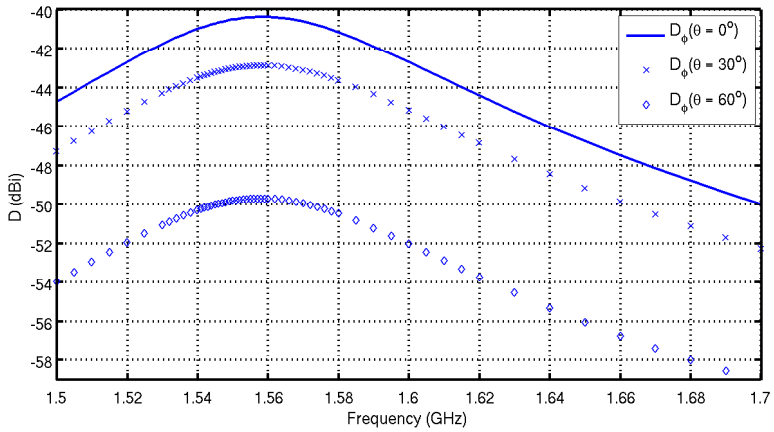

(b)

Figure 32: Frequency dependence of directivity of microstrip patch antenna in E-plane ($x = 0$) to angles $\theta = 0°, 30°, 60°$ for a) $\hat{\boldsymbol{u}}_\theta$-polarization. b) $\hat{\boldsymbol{u}}_\phi$-polarization. The patch element and the ground plane are on planes of constant z planes.

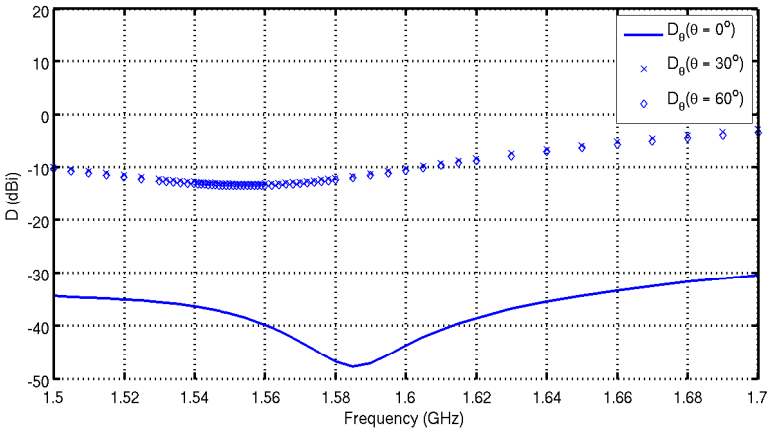

(a)

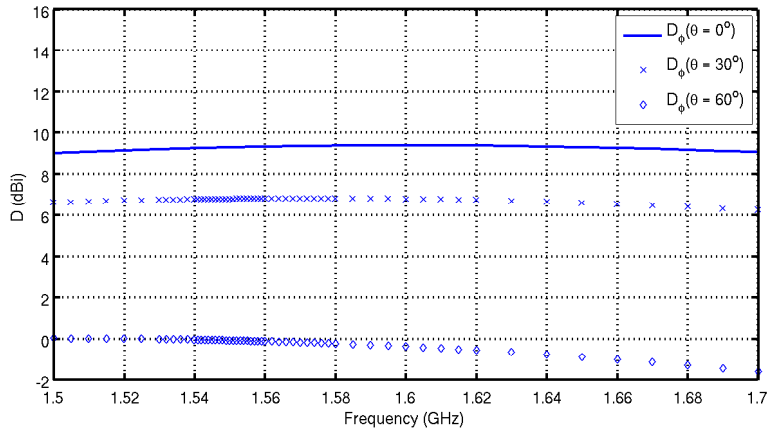

(b)

Figure 33: Frequency dependence of directivity of microstrip patch antenna in H-plane ($y = 0$) to angles $\theta = 0°, 30°, 60°$ for a) $\hat{\boldsymbol{u}}_\theta$-polarization. b) $\hat{\boldsymbol{u}}_\phi$-polarization. The patch element and the ground plane are on planes of constant z planes.

The directivity patterns (5.12) of the patch antenna were calculated at frequency $f = 1.59$ GHz both in the E-plane ($x = 0$) and in the H-plane ($y = 0$). The resulting directivity patterns are given in Figure 34.

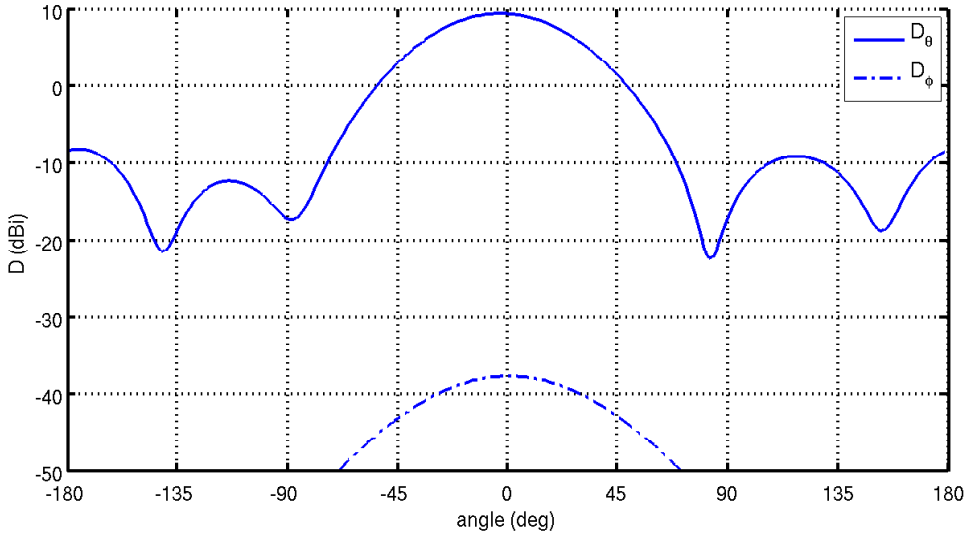

(a)

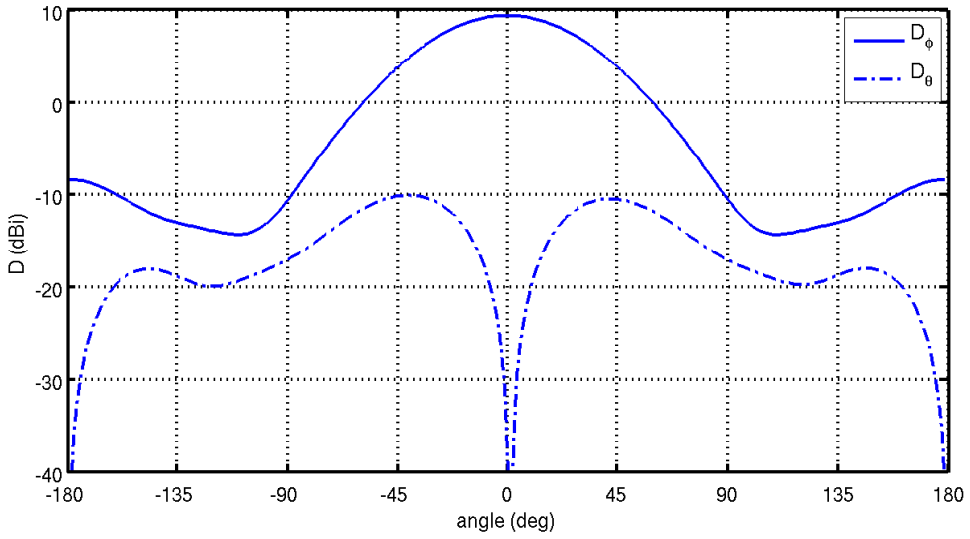

(b)

Figure 34: Directivity patterns D_θ and D_ϕ of the $\hat{\boldsymbol{u}}_\theta$ and $\hat{\boldsymbol{u}}_\phi$ polarizations a) in E-plane. b) in H-plane.

The results match surprisingly well to the measured patterns presented in [38]. This just shows the accuracy of the method when the discretization of the geometry is done well enough. Just to show the distribution of the surface current on the antenna, the resulting vector norm $|\boldsymbol{J}|$ of the equivalent electric surface current $\boldsymbol{J}$ at frequency $f = 1.55$ GHz is given for the whole geometry (not in scale) in Figure

35.

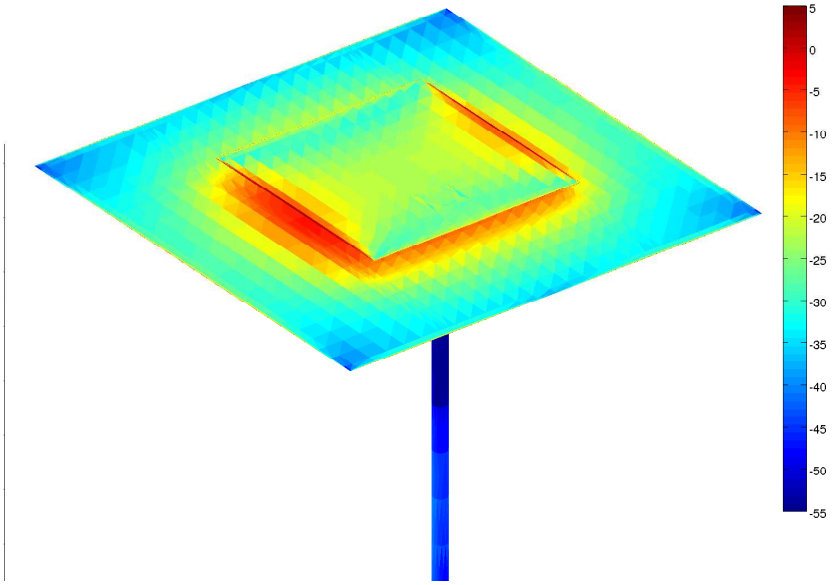

Figure 35: Equivalent electric surface current density $\boldsymbol{J}$ on the outer surface of the patch antenna .

As is well seen, the higher values of the surface current density on the ground plane extend well beyond the area covered by the patch element. This effective area is actually partially enlarged by the non-zero thickness of the patch. The surface current in these figures presented is shown as constant on triangles. In reality the RWG-functions have first order polynomial terms on triangles, so the exact surface current is smoother. And the field of the approximate surface current out of the surface is even smoother, since the field is given by integrating the surface current density. Integration at best smooths the result a lot, as e.g. EFIE does.

As a final result, a similar patch antenna was also simulated with a dielectric substrate between the ground plane and the patch element. In order to see the effect of dielectric losses, the real part of the permittivity remained unchanged, and the permittivity of the substrate was $\epsilon_s = (1 + 0.01)\,\epsilon_0$. The problematic coaxial cable extension length of $3\lambda_c/4$ at frequency $f_c = 1.54$ GHz is used in order to see the effect of losses on the resonance seen in Figure 28. The resulting input impedance is compared to the measured impedance with vacuum as substrate in Figure 36.

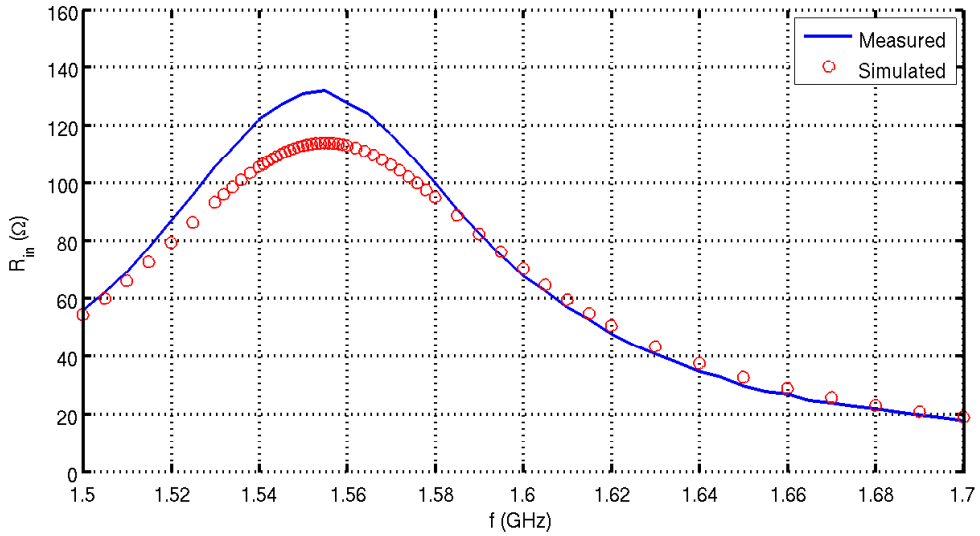

(a)

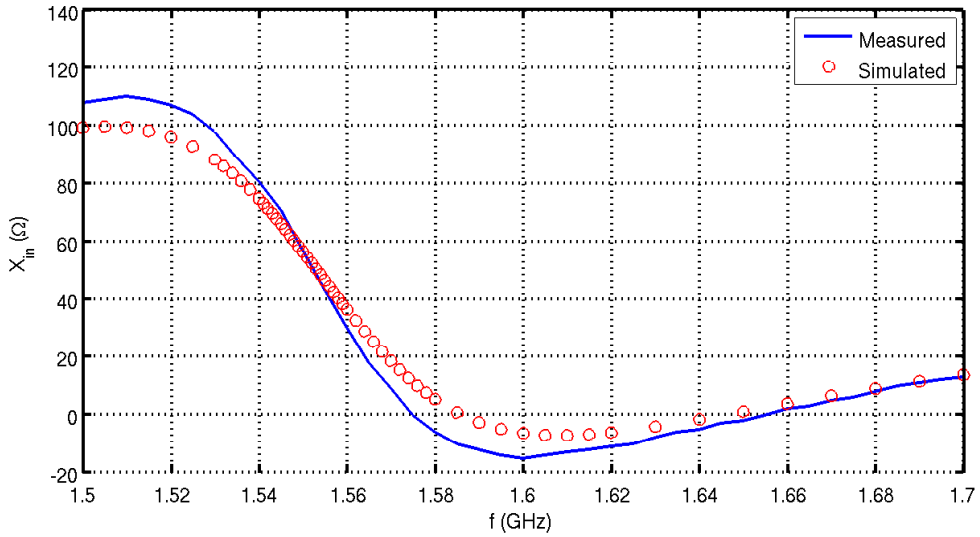

(b)

Figure 36: Input impedance of a coaxial probe fed patch antenna with additional losses in substrate with permittivity $\epsilon_s = (1 + 0.01i)\,\epsilon_0$. Both a) the real part and b) the imaginary part of the antenna impedance are given. The length of the short circuited coaxial cable extension is $3\lambda_c/4$ at frequency $f_c = 1.54$ GHz.

As is well seen, the resonance problem seems to be removed after losses are present. This resonance problem is not further studied in this thesis, but would be well worth of further research. The dielectric losses also drop the maximum value of real part of the antenna impedance, which is as expected, since the dielectric losses add a leakage current between the patch element and the ground plane. The Q-value also drops, which is seen as a reduced rate of change of imaginary part of the antenna impedance as a function of frequency.

8.4 Analysis of the results

This chapter includes a brief summarizing analysis of the results given in this thesis. An error analysis is also included.

8.4.1 Accuracy

As is well seen from the results of Chapter 8, the results that were achieved with the EFIE-PMCHWT solver are very accurate. The scattering of a plane wave from a spherical scatterers closely matches to the analytical results. The results of the antenna analysis were also very accurate. The results for the dipole antenna are similar to the results measured and simulated earlier. The results for the patch antenna are also very accurate, but the accurate results need a well optimized triangular mesh and simulation models.

The feed model as explained in Chapter 6.1.3 gives accurate results when the length l_c of the coaxial cable extension isn't related to the wavelength λ as $l_c/\lambda \approx 0.25 + n \cdot 0.5$, when the impedance seen from the antenna-cable interface into the cable tends to infinity. This kind of a coaxial model has been used earlier [13], but the problems with certain lengths of the cable extension haven't been documented to my knowledge.

8.5 Error analysis

The results achieved by the MoM solution of EFIE-PMCHWT surface integral equation formulation seem to be very accurate. The reliability of the results with the structures of size comparable to wavelength should be good. However, the EFIE-PMCHWT formulation has a well known low frequency breakdown in numerics, which can impose problems with details of size small compared to the wavelength. This can be avoided with preconditioners such as the those based on Calderon identities [43].

The coaxial feed model as used in this thesis has serious problems with certain lengths of the cable extension. This weakens the reliability of the results. In order to avoid this problem, the reflection caused by the short circuited end of the coaxial cable extension should somehow be avoided without letting the wave get out of the cable to cause unwanted radiation.

9 Conclusions

This work was centered around the programming work to implement a MoM solver for the electromagnetic surface integral equations with EFIE-PMCHWT formulation. As is seen in Chapter 8, the work resulted as a very accurate numerical solver that can be used for complex electromagnetic problems with composite metal-dielectric structures. The computation of antenna parameters with the solver was also a success. As such, the solver can well be used to find the most important antenna parameters with the methods described in this work.

This work also included a lot of error prone hand made optimization of the triangular meshes needed for the simulations. The traingular mesh of the patch antenna needed a lot of optimization to get the accuracy seen in the results. The amount of work needed for this is so large that a lot of workload would be saved by using commercial programs for the mesh generation.

Two important discoveries were made in this thesis. First was about the short circuited coaxial cable extension, that was used to feed the patch antenna. As is clearly seen from the antenna impedance results, a cable extension length l_c, which gives infinite impedance at the coaxial aperture seen into the cable, i.e. which is related to the wavelength λ by $l_c = (0.25 + n \cdot 0.5)\,\lambda$, gives false results and needs to be avoided. However, a cable extension length l_c, which gives zero impedance at the coaxial aperture seen into the cable, i.e. which is related to the wavelength λ by $l_c = n \cdot 0.5\lambda$, gives no problems, and can be used to model coaxial feed. Anything in between also seems to work quite good. However, the reflection always causes problems, if the frequency range of the simulation is large. In order to get a coaxial feed model that had none of these problems, the reflection given by the short circuiting of the cable extension should be avoided by somehow implementing a reflection free TEM boundary condition for the surface integral equation method.

Second discovery (of an old fact) was about the thin sheet approximation. As is clearly seen from the input impedance results of the patch antenna, the thin sheet approximation of metallic sheets of small thickness gives false effective size for the sheet. This is a fact that is very well known by most of the RF and microwave engineers, but can very often be ignored in numerics. As is well seen by the results, the numerical results of the input impedance of the patch antenna match very well into the measured values, when the thickness is also modeled. As there are well known approximative formulas for the effective size of metallic sheets of microstrip structures, it would be interesting to use these formulas to change the size of the patch antenna element and use thin sheet approximation with the effective size of the patch to calculate the antenna impedance. The results should most probably be very accurate. However, this kind of a compensating for the effective size cannot be used for microstrip antennas of arbitrary shape, so the thickness should always be included in the model and thin sheet approximation should be avoided, if the most accurate results are desired.

References

[1] Jackson, J. D. "Classical electrodynamics", pp. 2–25, 209–226, 284–312, 335–339, John Wiley & Sons, New York, 1975

[2] Stratton, J. A. and Chu, L. K. "Diffraction theory of electromagnetic waves", *Physical Review*, vol. 56, pp. 99–107, July 1939

[3] Stratton, J. A. "Electromagnetic theory", pp. 563–573, McGraw-Hill, New York, 1941

[4] Peterson, A. F., Ray, S. L. and Mittra, R. "Computational methods for electromagnetics", pp. 1–16, Oxford University Press, Oxford, 1998

[5] J.-S. Zhao and W. C. Chew: Integral equation solution of Maxwell's equations from zero frequency to microwave frequencies, *IEEE Trans. Antennas and Propagation*, vol. 48, no. 10, pp. 1635-1645, Oct. 2000.

[6] M. Taskinen and P. Ylä-Oijala, Current and charge integral equation formulation, *IEEE Trans. Antennas Propag.*, vol. 54, no. 1, pp. 58-67, Jan. 2006.

[7] Taskinen, M. Vänskä, S. "Current and charge integral equation formulations and Picard's extended Maxwell system", *IEEE Transactions on Antennas and Propagation*, vol. 55, no. 12, pp. 3495–3503, Dec. 2007

[8] Chew, W. C. "Waves and fields in inhomogheneous media", pp. 410–421, Van Nostrand, New York, 1990

[9] Deeley, E. M. "Surface impedance near edges and corners in three-dimensional media", *IEEE Transactions on Magnetics,* vol. 26, no. 2, pp. 712–714, March 1990

[10] Jingguo, W. and Lavers, J. D. "Modified surface impedance boundary conditions for 3D eddy current problems", *IEEE Transactions on Magnetics,* vol. 29, no. 2, pp. 1826–1829, March 1993

[11] Harrington, R. F. "Field computation by moment methods", Macmillan, New York, 1968

[12] Rao, S., Wilton, D. and Glisson, A. "Electromagnetic scattering by surfaces of arbitrary shape", *IEEE Transactions on Antennas and Propagation,* vol. 30, no. 3, pp. 409–418, May 1982

[13] Kolundzija, B. M. and Djordjevic, A. R. "Electromagnetic modeling of composite metallic and dielectric structures", Artech House, Norwood, 2002

[14] P. Ylä-Oijala, M. Taskinen and S. Järvenpää, Surface integral equation formulations for solving electromagnetic scattering problems with iterative methods, *Radio Science*, vol. 40 no. 6, RS6002, Nov. 2005.

[15] Mautz J. R. and R. F. Harrington, H-field, E-field and combined-field solutions for conducting bodies of revolution, *Arch. Elektr. Übertragung.*, Vol. 32, pp. 157-164, 1978.

[16] Harrington R. F., Boundary integral formulations for homogeneous material bodies, *Journal of Electromagnetic Waves and Applications*, 3, 1-15, 1989.

[17] A. J. Poggio and E. K. Miller: Integral equation solutions of three-dimensional scattering problems, in *Computer Techniques for Electromagnetics*, R. Mittra (ed.), Oxford U.K. Pergamon Press, 1973.

[18] Chang, Y. and Harrington, R. F. , "A surface formulation for characteristic modes of material bodies", *IEEE Transactions on Antennas and Propagation*, Vol. 25, No. 6, pp. 789-795, Nov. 1977.

[19] Wu, T. K. and Tsai, L. L. "Scattering from arbitrarily-shaped lossy dielectric bodies of revolution", *Radio Science*, Vol. 12, No. 5, Sept.Oct. 1977, pp. 709–718.

[20] Ylä-Oijala, P., Taskinen, M. and Sarvas, J. "Surface integral equation method for general composite metallic and dielectric structures with junctions", *PIER 52,* pp. 81–108, 2005

[21] Putnam, J. M., Medgyesi-Mitschang, L. N. "Combined field integral equation formulation for inhomogeneous two and three-dimensional bodies: The junction problem", *IEEE Transactions on Antennas and Propagation,* vol. 39, no. 5, pp. 667–672, May 1991

[22] P. Ylä-Oijala and M. Taskinen: Calculation of CFIE impedance matrix elements with RWG and $\hat{\boldsymbol{n}}\times$RWG functions, *IEEE Trans. Antennas and Propagation*, vol. 51, no. 8, pp. 1837-1846, Aug. 2003.

[23] R. D. Graglia, D. R. Wilton and A. F. Peterson: Higher order interpolatory vector bases for computational electromagnetics, *IEEE Transactions on Antennas and Propagation*, Vol. 45, No. 3, pp. 329-342, 1997.

[24] B. M. Kolundzija and B. D. Popovic, Entire domain Galerkin method for analysis of metallic antennas and scatterers, *IEE Proceedings-H*, vol. 140, no. 1, pp. 1-10, Feb., 1993.

[25] Stroer J. and Bulirsch R.: Introduction to Numerical Analysis, Springer-Verlag, New York, 1993 (Second ed.).

[26] Dunavant, D. A. , High degree efficient symmetrical Gaussian quadrature rules for the triangle, *International Journal for Numerical Methods in Engineering*, vol. 21, no. 6, pp. 1129–1148, 1985.

[27] S. Caorsi, D. Moreno and F. Sidoti: Theoretical and numerical treatment of surface integrals involving the free-space Green's function, *IEEE Transactions on Antennas and Propagation*, Vol. 41, No. 9, pp. 1296-1301, 1993.

[28] D. R. Wilton, S. M. Rao, A. W. Glisson, D. H. Schaubert, O. M. Al-Bundak and C. M. Butler, Potential integrals for uniform and linear source distributions on polygonal and polyhedral domains, *IEEE Transactions on Antennas and Propagation*, vol. AP-32, no. 3, pp. 276-281, 1984.

[29] R. D. Graglia, On the numerical integration of the linear shape functions times the 3-D Green's function or its gradient on a plane triangle, *IEEE Transactions on Antennas and Propagation*, vol. 41, no. 10, pp. 1448-1455, 1993.

[30] R. E. Hodges and Y. Rahmat-Samii: The evaluation of MFIE integrals with the use of vector triangle basis functions, *Microwave and Optical Technology Letters*, Vol. 14, pp. 9-14, 1997.

[31] Hänninen, I., Taskinen, M. and Sarvas, J. "Singularity subtraction integral formulae for surface integral equations with RWG, rooftop and hybrid basis functions", *PIER 63,* pp. 243–278, 2006

[32] Collin, R. E., "Antennas and radiowave propagation", pp. 13–46, 293–303, McGraw-Hill, United States, 1985

[33] Collin, R. E. and Zucker, F. J. "Antenna theory part 1", pp. 1–28, McGraw-Hill, United States, 1969

[34] Sarkar, T.K. and Pereira, O. " Using the matrix pencil method to estimate the parameters of a sum of complex exponentials", *IEEE Antennas and Propagation Magazine* vol. 37, no. 1, pp. 48–55, February 1995

[35] Pozar, D. M. , Input impedance and mutual coupling of rectangular microstrip antennas, *IEEE Transactions on Antennas and Propagation*, Vol. 30, No. 6, Nov. 1982.

[36] Mosig, J.R. Gardiol, F. E. , General integral equation formulation for microstrip antennas and scatterers, *IEE Proceedings-H* Vol. 132, No. 7, Dec. 1985.

[37] Mie, G. "Beiträge zur optik trüber medien, speziell kolloidaler metallösungen", *Ann. der Phys.* , vol. 25, pp. 377-445, 1908.

[38] A. Van de Capelle, C. Cao, F. Demuynck, B. Nauwelaers, G. Vandenbosch, C. Van Himbeeck, E. Van Lil, Current antenna research at K. U. Leuven *IEEE Antennas and Propagation Magazine*, Vol. 33, No. 5, pp. 30-42, Oct. 1991.

[39] G. A. F. Vandenbosch and A. R. Van de Capelle, Mixed-potential integral expression formulation of the electric field in a stratified dielectric medium – Application to the case of a probe current source, *IEEE Transactions on Antennas and Propagation*, Vol. 40, No. 7, pp. 806-817, July, 1992.

[40] Van Bladel J.: *Singular Electromagnetic Fields and Sources*, Clarendon Press, Oxford, 1991.

[41] B. Kolundzija, Precise modeling of microstrip patch antennas (finite metallization, substrate and ground), *IEEE APS Symposium*, San Antonio, USA, vol. 3, pp. 434-437, 2002.

[42] Bahl, I. J. and Garg, R. "Simple and accurate formulas for a microstrip with finite strip thickness", vol. 65, no. 11, pp. 1611-1612, Nov. 1977

[43] Andriulli, F. P. Cools, K. Bagci, H. Olyslager, F. Buffa, A. Christiansen, S. and Michielssen, E. "A Multiplicative Calderon Preconditioner for the Electric Field Integral Equation", *IEEE Transacyions on Antennas and Propagation*, Vol. 56, No. 8, pp. 2398–2412, Aug. 2008